Microwave cavity searches for dark-matter axions

Richard Bradley
National Radio Astronomical Observatory, Charlottesville, Virginia 22903

John Clarke
University of California, Berkeley, California 94720

Darin Kinion, Leslie J Rosenberg, and Karl van Bibber
Lawrence Livermore National Laboratory, Livermore, California 94551

Seishi Matsuki
Kyoto University, Kyoto 611-0011, Japan

Michael Mück
Justus Liebig University, D-35392 Giessen, Germany

Pierre Sikivie
University of Florida, Gainesville, Florida 32611

(Published 12 June 2003)

Recent determinations of cosmological parameters point to a flat Universe, whose total energy density is composed of about two-thirds vacuum energy and one-third matter. Ordinary baryonic matter is relegated to a small fraction of the latter, within which the luminous part is an order of magnitude smaller yet. Particle dark matter, i.e., one or more relic particle species from the big bang, is thus strongly suggested as the dominant component of matter in the Universe. The axion, a hypothetical elementary pseudoscalar arising from the Peccei-Quinn solution to the strong-CP problem, is a well-motivated candidate. If the axion exists, it must be extremely light, in the mass range of 10^{-6}–10^{-3} eV, and possess extraordinarily feeble couplings to matter and radiation. Nevertheless, as proposed by Sikivie in 1983, the axion's two-photon coupling lends itself to a feasible search strategy with currently available technology. In this scheme, axions resonantly convert to single microwave photons by a Primakoff interaction, in a tunable microwave cavity permeated by a strong magnetic field. Present experiments utilizing heterostructure transistor microwave amplifiers have achieved total system noise temperatures of $\sim$3 K and represent the world's quietest spectral radio receivers. Exclusion regions have already been published well into the band of realistic axion model couplings, within the lowest decade of mass range. Recent breakthroughs in the development of near-quantum-limited superconducting quantum interference device amplifiers should reduce the system noise temperature to $\sim$100 mK or less. Ongoing research into using Rydberg-atom single-quantum detectors as the detector in a microwave cavity experiment could further reduce the effective noise temperature. In parallel with improvements in amplifier technology, promising concepts for higher-frequency cavity resonators are being explored to open up the higher decades in mass range. Definitive experiments to find or exclude the axion may therefore be at hand in the next few years. As the microwave cavity technique measures the total energy of the axion, a positive discovery could well reveal fine structure of the signal due to flows of nonthermalized axions. Manifesting diurnal and sidereal modulation, such detailed features would contain a wealth of information about the history, structure, and dynamics of our Milky Way galaxy.

CONTENTS

I. OVERVIEW

The advent of precision cosmology has provided us with a clear picture of our Universe. To a high degree it is flat ($\Omega \sim 1$), presently composed of approximately one-third matter ($\Omega_m \sim 0.35$) and two-thirds vacuum energy ($\Omega_\Lambda \sim 0.65$), and seemingly doomed to a cold, dilute fate. Determination of these cosmological parameters rests primarily on recent cosmic microwave background radiation studies at subdegree angular scales (de Bernadis *et al.*, 2000; Hanany *et al.*, 2000) and measurements of the Hubble diagram at high redshift by Type-Ia supernova surveys (Reiss *et al.*, 1998; Perlmutter *et al.*, 1999).

Moreover, bounds from primordial nucleosynthesis now limit the density of ordinary baryons to one-seventh of all matter, $\Omega_b \sim 0.045$ (Schramm and Turner, 1998).

The aforementioned axion is one of the "usual suspects," having arisen from what is still the most attractive solution to the strong-CP problem. Since the original work of Peccei and Quinn (1977), it has been constrained to a three-decade mass range (10^{-6}–10^{-3} eV), where all its couplings, being proportional to its mass, would be extraordinarily feeble. Paradoxically, the cosmological energy density of axions increases as the mass of the axion decreases, reaching $\Omega_a \sim 1$ for masses within this range, depending on the scenario for axion production in the big bang. Thus a very light axion was seen to be a good cold-dark-matter candidate but impossible to detect, earning it the label "invisible axion." Nevertheless, an elegant technique for detecting axions constituting our galactic dark-matter halo was developed by Sikivie (1983a, 1985), by which axions resonantly convert to microwave photons in a tunable high-Q cavity permeated by a strong magnetic field. This proposal was well grounded in the technological state of the art, and several small experiments and research and development efforts ensued almost immediately.

This report is devoted entirely to microwave cavity searches for dark-matter axions. We believe this is a good time to review this subject, with third-generation experiments under development that should achieve the sensitivity required for the entire range of axion models. Indeed, this experiment has driven a research and development program on ultralow-temperature microwave detectors on three fronts of technology. Experiments published to date have used conventional amplifiers based on heterostructure field-effect transistors (HFET's), more commonly known by the trade name high-electron-mobility transistors (HEMT). The noise temperature of packaged HFET amplifiers in the gigahertz range has improved steadily over the years to ~ 1.5 K, and the microwave cavity experiment based on these devices already represents by far the quietest spectral receiver in the world in the gigahertz frequency range. The invention of high-gain gigahertz dc superconducting quantum interference device (SQUID) amplifiers was funded explicitly for the next-generation axion experiment. The noise temperature of one 600-MHz SQUID, for example, was measured to be ~ 50 mK, roughly twice the quantum limit. Finally, Rydberg-atom single-quantum detectors, also developed specifically for the axion search, have produced effective noise temperatures as low as ~ 12 mK, evading the standard quantum limit entirely, as a phaseless detector can.

Why search for the axion in dark matter? Such a search would seem to require two independent assumptions, namely, (1) that the axion exists, and (2) that it is the dominant component of our galactic halo. Would it not be more sensible to first determine whether the axion exists, in some purely laboratory experiment (ideally determining its mass as well), and then conduct a focused search for axions in the halo? The first, and weaker, answer is that the two assumptions are not entirely independent; a very light axion would almost necessarily be cosmologically significant. The second and real reason is that laboratory experiments lack sensitivity. The signal rate in production-detection (Hertzian) experiments goes as g^4, where g is the coupling, and their rate for plausible models is irrelevantly small. The rate in a Sikivie-type experiment, however, goes as g^2, relying as it does on preexisting axions. Even with their prodigious local density, e.g., 10^{14} cm^{-3} for a 10-μeV axion, the expected conversion power is extremely weak, $\sim 10^{-23}$ W, and is feasible only in a high-Q experiment that trades off bandwidth for sensitivity. Theoretical reviews of the axion and its astrophysical implications include those of Kim (1987), Turner (1990), and Raffelt (1990).

II. REVIEW OF AXION THEORY

A. Particle physics and the axion

The axion was postulated more than two decades ago (Peccei and Quinn, 1977; Weinberg, 1978; Wilczek, 1978) to explain why the strong interactions conserve P and CP in spite of the fact that strongly coupled objects (instantons, pseudoparticles) violate those symmetries. For reviews see Kim (1987); Cheng (1988); Peccei (1989); Raffelt (1990); and Turner (1990).

Consider the Lagrangian of QCD:

$$\mathcal{L}_{QCD} = -\frac{1}{4} G^a_{\mu\nu} G^{a\mu\nu} + \sum_{j=1}^{n} [\bar{q}_j \gamma^\mu i D_\mu q_j - (m_j q^\dagger_{Lj} q_{Rj} + \text{H.c.})] + \frac{\theta g^2}{32\pi^2} G^a_{\mu\nu} \tilde{G}^{a\mu\nu}. \quad (1)$$

The last term is a four-divergence and hence does not perturbatively contribute to the equations of motion. That term does, however, contribute through nonperturbative effects (Callan *et al.*, 1976; Jackiw and Rebbi, 1976; 't Hooft, 1976a, 1976b) associated with QCD instantons (Belavin *et al.*, 1975). Hence the quantitative predictions of QCD generally depend on the value of θ. From the Adler-Bell-Jackiw anomaly (Adler, 1969; Bell and Jackiw, 1969), one can show that θ dependence must be present provided none of the current quark masses vanishes. Without θ dependence, QCD would have a $U_A(1)$ symmetry and would predict the mass of the η' pseudoscalar meson to be less than $\sqrt{3} m_\pi \approx 240$ MeV (Weinberg, 1975), contrary to observation. Using the anomaly, one can further show that QCD depends on θ only through the combination of parameters:

$$\bar{\theta} = \theta - \arg\det(m_1, m_2, \ldots, m_n), \quad (2)$$

where $\arg\det(m_1, m_2, \ldots, m_n)$ is the phase of the quark mass matrix. If $\bar{\theta} \neq 0$, QCD violates P and CP. The observed absence of P and CP violations in the strong interactions therefore places an upper limit upon $|\bar{\theta}|$. The most stringent constraint comes from the experimental bound (Harris *et al.*, 1999) on the neutron electric dipole moment, which yields $|\bar{\theta}| < 10^{-9}$.

The question then is: why is $\bar{\theta}$ so small? In the standard model of particle interactions, the quark masses originate in the electroweak sector, which we know violates P and CP. There is no reason why the overall phase of the quark mass matrix should exactly match the value of θ from the QCD sector to yield $|\bar{\theta}| < 10^{-9}$. In particular, if CP violation is introduced in the manner of Kobayashi and Maskawa (1973), the Yukawa couplings that give masses to the quarks are arbitrary complex numbers and hence $\arg\det m_q$ and $\bar{\theta}$ are expected to be of order 1.

The mystery as to why $|\bar{\theta}| < 10^{-9}$ is usually referred to as the "strong-CP problem." The existence of the axion solves this problem in a simple manner rich in implications for experiment, astrophysics, and cosmology. There are two alternative solutions, however. The first is to set at least one quark mass to zero. This removes the θ dependence of QCD, which is then CP conserving. However, the well-known calculation of the pseudoscalar meson masses in lowest order of chiral perturbation theory yields $m_u \simeq 4$ MeV and is not compatible with $m_u = 0$. This calculation also predicts the successful Gell-Mann–Okubo relation among the pseudoscalar masses squared. It is possible to have $m_u = 0$ by invoking second-order effects (Georgi and McArthur, 1981; Kaplan and Manohar, 1986; Choi, 1992). This is a reasonable proposition because m_s happens to be of order the QCD scale. However, when second-order effects are included (Gasser and Leutwyler, 1985), the Gell-Mann–Okubo relation is in general violated. Thus the price for having $m_u = 0$ through higher-order effects is that the Gell-Mann–Okubo relation becomes an accident. The second alternative solution to the strong-CP problem is to assume that CP and/or P is spontaneously broken but is otherwise a good symmetry. In this case, $\bar{\theta}$ is calculable and may be arranged to be small.[1]

Finally, it is worth emphasizing that the strong-CP problem need not be solved in the low-energy theory. Indeed, as Ellis and Gaillard (1979) pointed out, if in the Standard Model $\bar{\theta} = 0$ near the Planck scale, then $\bar{\theta} \ll 10^{-9}$ at the QCD scale.

Peccei and Quinn (1977) proposed to solve the strong-CP problem by postulating the existence of a global $U_{PQ}(1)$ quasisymmetry. $U_{PQ}(1)$ must be a symmetry of the theory at the classical (i.e., Lagrangian) level, it must be broken explicitly by those nonperturbative effects that make the physics of QCD depend upon θ, and it must be spontaneously broken. The axion (Weinberg, 1978; Wilczek, 1978) is the quasi-Nambu-Goldstone boson associated with the spontaneous breakdown of $U_{PQ}(1)$. One can show that, if a $U_{PQ}(1)$ quasisymmetry is present, then

$$\bar{\theta} = \theta - \arg\det(m_1, m_2, \ldots, m_n) - \frac{a(x)}{f_a}, \quad (3)$$

where $a(x)$ is the axion field, $f_a = v_a / N$ is called the axion decay constant, v_a is the vacuum expectation value, which spontaneously breaks $U_{PQ}(1)$, and N is an integer that expresses the color anomaly of $U_{PQ}(1)$ symmetry. Axion models have N degenerate vacua (Sikivie, 1982). The nonperturbative effects that make QCD depend upon $\bar{\theta}$ produce an effective potential $V(\bar{\theta})$ whose minimum is at $\bar{\theta} = 0$ (Vafa and Witten, 1984). Thus, by postulating an axion, $\bar{\theta}$ is allowed to relax to zero dynamically and the strong-CP problem is solved.

The properties of the axion can be derived using the methods of current algebra (Bardeen and Tye, 1978;

[1]This approach was taken by Beg and Tsao, 1978; Georgi, 1978; Mohapatra and Senjanovic, 1978; Barr, 1984; Nelson, 1984; Babu and Mohapatra, 1990; Barr *et al.*, 1991; Frampton and Kephart, 1991; Frampton and Ng, 1991; Kuchimanchi, 1996; Mohapatra and Rasin, 1996.

Donnelly *et al.*, 1978; Weinberg, 1978; Ellis and Gaillard, 1979; Kaplan, 1985; Srednicki, 1985; Sikivie, 1987). The axion mass is given in terms of f_a by

$$m_a \simeq 0.6 \text{ eV} \frac{10^7 \text{ GeV}}{f_a}. \quad (4)$$

All the axion couplings are inversely proportional to f_a. Of particular interest here is the axion coupling to two photons:

$$\mathcal{L}_{a\gamma\gamma} = -\left(\frac{\alpha}{\pi}\frac{g_\gamma}{f_a}\right) a\vec{E}\cdot\vec{B} = -g_{a\gamma\gamma} a\vec{E}\cdot\vec{B}, \quad (5)$$

where $\vec{E}$ and $\vec{B}$ are the usual electric and magnetic fields, α is the fine-structure constant, and g_γ is a model-dependent coefficient of order 1. The strength of the interaction depends on the assignment of $U_{\mathrm{PQ}}(1)$ charges to (perhaps new) quarks and leptons. $g_\gamma = 0.36$ in the Dine-Fischler-Srednicki-Zhitnitskii (DFSZ) model (Zhitnitskii, 1980; Dine *et al.*, 1981), whereas $g_\gamma = -0.97$ in the Kim-Shifman-Vainshtein-Zakharov (KSVZ) model (Kim, 1979; Shifman *et al.*, 1980). Experimental results are often given in terms of $g_{a\gamma\gamma}$, the effective two-photon coupling constant. The coupling of the axion to a spin-1/2 fermion f has the form

$$\mathcal{L}_{a\bar{f}f} = i g_f \frac{m_f}{v_a} a\bar{f}\gamma_5 f, \quad (6)$$

where g_f is a model-dependent coefficient of order one. In the KSVZ model, the coupling to electrons is zero at tree level. Models with this property are called "hadronic."

B. Constraints from laboratory searches and astrophysics

A priori, the value of v_a, and hence that of m_a, is arbitrary. When the axion was first proposed, it was thought that v_a is of order the electroweak scale, 250 GeV, in which case the axion mass is of order 100 keV. However, searches for the axion in high-energy and nuclear physics experiments combined with astrophysical constraints soon ruled out an electroweak scale axion. At present, the combined limits rule out axions heavier than about 3×10^{-3} eV.

The relevant high-energy and nuclear physics experiments were reviewed by Kim (1987) and by Peccei (1989). A complete list can be found in the *Review of Particle Physics* (Particle Data Group, 1998). Here we give only a very brief summary. If the axion is heavier than 1 MeV and decays quickly into e^+e^- (lifetime of order 10^{-11} sec or less), then it is ruled out by negative searches for rare particle decays such as $\pi^+ \to a(e^+e^-)e^+\nu_e$ (Eichler *et al.*, 1986). The rate of this particular reaction follows simply from the mixing of a and π^0 and the known decay $\pi^+ \to \pi^0 e^+ \nu_e$, hence it is almost completely model independent (Suzuki, 1986). Alternatively, long-lived axions (10^{-11} sec or more) are severely constrained by negative searches in beam dumps. In a beam dump, axions are produced by many different processes involving independent couplings, such as $a-\pi^0$, $a-\eta$, and $a-\eta'$ mixing, the axion couplings to two photons and to two gluons, and the couplings to quarks and gluons. It is difficult to calculate these processes with precision at all energies. However, the many processes add up incoherently and they cannot all vanish. Thus one can give a reliable estimate for the total production ($p+N\to a+X$, or $e+N\to a+X$) and interaction ($a+N\to X$) cross sections. Many such searches (Particle Data Group, 1998) have been carried out. They rule out long-lived axions with mass larger than about 50 keV. When the limits from laboratory searches are combined with the astrophysical constraints, the whole axion mass range down to approximately 3×10^{-3} eV is ruled out, as described briefly below.

The astrophysical constraints on the axion have been reviewed by Turner (1990) and Raffelt (1990). Axions could be emitted by stars in a variety of processes such as Compton-like scattering ($\gamma+e\to a+e$), axion bremsstrahlung ($e+N\to N+e+a$), and the Primakoff process ($\gamma+N\to N+a$). The rate at which a star burns its nuclear fuel is limited by the rate at which it can lose energy. Emission of weakly coupled light bosons, such as axions, allows a star to lose energy efficiently because such particles can escape the star without rescattering, whereas photons are scattered numerous times before leaving the star. Thus the existence of the axion would accelerate stellar evolution and is therefore constrained by observation. The abundance of stars along red giant branches rules out the mass range $200 \text{ keV} \gtrsim m_a \gtrsim 0.5$ eV (Dicus *et al.*, 1978, 1980; Raffelt and Dearborn, 1987) for hadronic axions. Above 200 keV the axion is too heavy to be copiously emitted in the thermal processes taking place in red giants, whereas below 0.5 eV it is too weakly coupled. For axions with a large coupling to electrons [$g_e = \mathcal{O}(1)$ in Eq. (6)] the excluded range can be extended to $200 \text{ keV} \gtrsim m_a \gtrsim 10^{-2}$ eV, since the cooling of the helium core of red giants by axion emission would prevent the onset of helium burning (Dearborn *et al.*, 1986).

Finally, the range $2 \text{ eV} \gtrsim m_a \gtrsim 3\times10^{-3}$ eV is ruled out by the terrestrial neutrino signal from Supernova 1987a (Ellis and Olive, 1987; Raffelt and Seckel, 1988; Turner, 1988; Janka *et al.*, 1996; Keil *et al.*, 1997). This constraint follows from the observation that the duration of the associated neutrino events in the large underground proton decay detectors (Alexeyev *et al.*, 1987; Bratton *et al.*, 1988; Hirata *et al.*, 1988) is consistent with theoretical expectations based on the premise that the collapsed supernova core cools solely by emission of neutrinos. If the axion mass is in the above-mentioned range, the core also cools by axion emission, and the neutrino burst is excessively foreshortened. The supernova constraint is relatively axion model independent because the axions are emitted by axion bremsstrahlung in nucleon-nucleon scattering ($N+N\to N+N+a$) and the relevant couplings follow simply from the mixing of the axion with π^0, which is a generic feature of axion models.

C. Axions and cosmology

The implications of the axion for the history of the early universe may be briefly described as follows. At a temperature of order f_a, a phase transition occurs in which the Peccei and Quinn $U_{\rm PQ}(1)$ symmetry becomes spontaneously broken. This is called the PQ phase transition. At these temperatures, the nonperturbative QCD effects that produce the effective potential $V(\overline{\theta})$ are suppressed (Gross *et al.*, 1981), the axion is massless, and all values of $\langle a(x)\rangle$ are equally likely. In this phase transition, axion strings appear as topological defects. One must distinguish two cases: (1) inflation occurs with reheat temperature less than the PQ transition temperature or (2) inflation occurs with reheat temperature higher than the PQ transition temperature (equivalently, for our purposes, inflation does not occur at all). In case (1) the axion field gets homogenized by inflation and the axion strings are diluted away, whereas in case (2) axion strings are present from the PQ transition to the QCD epoch.

When the temperature approaches the QCD scale, the potential $V(\overline{\theta})$ turns on and the axion acquires mass. There is a critical time, defined by $m_a(t_1)t_1=1$, at which the axion field starts to oscillate in response to the axion mass turn-on (Abbott and Sikivie, 1983; Dine and Fischler, 1983; Preskill *et al.*, 1983). The corresponding temperature $T_1\simeq 1$ GeV. In case (1), in which the axion field has been homogenized by inflation, the initial amplitude of this oscillation depends on how far from zero the axion field is at t_1. The axion field oscillations do not dissipate into other forms of energy and hence contribute to the cosmological energy density today (Abbott and Sikivie, 1983; Dine and Fischler, 1983; Preskill *et al.*, 1983). This contribution is called *vacuum realignment*. It is the only contribution in case (1). In terms of the critical density $\rho_c=3H_0^2/8\pi G$, it is

$$\Omega_a=\frac{\rho_a(t_0)}{\rho_c}\simeq\frac{1}{6}\alpha^2(t_1)\left(\frac{f_a}{10^{12}\ \mathrm{GeV}}\right)^{7/6}\left(\frac{0.7}{h}\right)^2\ \ [\text{case (1)}],$$

where h parametrizes the present Hubble rate $H_0=h\times 100$ km/sec Mpc and $\alpha(t_1)=a(t_1)/f_a$ is the initial misalignment angle. Note that Ω_a may be accidentally suppressed in case (1) if the homogenized axion field happens to lie close to zero.

In case (2) the axion strings radiate axions (Davis, 1985a, 1985b; Harari and Sikivie, 1987) from the time of the PQ transition until t_1. At t_1 each string becomes the boundary of N domain walls. If $N=1$, the network of walls bounded by strings is unstable (Vilenkin and Everett, 1982; Sikivie, 1983b) and decays away. If $N>1$ there is a "domain wall problem" (Sikivie, 1982) because axion domain walls end up dominating the energy density, resulting in a universe very different from the one observed today. Henceforth, we assume $N=1$. There are three contributions to the axion cosmological energy density in case (2). One contribution[2] is from axions that were radiated by axion strings before t_1. A second contribution[3] is from axions that were produced in the decay of walls bounded by strings after t_1. A third contribution is from vacuum realignment (Abbott and Sikivie, 1983; Dine and Fischler, 1983; Preskill *et al.*, 1983). The vacuum realignment contribution is in case (2)

$$\Omega_a^{\rm vac}\simeq\frac{1}{3}\left(\frac{f_a}{10^{12}\ \mathrm{GeV}}\right)^{7/6}\left(\frac{0.7}{h}\right)^2. \tag{7}$$

In case (2), the vacuum realignment contribution cannot be accidentally suppressed because it is an average over many horizon volumes at QCD time, each with a causally independent value of the initial misalignment angle $\alpha(t_1)$. Note also that the vacuum realignment contribution is larger, by approximately a factor of 2, in case (2) than it is in case (1), with $\alpha(t_1)\simeq 1$. This is because only the "zero-momentum mode" contributes in case (1), whereas in case (2) there are contributions from the zero-momentum mode and from higher modes (Chang *et al.*, 1999). The contribution from wall decay is (Chang *et al.*, 1999)

$$\Omega_a^{\rm d.w.}\simeq\frac{2}{\gamma}\left(\frac{f_a}{10^{12}\ \mathrm{GeV}}\right)^{7/6}\left(\frac{0.7}{h}\right)^2, \tag{8}$$

where $\gamma\equiv\langle\omega_a\rangle/m_a$ is the average Lorentz factor of the axions produced in the decay of walls bounded by strings. In simulations, Chang *et al.* (1999) found that $\gamma\sim 7$ for $\ln(v_a/m_a)\simeq 6$, and that γ increases approximately linearly with $\ln(v_a/m_a)$. Extrapolation of this behavior to the parameter range of interest, $\ln(v_a/m_a)\simeq 60$, yields $\gamma\sim 60$, suggesting that the wall decay contribution is subdominant compared to the vacuum realignment contribution.

The string decay contribution has been the most controversial. There are three estimates in the literature. The result of Battye and Shellard (1994a, 1994b, 1996) is

$$\Omega_a^{\rm str,BS}\simeq 10.7\left(\frac{\xi}{13}\right)\left[\left(1+\frac{\alpha}{\kappa}\right)^{3/2}-1\right]\frac{1}{h^2}\left(\frac{f_a}{10^{12}\ \mathrm{GeV}}\right)^{7/6}, \tag{9}$$

where we have put in the dependence on ξ explicitly. ξ parametrizes the average distance between axion strings at time t as ξt. The ratio of parameters α/κ is expected to be in the range $0.1<\alpha/\kappa<1.0$ (Battye and Shellard, 1994a, 1994b, 1996). Battye and Shellard obtain the estimate $\xi\simeq 13$ from their simulations of local string networks in an expanding universe. However, axion strings are *global strings*. Global strings have most of their energy in the Nambu-Goldstone field surrounding the string core, whereas local strings have most of their energy inside the string core. At any rate, for the expected range of α/κ,

[2]See, for example, Davis, 1985, 1986; Harari and Sikivie, 1987; Hagmann and Sikivie, 1991; Battye and Shellard, 1994a, 1994b, 1996; Yamaguchi *et al.*, 1999; Hagmann *et al.*, 2001.

[3]See, for example, Hagmann and Sikivie, 1991; Lyth, 1992a; Nagasawa and Kawasaki, 1994; Chang *et al.*, 1999.

$$\Omega_a^{\mathrm{str,BS}} = (3.4-40)\left(\frac{\xi}{13}\right)\left(\frac{f_a}{10^{12}\ \mathrm{GeV}}\right)^{7/6}\left(\frac{0.7}{h}\right)^2. \quad (10)$$

Yamaguchi *et al.* (1999) carry out simulations of global string networks in an expanding universe and find $\xi = 1.00 \pm 0.08$. Their result for the string decay contribution to the cosmological axion energy density is

$$\Omega_a^{\mathrm{str,YKY}} = (1.4 \pm 0.94)\left(\frac{f_a}{10^{12}\ \mathrm{GeV}}\right)^{7/6}\left(\frac{0.7}{h}\right)^2. \quad (11)$$

Hagmann and Sikivie (1991) and Hagmann (2001) carried out simulations of the motion and decay of single string loops and of oscillating bent strings, focusing their effort on obtaining the correct spectrum of the axions radiated by strings. They used $\xi \simeq 1$. Their result is

$$\Omega_a^{\mathrm{str,HCS}} \simeq \left(\frac{1}{3}\right) 2^{\pm 1}\left(\frac{f_a}{10^{12}\ \mathrm{GeV}}\right)^{7/6}\left(\frac{0.7}{h}\right)^2. \quad (12)$$

The last two results are consistent with one another. The result of Battye and Shellard is compatible with the other two if one sets $\xi \simeq 1$ instead of $\xi \simeq 13$. Since axion strings are global rather than local, the global string network simulations of Yamaguchi *et al.* may be considered more reliable in determining ξ. If we use $\xi = 1$, all estimates are consistent and suggest

$$\Omega_a = \Omega^{\mathrm{vac}} + \Omega^{\mathrm{d.w.}} + \Omega^{\mathrm{str}} = (0.5\text{–}3.0)\left(\frac{f_a}{10^{12}\ \mathrm{GeV}}\right)^{7/6}\left(\frac{0.7}{h}\right)^2 \quad [\text{case (2)}].$$

Equation (4), case (1), and case (2) suggest that the interesting mass range for dark-matter axions is 1–100 μeV.

It should be emphasized that there are many sources of uncertainty in the cosmological axion energy density aside from the uncertainty about the contribution from string decay. The axion energy density may be diluted by the entropy release from heavy particles that decouple before the QCD epoch but decay afterward (Steinhardt and Turner, 1983; Lazarides *et al.*, 1990), or by the entropy release associated with a first-order QCD phase transition. However, in the unlikely case when the QCD phase transition is first order (Turner, 1985; Unruh and Wald, 1985; deGrand *et al.*, 1986; Hindmarsh, 1992), an abrupt change of the axion mass at the transition might increase Ω_a. As was already mentioned, if inflation occurs with reheat temperature less than T_{PQ}, there may be an accidental suppression of Ω_a because the homogenized axion field happens to lie close to a CP-conserving minimum. Because the vacuum misalignment angle $\alpha(t_1) = a(t_1)(N/v_a)$, whose square appears on the right-hand side of case (1), is randomly chosen between $-\pi$ and $+\pi$, the probability that Ω_a is suppressed by a factor x is of order $\sqrt{x}$. This cannot be extended to arbitrarily small x, however, because quantum-mechanical fluctuations in the axion field during the epoch of inflation do not allow the suppression to be perfect.[4]

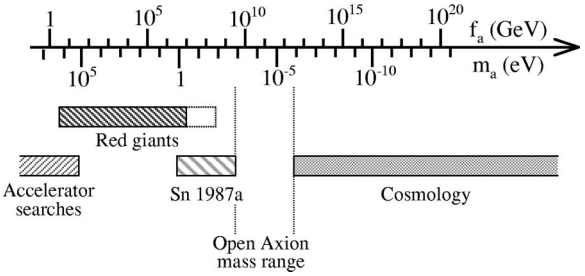

FIG. 1. Ranges of axion mass m_a (or axion decay constant f_a) that have been ruled out by accelerator searches, the evolution of red giants, the supernova SN1987a, and the axion cosmological energy density.

The axions produced when the axion mass turns on at the QCD phase transition, whether from string decay, vacuum realignment, or wall decay, have momenta $p_a \sim 1/t_1 \sim 10^{-8}$ eV/c when the surrounding plasma has temperature $T_1 \simeq 1$ GeV. They are nonrelativistic from the moment of their first appearance, do not thermalize, and are therefore a form of *cold dark matter* (CDM; Ipser and Sikivie, 1983). Studies of large-scale structure formation support the view that the dominant fraction of dark matter is CDM. Moreover, any form of CDM necessarily contributes to galactic halos by falling into the gravitational wells of galaxies. Hence there is a special opportunity to search for axions by direct detection on Earth.

Finally, we mention that there could be a particular kind of clumpiness (Hogan and Rees, 1988; Kolb and Tkachev, 1993, 1994, 1996; Chang *et al.*, 1999), which would affect axion dark matter if there were no inflation after the Peccei-Quinn phase transition. This clumpiness occurs because the dark-matter axions are inhomogeneous with $\delta\rho/\rho \sim 1$ over the horizon scale at temperature $T_1 \simeq 1$ GeV, when they are produced at the start of the QCD phase transition, combined with the fact that their velocities are so small that they would not erase these inhomogeneities by free streaming before the time t_{eq} of equality between the matter and radiation energy densities when matter perturbations can start to grow. These particular inhomogeneities in axion dark matter would occur immediately in the nonlinear regime after time t_{eq} and thus form clumps, called "axion miniclusters" (Hogan and Rees, 1988; Kolb and Tkachev, 1993, 1994, 1996). These could have mass $M_{mc} \simeq 10^{-13} M_\odot$ and size $l_{mc} \simeq 10^{13}$ cm.

The various constraints on the axion, from accelerator searches, astrophysics, and cosmology, are summarized in Fig. 1.

[4]See, for example, Linde, 1984, 1985; Seckel and Turner, 1985; Linde and Lyth, 1990; Lyth 1990; Linde, 1991; Turner and Wilczek, 1991; Lyth, 1992b; Lyth and Stewart, 1992a, 1992b.

D. Phase-space structure of halo dark-matter axions

Based on all observables of our Milky Way galaxy (e.g., rotation curve, microlensing optical depth, projected areal density of the disk, etc.), a global fit can be performed for a generic multicomponent halo. The best maximum-likelihood estimate for the cold-dark-matter component alone is $\rho_{CDM}=0.45\ \mathrm{Gev/cm^3}$, albeit with large uncertainties (Gates, Gyuk, and Turner, 1995). While it is often assumed that the CDM is thermalized, there is little experimental knowledge of its phase-space distribution at present.

If a signal is found in the cavity detector of galactic halo axions, it will be possible to measure the energy spectrum of cold-dark-matter particles on Earth with great precision and resolution. As Sec. III explains, the spread in the axion signal is due to the kinetic energy of motion of the axions relative to the detector. Present detectors can resolve the axion energy spectrum (assumed to be ~ 500 Hz) in 10^5 or more independent frequency bins. The energy spectrum contains a detailed history of the formation of the Milky Way halo. There is strong motivation to try to predict what the spectrum is because such knowledge may help coax the axion signal out of the noise.

In many past discussions of dark-matter detection on Earth, it has been assumed that the dark-matter particles have an isothermal velocity distribution. Thermalization has been argued to be the result of a period of "violent relaxation" following the collapse of the protogalaxy (Lynden-Bell, 1967). However, there could be substantial deviations from an isothermal distribution (Ipser and Sikivie, 1992) because of late infall and long thermalization times. If the dark matter is collisionless, as are axions, our Galaxy must be surrounded by a sea of dark-matter particles. The particles fall into the gravitational well of the Galaxy, forming a continual "rain." The flows of late infalling dark matter do not thermalize, even on time scales of order the age of the Universe (Sikivie and Ipser, 1992). Hence there is a discrete set of dark-matter flows with well-defined velocity vectors at any location in the halo, in addition to a thermalized component. One flow is composed of particles falling onto the galaxy for the first time, a second flow of particles falling out of the galaxy for the first time, a third flow of particles falling into the galaxy for the second time, etc. Each of the flows typically contains a few percent of the local halo density (Sikivie *et al.*, 1995, 1997).

The fractional width of the peaks in the energy spectrum due to the most recent infall is estimated (Sikivie and Ipser, 1992) to be of order 10^{-17}, although each peak may be fragmented into subpeaks of that approximate width. Because of the Earth's rotation ($v_{\mathrm{rot}} \simeq 10^{-6}c$) and its revolution around the Sun ($v_{\mathrm{rev}} \simeq 10^{-4}c$), the peak frequencies ω_n are modulated by the relative amount

$$\frac{\delta\omega_n}{\omega_n}=\frac{\vec{v}_n\cdot(\vec{v}_{\mathrm{rot}}+\vec{v}_{\mathrm{rev}})}{c^2}+\mathcal{O}\left(\frac{v^2}{c^2}\right), \tag{13}$$

where $v_n \simeq 10^{-3}c$ is the velocity of the nth flow relative to the Sun. (This is in addition, of course, to the Sun's orbital motion in the Milky Way, $v_{sun}\sim 10^{-3}c$.) Observation of the diurnal and sidereal frequency modulation of a peak allows one to determine the corresponding velocity vector $\vec{v}_n$ completely. Sikivie (1999) lists the local velocities and densities of the flows predicted by an idealized caustic ring model of the galactic halo (Sikivie *et al.*, 1995, 1997; Sikivie, 1998). The gravitational focusing effect of the Sun on the flows has recently been discussed by Sikivie and Wick (2002).

III. THE SIKIVIE MICROWAVE CAVITY EXPERIMENT

A. Principles and techniques

Axions can be detected by stimulating their conversion to photons in a strong magnetic field (Sikivie 1983a, 1985). The relevant coupling is given in Eq. (5). In particular, an electromagnetic cavity permeated by a strong static magnetic field can detect galactic halo axions. These halo axions have velocities β of order 10^{-3}, and hence their energies $E_a=m_a+\frac{1}{2}m_a\beta^2$ have a spread of order 10^{-6} above the axion mass. When the frequency $\omega=2\pi f$ of a cavity mode equals m_a, galactic halo axions convert resonantly into quanta of excitation (photons) of that cavity mode ($m_a=4.14\ \mu\mathrm{eV}$ corresponds to $f=1$ GHz). The power from axion-to-photon conversion on resonance is found to be (Krauss *et al.* 1985; Sikivie 1985)

$$\begin{aligned}P_a&=\left(\frac{\alpha}{\pi}\frac{g_\gamma}{f_a}\right)^2 V B_0^2\rho_a C\frac{1}{m_a}\mathrm{Min}(Q_L,Q_a)\\&=0.5\times10^{-26}\ \mathrm{W}\left(\frac{V}{500\ \mathrm{liter}}\right)\left(\frac{B_0}{7\ \mathrm{T}}\right)^2 C\left(\frac{g_\gamma}{0.36}\right)^2\\&\quad\times\left(\frac{\rho_a}{\frac{1}{2}\times10^{-24}\ \mathrm{g/cm^3}}\right)\\&\quad\times\left(\frac{m_a}{2\pi\ (\mathrm{GHz})}\right)\mathrm{Min}(Q_L,Q_a),\end{aligned} \tag{14}$$

where V is the volume of the cavity, B_0 is the magnetic-field strength, Q_L is the cavity's loaded quality factor, $Q_a=10^6$ is the quality factor of the galactic halo axion signal (i.e., the ratio of axion energy to energy spread), ρ_a is the density of galactic halo axions on Earth, and C is a mode-dependent form factor given by

$$C=\frac{\left|\int_V d^3x\,\vec{E}_\omega\cdot\vec{B}_0\right|^2}{B_0^2V\int_V d^3x\,\epsilon|\vec{E}_\omega|^2}, \tag{15}$$

where $\vec{B}_0(\vec{x})$ is the static magnetic field, $\vec{E}_\omega(\vec{x})e^{i\omega t}$ is the oscillating electric field of the cavity mode in question, and ϵ is the dielectric constant. For a cylindrical cavity and a homogeneous longitudinal magnetic field,

$C=0.69$ for the TM_{010} mode. The form factors of the other TM_{0n0} modes are much smaller, and form factors for pure TE, TEM, and remaining TM modes are zero.

Because the axion mass is known only to within an order of magnitude at best, the cavity must be tunable, and a large range of frequencies must be explored in seeking a signal. The cavity can be tuned by moving interior dielectric rods or metal posts. The rate at which the mass region is swept out, either to find the axion at a given signal-to-noise ratio (SNR) or to exclude it at a given confidence level, is dictated by the Dicke radiometer equation (Dicke, 1946):

$$\mathrm{SNR}=\frac{P_a}{\overline{P}_N}\sqrt{Bt}=\frac{P_a}{k_B T_S}\sqrt{\frac{t}{B}}, \tag{16}$$

where $\overline{P}_N=k_B B T_S$ is the average thermal noise power, B is the bandwidth, and T_S is the sum of the physical temperature of the cavity plus the noise temperature of the microwave receiver that detects the photons from axion-to-photon conversion. For a given signal-to-noise ratio, the scanning rate is

$$\frac{df}{dt}=\frac{12\ \mathrm{GHz}}{\mathrm{yr}}\left(\frac{4}{\mathrm{SNR}}\right)^2\left(\frac{V}{500\ \mathrm{liter}}\right)^2\left(\frac{B_0}{7\ \mathrm{T}}\right)^4 \times C^2\left(\frac{g_\gamma}{0.36}\right)^4\left(\frac{\rho_a}{\frac{1}{2}\times 10^{-24}\ \mathrm{g/cm^3}}\right)^2 \times\left(\frac{3K}{T_S}\right)^2\left(\frac{f}{\mathrm{GHz}}\right)^2\frac{Q_L}{Q_a}. \tag{17}$$

Equation (16) makes plain that an arbitrarily small signal may be made statistically significant by increasing the signal power ($P_a \propto B_0^2 V$), decreasing the system noise temperature, or integrating for a longer time. For a practical search covering a mass range expressed in decades, the last approach is not an option. Technology and cost also limit improvements in either B_0 or V. Developing lower-noise amplifiers appears to be the most practical strategy for improving the experiment. From Eq. (17), there are two scaling laws to keep in mind for the experimental parameters one has control of, B_0, V, and T_S. (The cavity quality factor Q at cryogenic temperatures is limited by the anomalous skin depth of copper, and the theoretical maximum can be readily achieved.)

In a search for the axion with a given coupling g_γ, the logarithmic scan rate (appropriate for axion linewidth increasing with frequency) is

$$\frac{1}{f}\frac{df}{dt}\propto(B_0^2V)^2\cdot\frac{1}{T_S^2}. \tag{18}$$

On the other hand, in a search with a given logarithmic scan rate, the reach in model space g_γ^2 ($\propto$ conversion power) is

$$g_\gamma^2\propto(B_0^2V)^{-1}T_S. \tag{19}$$

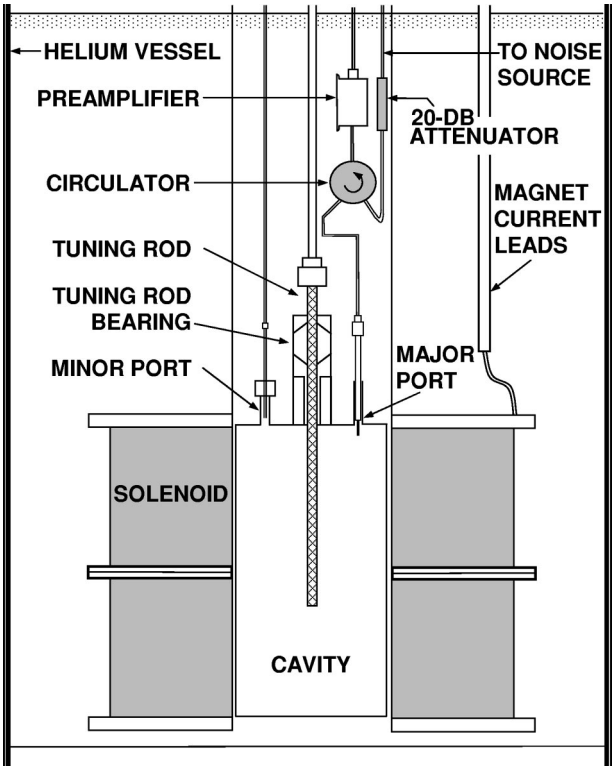

FIG. 2. Schematic of the Rochester-Brookhaven-Fermilab microwave cavity experiment (Wuensch *et al.*, 1989).

B. First-generation experiments

First-generation microwave cavity experiments were carried out at Brookhaven National Laboratory (BNL) and at the University of Florida. They demonstrated the feasibility of the technique over a significant range of frequencies, but fell short in power sensitivity by 100–1000 in efforts to detect halo dark-matter axions with plausible model couplings, due to their small volumes and relatively high noise temperatures.

1. The Rochester-Brookhaven-Fermilab experiment

A proof-of-principle experiment, located at BNL, was carried out by a collaboration of the University of Rochester, Brookhaven National Laboratory, and Fermi National Accelerator Laboratory (DePanfilis *et al.*, 1987; Wuensch *et al.*, 1989). A superconducting solenoid magnet provided a peak central field of 8.5 T within a useful cylindrical volume of roughly 15 cm diameter and 40 cm length. The cavity was constructed of high-purity oxygen-free copper, for which the unloaded quality factor in the 2–3-GHz range was $Q_W \sim 1.8\times 10^5$ at $T=4.2$ K, the operating temperature of the experiment. The cavity resonant frequency was tuned by means of a sapphire rod inserted longitudinally along the central axis of the cavity. A schematic of the Rochester-Brookhaven-Fermilab experiment is shown in Fig. 2.

The cavity field was sampled by a small coupling loop, isolated by a circulator, and fed to a cryogenic preamplifier. Various amplifiers were used with $T_N=8-15$ K, the *in situ* noise calibration being performed by a noise

source applied to the terminated port of the circulator. The amplified signal was mixed down in a double-heterodyne receiver and fed to a 64-channel filter-detector system used as a spectrum analyzer. Two sets of filters were used, one with 200-Hz bandwidth, the other with 400-Hz bandwidth. The 64-channel filter output was passed through a low-pass filter and the voltage digitized and recorded every 100 ms (the characteristic time of the low-pass filter). The six sets of cavity diameter and rod diameter combinations covered the frequency range of 1.09–3.93 GHz (4.5–16.3 μeV). A noteworthy detail in this experiment was the use of a higher-TM mode to extend the frequency range of the search, albeit at the cost of a greatly reduced cavity form factor C, and thus sensitivity. The Rochester-Brookhaven-Fermilab collaboration also developed an equivalent circuit analysis of a microwave cavity detector coupled to a noisy amplifier, which was critical for their analysis (Moskowitz and Rogers, 1988).

The criterion for a candidate axion signal was a peak in the cavity power spectrum of a certain number of standard deviations above the local mean power. Each frequency range was swept twice and a candidate peak was required to appear in both sweeps. Ultimately no peaks survived reexamination. Limits (95% C.L.) on $g^2_{a\gamma\gamma}$ GeV^2 were established of 5.7×10^{-28} at the low-mass end (4.5 μeV) to 1.8×10^{-25} on the high-mass end (16 μeV).

2. The University of Florida experiment

The other first-generation microwave cavity experiment was carried out at the University of Florida (Hagmann, Sikivie, Sullivan, and Tanner, 1990). The superconducting solenoid magnet (17.1 cm diameter, 40 cm length) produced a peak central field of 8.6 T. The cavities, made of high-purity oxygen-free copper, had an unloaded quality factor at 1.5 GHz of $Q_W\sim1.6\times10^5$, measured at 4.2 K physical temperature. The operating temperature of the experiment was normally 2.2 K. Coarse tuning was done by a large dielectric rod moved transversely in the cavity, and fine tuning by insertion of a small tuning rod inserted through a hole in the top plate of the cavity.

Power from the TM_{010} mode of the cavity was extracted by a small loop. The cavity and the cryogenic preamplifier were isolated by a circulator. The noise temperature of the HFET amplifiers varied between 3 and 7 K, depending on frequency. A double-heterodyne receiver mixed the amplified signal down to the 0–30-kHz range, where a PC-based analog-to-digital converter/fast Fourier transform calculated the power spectrum. The sampling rate of 70 kHz was slightly greater than the Nyquist bandwidth (see, for example, Siebert, 1986). Two cavities of different diameters, with both metal and dielectric tuning rods, allowed the frequency range of 1.32–1.83 GHz to be covered completely.

Unlike the Rochester-Brookhaven-Fermilab experiment, the University of Florida experiment was tuned in steps rather than continuously swept. In each 90-sec run, 10^5 subspectra were averaged to generate a 32-bin power spectrum of 1-kHz resolution. Any 2σ peak above the local mean power was rescanned. This was repeated up to four times and persistent candidates were flagged for further investigation later; none survived. Limits (97.5% C.L.) on $g^2_{a\gamma\gamma}$ GeV^2 were established of 3.3×10^{-28} at the low-mass end (5.46–5.95 μeV) to 1.2×10^{-27} on the high-mass end (7.46–7.60 μeV). Included in the University of Florida effort was electromagnetic modeling of the microwave cavities and exploration of concepts for much-higher-frequency resonators (Hagmann, Sikivie, Sullivan, Tanner, and Cho, 1990). In particular, power combining of two independent cavities was demonstrated at 300 K, as a first step towards multiplexing many small cavities of high frequency while utilizing a large magnetic volume (Hagmann, 1990). The exclusion regions from both the Rochester-Brookhaven-Fermilab and University of Florida experiments are displayed together in Fig. 3.

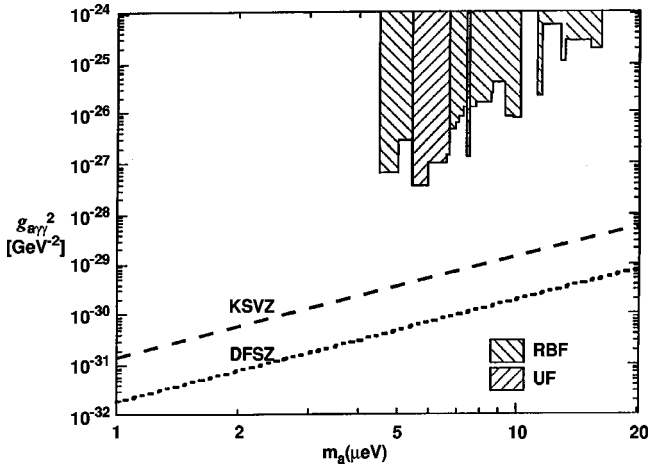

FIG. 3. Exclusion regions for the Rochester-Brookhaven-Fermilab (RBF) (DePanfilis *et al.*, 1987; Wuensch *et al.*, 1989) and University of Florida (UF) (Hagmann, Sikivie, Sullivan, and Tanner, 1990) experiments. Dashed line, model of Kim, Shifman, Vainshtein, and Zakharov (Kim, 1979; Shifman *et al.*, 1980); dotted line, model of Dine, Fischler, Srednicki, and Zhitnitskii (Dine *et al.*, 1981; Zhitnitskii, 1980).

C. Second-generation experiments

In the 1990s, two experimental efforts were mounted with the goal of improving the power sensitivity of the Sikivie microwave cavity experiment to reach plausible axion model couplings for the first time. While the essential features of the experiments were the same—resonant conversion of axions to photons in a microwave cavity permeated by a magnetic field—the two experiments diverged in their strategies for the actual signal detection. The U.S. experiment described in Sec. IV continued with improvements in coherent microwave amplifier technology and signal processing along with an increase in cavity volume. Section V gives a pedagogical discussion of amplifiers and the standard quantum limit.

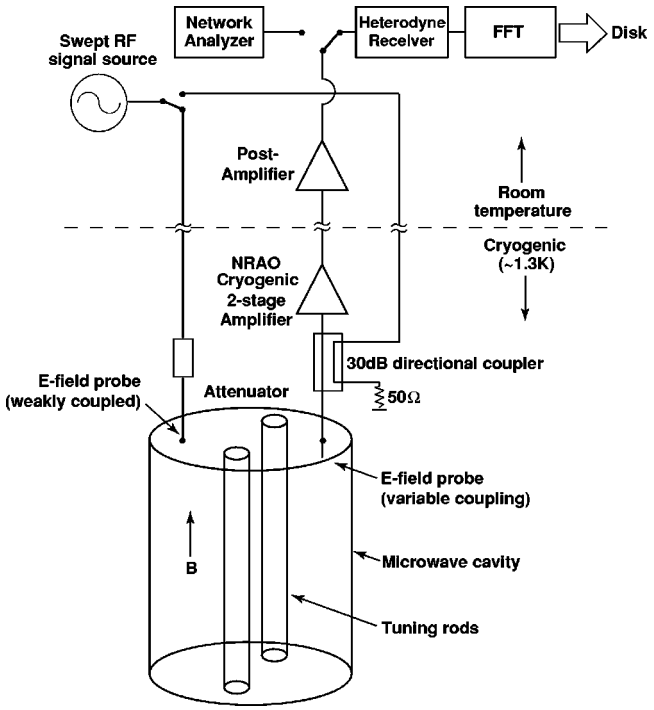

FIG. 4. Schematic of the U.S. search apparatus. From Asztalos *et al.*, 2001.

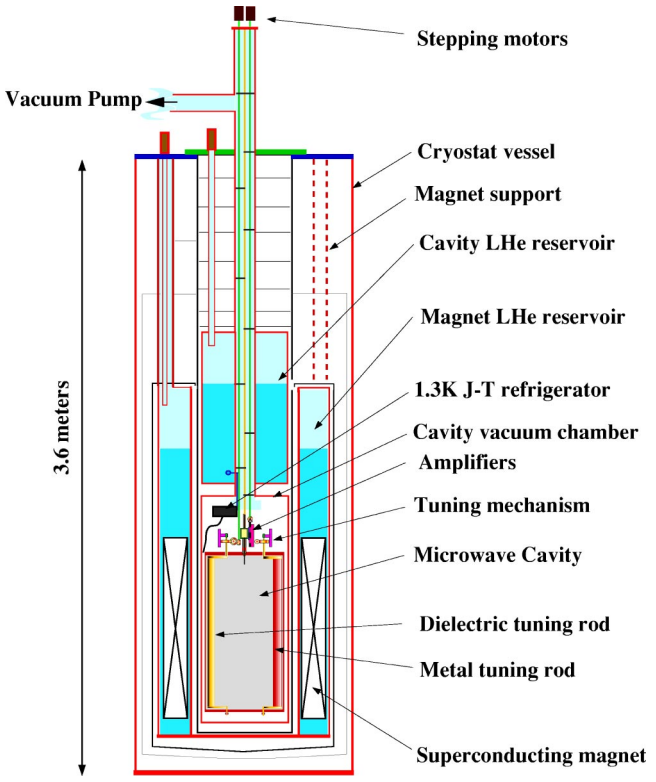

FIG. 5. (Color in online edition) Sketch of the U.S. experiment insert within the magnet system. The experiment insert can be withdrawn without warming the magnet. From Asztalos *et al.*, 2001.

Section VI discusses the development of microstrip SQUID amplifiers which will be used in the continuation of the U.S. experiment. The Kyoto experiment described in Sec. VII, however, opted to develop a Rydberg-atom single-quantum detector. The two efforts thus represent the classical "wave-particle" bifurcation of dealing with photons.

IV. THE U.S. LARGE-SCALE SEARCH

A microwave-cavity axion experiment is in routine operation at Lawrence Livermore National Laboratory (LLNL). This experiment, a collaboration of LLNL, MIT, University of Florida, Lawrence Berkeley National Laboratory (LBNL), U.C. Berkeley, University of Chicago, and Fermilab, has been operating since February 1996 and exploring the region from 0.3 to 3.0 GHz (1.2–12.4 μeV) at better than KSVZ sensitivity. We first present an overview of the experiment and its operation, followed by detailed discussions of the hardware, data analysis, and results.

Figure 4 is a diagram of the apparatus (Peng *et al.*, 2000). The heart of the axion detector is a cylindrical rf cavity containing two movable tuning rods aligned parallel to a strong solenoidal magnetic field. The cavity electromagnetic field is coupled through a small adjustable electric-field probe to ultralow-noise receiver electronics. These components are sketched in Fig. 5.

The cavity electromagnetic fields are coupled to the receiver chain by an electric-field probe with adjustable insertion depth (and, therefore, adjustable cavity loading). The signal from the cavity is amplified by two cryogenic HFET amplifiers in series, built by the National Radio Astronomy Observatory (NRAO). The overall power gain for the two cryogenic amplifiers is approximately 34 dB. The first set of amplifiers used in data taking had a noise temperature of about 4.3 K. Recent amplifiers have noise temperatures better than 2 K. The output of the cryogenic amplifiers is amplified by a low-noise room-temperature amplifier with about 38-dB gain and then sent to the receiver.

The receiver has a double-heterodyne design influenced by experience gained in the earlier University of Florida experiment. The first down-conversion stage, by image rejection mixing, generates a 10.7-MHz intermediate frequency. A crystal bandpass filter in the 10.7-MHz intermediate frequency rejects power outside a 35-kHz frequency window centered on the cavity resonant frequency. A second conventional mixing stage down-converts the 10.7-MHz intermediate frequency to near audio frequency centered at 35 kHz. The audio signal is analyzed by commercial fast-Fourier-transform (FFT) electronics, which compute a 50-kHz bandwidth power spectrum centered at 35 kHz.

The normal data-taking sequence starts by moving the tuning rods incrementally to establish a new cavity resonant TM_{010} frequency. The electromagnetic power spectrum around the cavity TM_{010} mode is then determined by the receiver electronics and FFT instrumentation.

The thermalized axion signature is excess power above the background power spectrum concentrated in a peak of bandwidth of order 1 kHz (about six fre-

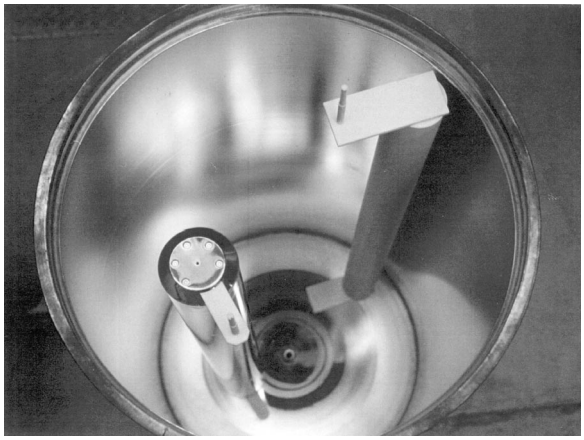

FIG. 6. The resonant cavity viewed from above with the top flange removed. The cavity is a right circular cylinder of diameter 50 cm and depth 1 m. An alumina tuning rod is at the upper right, a copper tuning rod is at the lower left. From Asztalos *et al.*, 2001.

quency bins wide). The dominant background sources are relatively broadband cavity blackbody noise and broadband electronic noise from the first cryogenic amplification stage.

A. Hardware

A sketch of the U.S. axion search experiment apparatus is shown in Fig. 5. The magnetic field is produced by a superconducting solenoid consisting of niobium-titanium windings immersed in a liquid-^{4}He cryostat. The axial field at the center of the solenoid was 7.6 T, falling to about 70% of this value at the cavity end plates. More recently, the magnet has been run in excess of 8.2 T.

The cavity is at the bottom of the insert. A large "Roots blower" pumps on a shallow helium pool below the cavity, thus cooling the cavity to a physical temperature of 1.3 K, reducing the blackbody noise. To fill in small frequency gaps that are otherwise inaccessible, e.g., mode-crossing regions described later, the liquid-helium pool is allowed to rise until the entire cavity is filled.

1. Cavity and tuning rods

The resonant cavity consists of a copper-plated stainless-steel right-circular cylinder 1 m long and 50 cm in diameter with two end plates. The cavity volume is $\sim$200 liters. The cavity components are plated on all major surfaces with high-purity oxygen-free copper, then annealed. Both metal and dielectric tuning rods were designed for use in the experiment. The rods are mounted at the end of alumina swing arms, which pivot about alumina axles that penetrate the top and bottom end plates of the cavity. By rotating these axles, one may swing the tuning rods in circular arcs from close to the cavity side wall to close to the center. Metal rods increase the frequency of the cavity, whereas dielectric rods decrease it. Figure 6 is a photograph of two tuning rods within the cavity. The axles and arms used to move the tuning rods are visible. In this picture, the upper right tuning rod is made of low-loss alumina. The first data-taking run used two copper tuning rods, each similar to the lower left rod in the picture, 8.25 cm in diameter. The tuning rods are driven by stepper motors mounted on top of the cryostat through a two-stage antibacklash gear reduction mounted on the cavity end plate. There are 8.4 million motor steps per full revolution, with a single step corresponding to a change in the angle of the tuning rod by 0.15 arc sec. The resulting frequency tuning precision is about 1 kHz at a resonant frequency of 800 MHz.

The Q of the TM_{010} mode is determined from the transmission response. A swept rf signal is applied through the very weakly coupled rf calibration port on the top plate of the cavity, and the transmitted signal from the major port is directed to a scalar network analyzer. In general, the unloaded Q of the cavity is $\sim 2 \times 10^5$.

The scan rate at constant signal-to-noise ratio depends on the coupling of the external amplifier to the cavity, with a broad maximum at slightly over critical coupling. Hence, during normal data taking, the insertion depth of the major port electric-field probe was periodically adjusted to maintain critical coupling between the cavity TM_{010} mode and the receiver chain. A cryogenic directional coupler is used to measure the power reflected from the cavity; when the probe is critically coupled, essentially no power is reflected at the cavity resonant frequency.

2. The cavity mode structure and form factor

There is a complicated mode structure within the cavity. A cylindrical cavity supports both TE and TM modes, with or without tuning rods, and TEM (coaxial) modes when metallic tuning rods are introduced. There are in addition hybrid modes associated with deviations from a uniform cross section. The cavity itself is not a perfect circular cylinder, and the insertions and tuning rods also distort the cylindrical geometry; thus there is considerable mixing among modes. Consequently there is no sufficiently accurate closed analytic form for the cavity mode structure, so the form factor C is estimated by numerical simulation.

With a cavity containing two metal tuning rods, the TM_{010} mode appropriate for this geometry has lowest frequency when both copper rods are nearest the wall. As one or both rods approach cavity center, the frequency increases. Figure 7 (upper panel) shows the frequencies of various cavity modes versus tuning rod positions for the case of one rod fixed near the wall and the other moving towards the center. The vertical axis is cavity frequency f_0 and the horizontal axis is number of stepper motor steps from a rod position near the wall. These mode maps were obtained by feeding a swept rf signal into the cavity through the weakly coupled rf port and measuring the transmitted power. The TE and TEM

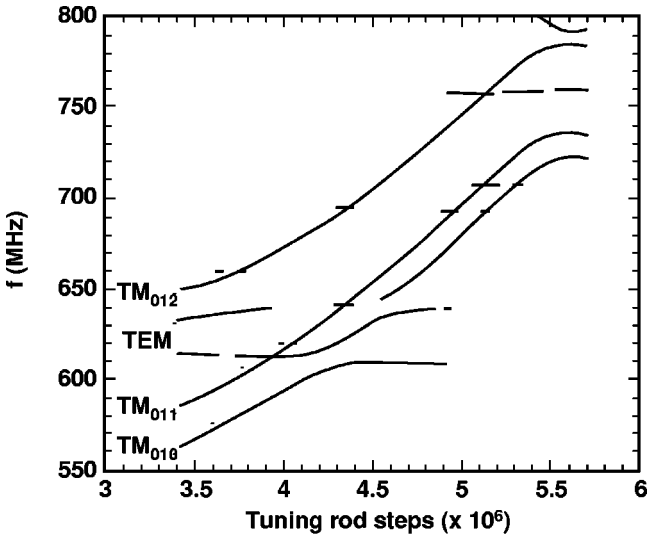

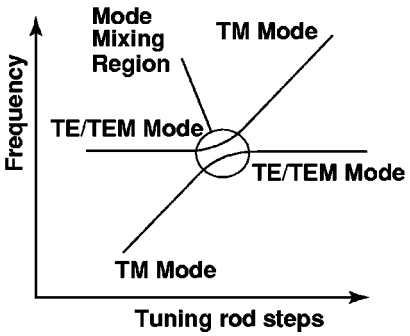

FIG. 7. Cavity mode structure with two metal tuning rods: upper panel, the cavity mode structure with one rod fixed near the wall and the other rotating towards the cavity center. The horizontal axis is the rod position in units of stepper motor steps. Lower panel, sketch of an avoided mode crossing. From Asztalos *et al.*, 2001.

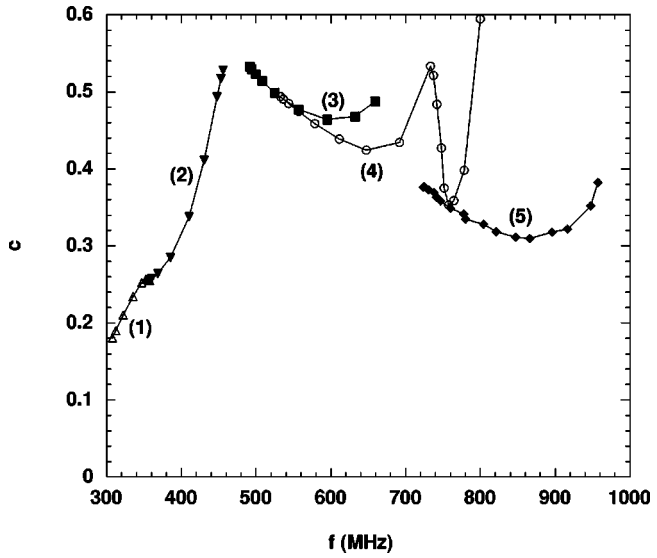

FIG. 8. The frequency dependence of the form factor. The horizontal axis is the cavity resonant frequency, the vertical axis is the form factor C_{010}. The curves show the form factor for different tuning rod materials and rod geometries: (1) two alumina rods ($\epsilon=9.5$), ratio of rod diameter (r) to cavity dimeter (R) $r/R=0.13$, one rod fixed at cavity center; (2) two alumina rods, $r/R=0.13$, one rod fixed at cavity center; (3) one metal rod, $r/R=0.16$; (4) two metal rods, $r/R=0.16$, one rod fixed at wall (for the 500–700-MHz range) or fixed at the cavity center (for the 700–800-MHz range); (5) two metal rods, the $r/R=0.16$ rod fixed at the cavity center, the $r/R=0.3$ rod moving. From Asztalos *et al.*, 2001.

modes of the cavity are only weakly excited by the rf probes oriented perpendicular to the TE and TEM electric fields.

Notice that there are mode crossings (mixings) in the various TM modes. These crossings occur when the frequencies of two modes are nearly degenerate and the modes mix. The mode crossings introduce frequency gaps that are not well modeled by a pure TM_{010} mode. These gaps were scanned by filling the cavity with liquid helium at 1.3 K. Liquid helium has a relative dielectric permittivity of 1.055, hence it alters the microwave index of refraction by a factor of 1.027. The frequencies of all the modes of the cavity and the mode crossings are therefore decreased by 2.7%, or 19 at 700 MHz. By combining data taken when the cavity is filled with low-pressure gas, as is normally the case, with data taken when the cavity is filled with helium, the entire frequency range is covered without gaps. There is a slight penalty in filling the cavity with helium, as the reduced electric field gives a lower axion conversion rate.

The form factor C_{010} of the TM_{010} mode, defined in Eq. (15), is calculated from a numerical solution of the wave equation for the axial component of the electric field E_z in the cavity, including tuning rods. The resultant axial electric field is combined with the calculated magnetic-field shape (calculated from the actual magnet winding current density) to yield Fig. 8, a plot of the form factor versus TM_{010} resonant frequency for different tuning rod materials (metallic and dielectric) and rod diameters.

B. Balanced heterostructure field-effect transistor amplifiers

The characteristics of the cryogenic amplifiers are particularly important because their noise dominates the system noise temperature of a microwave cavity experiment. The active device used in such amplifiers is the heterostructure field-effect transistor (HFET). Due to its higher carrier mobility, lower impurity scattering, and smaller separation between the gate and the transport channel as compared with the conventional field-effect transistor, it has become the mainstay device for very-low-noise cryogenic amplifiers operating throughout the microwave band and well into millimeter wavelengths.

Figure 9 is a photomicrograph of the Fujitsu FHX13X HFET chip used in the NRAO balanced amplifiers. The most notable features of the chip are the relatively large wire bonding pads for the source, drain, and gate contacts. The HFET structure is located directly under the

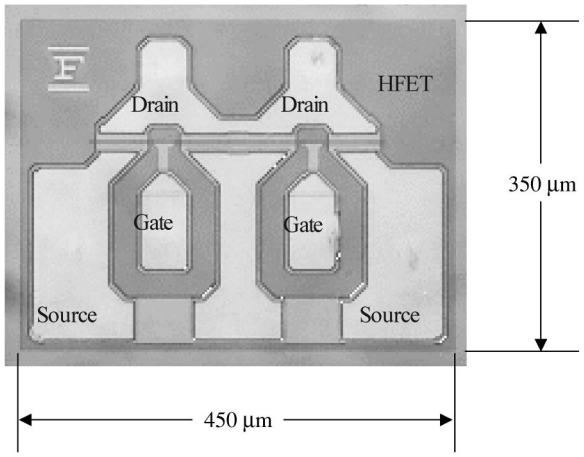

FIG. 9. Photomicrograph of the Fujitsu FHX13X heterostructure field effect transistor (HFET) chip showing the gate source and drain electrodes. From Bradley, 1999.

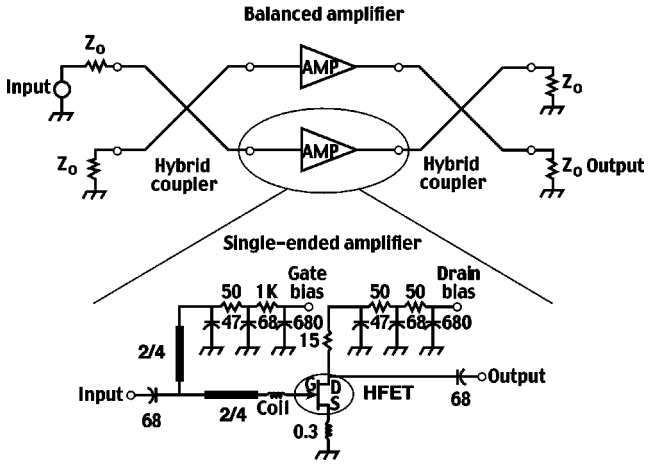

FIG. 10. Schematic diagram of the balanced HFET amplifier (top) with an expanded view of the single-ended amplifier (bottom). Resistances are in ohms, capacitances are in pF, and inductances are in nH. From Bradley, 1999.

long, thin gate metallization, as shown. The gate length is 0.25 μm and the gate width is 300 μm. The HFET heterostructure achieves spatial separation between the conduction electrons of the two-dimensional electron gas at the heterointerface and the donor ions in the heavily doped $Al_XGa_{1-X}As$ layer. Electrons diffuse across from the $Al_XGa_{1-X}As$ into the GaAs layer, where the electron motion is restricted to the two dimensions parallel to the heterointerface, forming the 2D electron-gas channel between the source and the drain. A Schottky barrier gate is used in the depletion mode "normally on" HFET (the type commonly used for microwave amplifiers). The depletion of the Schottky gate should just merge with the interface depletion to avoid conduction through the $Al_XGa_{1-X}As$, which has inferior transport properties. Modulation of the gate-to-source voltage causes a corresponding modulation in the drain-to-source current. The HFET is therefore classified as a voltage-controlled current source described by a transconductance, g_m.

The source contact of the HFET is normally the common terminal in the microwave small-signal amplifier configuration. The gate-to-source input is matched to the 50-Ω input using as few components as possible—usually a transmission line transformer and a series inductance. A small amount of inductive source feedback is generally required to enhance stability. Since the input resistance that minimizes the noise temperature of the amplifier is often much different than 50 Ω, the input reflection coefficient is commonly quite large for such low-noise amplifiers. As a result, a single-ended low-noise amplifier that is critically coupled to a high-Q cavity will tend to oscillate unless an isolator or other nonreciprocal device is placed between them. However, there are practical difficulties in using such ferrite devices in large ambient magnetic-field environments such as that encountered in the cavity experiment.

The balanced amplifier, first introduced by Kurokawa (1965), provides simultaneous power and noise match over an octave or more bandwidth without the use of a nonreciprocal device, yielding better amplifier stability without compromising the noise performance. A circuit diagram is shown in Fig. 10. This balanced design is realized by a matched pair of single-stage HFET amplifiers, with single-pole impedance-matching networks at the inputs. The input signal to the balanced amplifier is split into two paths by a 90° hybrid (one path phase shifted by 90° with respect to the other). Each path is then amplified and recombined by another 90° hybrid, essentially reversing the initial phase shift. Any reflection from the input from one path is canceled by the phase-shifted reflection from the other path. The reflection is instead directed to a termination resistor located at the fourth port of the input hybrid.

A suite of five low-noise, balanced, GaAs HFET amplifiers covering the 300–1200-MHz band with noise temperatures in the range of 1.5–4 K have been developed at the NRAO primarily for use in radio astronomy. Fortuitously, these same amplifiers were ideal for the U.S. axion experiment. The amplifier is housed in a gold-plated brass enclosure measuring $8.26\times4.53\times2.08\ \mathrm{cm}^3$, with coaxial rf connectors for the input and output and a nine-pin connector for the bias. Microstrip transmission line structures are used throughout. The circuit board material is low-loss RT/duroid ($\epsilon_r=10.5$ at 300 K) by Rogers Corporation. The input and output 90° hybrids are Lange-type (Lange, 1969) couplers that are meandered to reduce their physical size. The pair of FHX13X HFET chips are located adjacent to the copper coils. Noise temperature and gain for this amplifier operating at a physical temperature of 14 K are shown in Fig. 11. Measured input return loss is better than 20 dB. Recent dynamic range measurements are shown in Fig. 12.

Three balanced amplifiers, covering the 800–2000-MHz band, are currently under development at NRAO. These amplifiers are very similar in overall structure to the lower-frequency versions with the exception of the HFET's which are Mitsubishi MGFC4419G having a gate length of 0.25 μm and a gate width of 250 μm. Early measurements on the 1150–1650-MHz amplifier

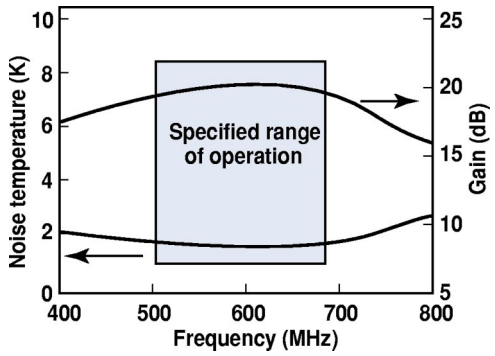

FIG. 11. (Color in online edition) Measured noise temperature and gain of the 510–690-MHz balanced amplifier at 14 K. From Bradley, 1999.

show a noise temperature of about 3 K (at 14 K physical) with a power gain of approximately 18 dB, with further reductions in noise temperature expected.

The orientation of the amplifier during the production data taking is such that the magnetic field is parallel to the HFET channel electron flow. During commissioning it was observed that if the cryogenic amplifier were rotated so the magnetic field was perpendicular to the electron flow in the HFET junctions, the amplifier noise temperature rose from 4.6 K to around 8 K. A simple model for the magnetic-field dependence is that the Lorentz force on the electrons in the HFET junctions distorts the electron paths so that their trajectory across the gate region lengthens. In the simplest version of the model, the HFET amplifier noise temperature is proportional to the length of the electron path through the gate. The model predicts an increase in noise temperature consistent with that observed (Daw and Bradley, 1997).

C. Receiver electronics

The output of the cryogenic amplifiers is carried by a cryogenic coaxial cable to a low-noise room-temperature postamplifier mounted in a room-temperature rf-shielded enclosure on top of the cryostat. The power gain of the postamplifier is about 38 dB in the frequency range 300 MHz–1 GHz, with noise temperature around 90 K. The power gain of the two cryogenic amplifiers in series is 34 dB, hence the contribution of the postamplifier to the system noise temperature is negligible, less than 0.03 K. The total power gain from cavity probe to the postamplifier output is 69 dB (8×10^6); with this gain, the noise power from the cavity and amplifier at the postamplifier output in a 125-Hz bandwidth is 8.3×10^{-14} W.

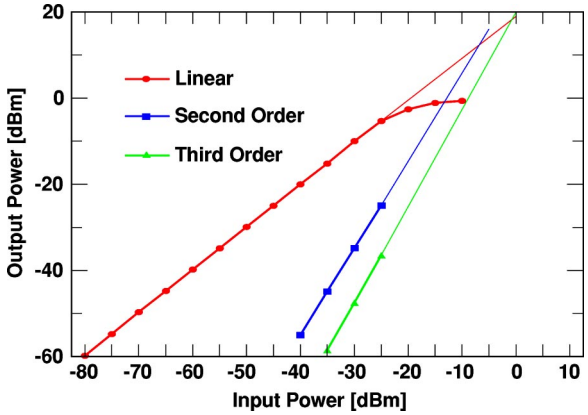

FIG. 12. (Color in online edition) Dynamic range measurements.

The amplified rf signal from the detector then enters the double-heterodyne section of the receiver. Figure 13 is a block diagram of the receiver intermediate-frequency and audio-frequency processing components.

The first component in this section is an image rejection mixer; it shifts rf power from the TM_{010} resonant frequency to an intermediate frequency range centered at 10.7 MHz while rejecting image noise power from this range. During normal running, the local oscillator frequency is maintained at 10.7 MHz below the measured cavity resonant frequency so that the cavity resonance is centered at 10.7 MHz in the intermediate-frequency strip.

The intermediate-frequency section has a crystal bandpass filter to suppress noise outside a 30-kHz bandwidth centered on the 10.7-MHz intermediate frequency. Out-of-band power would otherwise have been aliased in the audio-frequency output by the next mixing stage. On account of the strong dependence of the receiver transfer function on the filter's response, the filter is enclosed in a temperature-controlled oven maintained at $40\pm0.5\,^{\circ}$C. After another 20 dB of amplification, the intermediate-frequency signal is mixed down again to near audio frequency in the range 10–60 kHz. The output of the second mixer leads to a commercial FFT spectrum analyzer, and the resulting single-sided power spectra are saved to disk as the raw data. The frequencies of the local oscillators are stabilized to drift less than ±0.005 Hz by a cesium frequency reference. The frequency stability of the receiver chain is established *in situ* by noting that occasional large external radio peaks drift in frequency by less than ±0.02 Hz.

The receiver response, including the filter, is calibrated by measuring the receiver output spectrum with a white-noise source at the input. Noise generated by a broadband noise source is injected at the rf input of the image rejection mixer. At the output of the receiver, the FFT spectrum analyzer takes and averages many 400-point single-sided power spectra (125 Hz per point) of the filter passband response.

The search for axionlike signals in the data is affected by even very small drifts in the receiver response. A typical integration time for the acquisition of a single averaged FFT power spectrum (containing 10^4 individual spectra, described in the next section) is 80 sec. Hence fluctuations in the power spectrum are expected to be $1/\sqrt{10\,000}$ of the raw noise power.

The FFT spectrum analyzer in this experiment operates at an effective sampling rate of 100 kHz. Every 8 msec, an individual single-sided spectrum (one in which

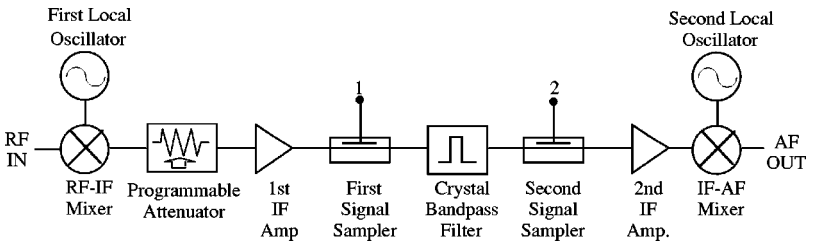

FIG. 13. Simplified schematic of the intermediate-field (IF) and near-audio-frequency (AF) components in the receiver chain. From Asztalos *et al.*, 2001.

the negative and positive frequency components are folded on top of each other) is taken with uniform (flat) windowing consisting of 400 bins, each 125 Hz wide, spanning the frequency range 10–60 kHz. Over 80 sec of integration time per frequency setting, 10 000 such individual spectra are taken and averaged and the averaged spectrum is saved as raw data. This is referred to as the medium-resolution data. Figure 14 shows a typical averaged power spectrum taken during production running.

The most obvious feature of this spectrum is the rapid falloff in power at the limits of the 20–50-kHz frequency range at the skirts of the intermediate-frequency crystal filter bandpass response. There is a slight difference in noise power levels on and off resonance; the noise power on resonance (where the cavity noise source dominates) is less than the noise power off resonance (where internal noise sources in the amplifier dominate). Understanding the underlying structure of the raw data spectra is important because the expected axion signal appears as additional structure above noise background across several adjacent bins in the power spectrum. This structure can be modeled very well using an equivalent circuit for a noisy amplifier coupled to a single cavity mode by a length of transmission line (Peng *et al.*, 2000).

There is in addition a dedicated electronics channel optimized for the detection of extremely narrow lines from late-infall axions (see Sec. II.D). For this case, the audio-frequency cavity signal (centered at 35 kHz) is sent through a passive LC filter (passband $\simeq 6.5$ kHz), amplified, and mixed down to a 5-kHz center frequency. The signal is applied to an analog-to-digital converter/digital signal processor (DSP) board in a PC host computer, where it is oversampled at 20 kHz by a 16-bit analog-to-digital converter and stored in DSP memory. A single spectrum is obtained by acquiring 2^{20} (approximately 1 million) points in about 53 sec, performing the FFT calculation in about 8 sec, and uploading the 2^{19}-point power spectrum to the PC host for analysis. This is referred to as the high-resolution data.

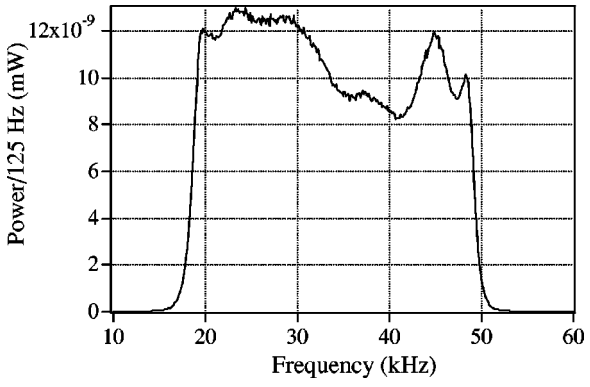

FIG. 14. A typical power spectrum from the raw data. The vertical axis is spectral density at the AF output. The mixed-down cavity resonant frequency is near the center of the frequency range. The obvious structure is due to the filtering in the receiver.

About 3.4×10^5 points lie in the 6.5-kHz passband with a frequency spacing of 19 mHz. In order to have higher sensitivity for lines of intermediate width, nonoverlapping segments of 8 and 64 points were averaged, resulting in two additional power spectra of resolution 152 mHz and 1.2 Hz, respectively.

D. Data and analysis

The medium-resolution data from this experiment were analyzed to search for dark-matter axions under two hypotheses (Asztalos *et al.*, 2001). The first hypothesis (the "single-bin" search) is motivated by the possibility that at least some halo axions may not have thermalized and therefore would have a negligible velocity dispersion; these axions would deposit their energy into a single power-spectrum bin. The second hypothesis (the "six-bin" search) makes no assumption about the halo axion energy distribution other than a velocity dispersion of $\mathcal{O}(10^{-3}c)$ or less, consistent with the best-fit virial velocity from all observations. (Axions with velocity larger than about 2×10^{-3} would escape from the halo.) The results from the six-bin search are the most conservative, since they are valid whether or not the halo axions have thermalized, completely or in part. Both searches incorporate a simple power excess in the search statistic. The axion search using an extremely narrow line channel is outlined at the end of this section.

1. The medium-resolution search

For the single-bin search, individual 125-Hz frequency bins exceeding a prescribed power-level threshold are selected from the combined power spectrum. The threshold is chosen relatively low, resulting in a considerable number of candidates. For the frequency bins above threshold, a second, independent, set of raw data are taken with the same integration time. This new data set is combined with the first, producing a single combined power spectrum with higher signal-to-noise ratio at the selected candidate frequencies. The selection process is repeated; individual frequency bins exceeding a power-level threshold are selected from the new combined power spectrum, and so on. The few surviving

candidates are carefully checked as to whether they are identified with known sources of external interference. If all candidates were to be identified with external interference, then no candidates would survive and the excluded axion couplings would be computed from the near-Gaussian statistics of the single-bin data.

For the six-bin search, all six adjacent frequency bins exceeding a power-level threshold are selected from the combined power spectrum, again resulting in a large number of candidates. (These candidates are correlated with candidates from the one-bin search.) This search thereafter proceeds similarly to the single-bin search. Should all candidates be identified with external interference, then no candidates survive and the excluded axion couplings are computed by Monte Carlo techniques. For details see Asztalos *et al.* (2001).

2. The high-resolution search

According to the radiometer equation, the search sensitivity can be increased if strong and narrow spectral lines exist.

For nominal experimental conditions, the integration time for each tuning rod setting is around 60 sec. The fractional Doppler shift due to the Earth's rotation in this time is $\sim 10^{-12}$ and amounts to $\sim$mHz (less than the inverse integration time).

Besides the highest-resolution spectrum of bandwidth 19 mHz, two more high-resolution spectra (of Nyquist resolutions 152 and 1200 mHz) are formed by combining adjacent bins of the highest-resolution spectrum. The three high-resolution spectra were examined for peaks on-line by calculating the mean and standard deviation of each 100-bin-wide segment. Bins with an excess of 11σ in the nonaveraged spectrum and excesses of 5σ and 4σ in the two lower-resolution spectra (152-mHz and 1.2-Hz bin width, respectively) were identified and saved for further analysis.

After completion of all frequency scans, the frequency coverage was fairly uniform, with every frequency sampled several times. Any undersampled regions were rescanned separately to achieve a minimum of four samples at each frequency.

In order to reduce the number of candidate peaks, a coincidence search was performed. Since the contributing spectra were generally taken at different times, the annual frequency modulation of the narrow axion lines must be considered. The peaks were required to fall within a variable frequency window of size $\Delta f/f = 4 \times 10^{-7} |\sin(\pi \Delta t/365 \text{ days})|$, where Δt is the time separation.

To reduce the number of candidates for subsequent rescans, the thresholds for coincidence pairs at the three resolutions were set to 15σ, 8σ, and 5σ, respectively. This produced a total of several hundred candidate frequencies for the three resolutions. Each peak was later examined by taking six additional spectra. If the peak persisted, further tests were performed, similar to the six- and one-bin searches, by disconnecting or attenuating various diagnostic coaxial cables leading into the experiment Dewar. Some spurious peaks disappeared with this procedure, while the remainder were matched to strong narrow-band signals in the environment.

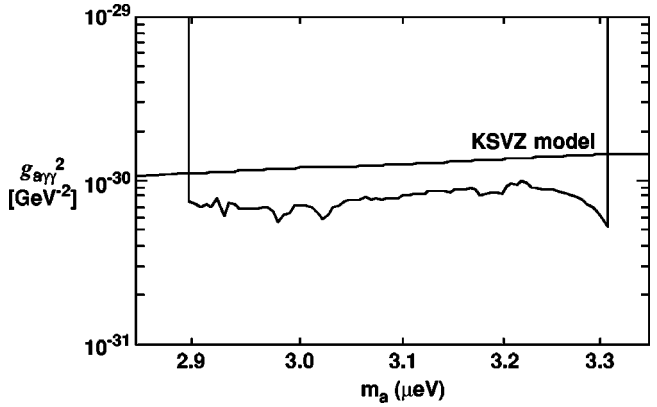

FIG. 15. Axion-photon couplings excluded at 90% confidence level, assuming the axion spectral line is significantly narrower than 125 Hz. From Asztalos *et al.*, 2001.

The minimum detectable power in a bin of bandwidth B is given by $P_{\min} = k_B T_s B N_\sigma$, where N_σ is the number of standard deviations above the mean. Because the signal could fall between two bins, the detectable power is smaller than $P_{\min}$. A simulation shows that at an approximate 90% confidence level and with the signal frequency falling randomly between two bin frequencies, the least power in the stronger of the two bins for two out of four trials is $0.7 \times P_{\min}$. Thus the minimum detectable conversion powers for the three different resolutions are approximately $P_{\min} \simeq 3 \times 10^{-23}$ W, 5×10^{-23} W, and 9×10^{-23} W, respectively, assuming a system noise temperature of $T_s \simeq 5.5$ K. This represents sensitivity to approximately 10%, 17%, and 30% of the total KSVZ axion signal power, respectively.

E. Results of the U.S. experiment

The medium-resolution single-bin peak search is most sensitive to signals with a bandwidth less than 125 Hz. The search statistic is a power excess in any single 125-Hz frequency bin of the combined data. It was assumed that the distribution of single-bin power excesses in single bins of the combined data is purely Gaussian, so that the sensitivity to axions in this channel can be calculated analytically.

All of the candidates surviving the rescan process were rejected. Figure 15 shows the resulting axion-photon couplings excluded as a function of axion mass at 90% confidence level assuming an axion line significantly narrower than 125 Hz and a halo density of 0.45 GeV/cm^3.

The sensitivity to axions in the six-bin search is deduced from the results of a Monte Carlo simulation. The signal power in the cavity is proportional to the square of the axion-photon coupling constant $g_{a\gamma\gamma}^2$, which together with the relation between axion mass and PQ symmetry-breaking scale gives the following expression for the limit on $g_{a\gamma\gamma}^2$ imposed by this experiment:

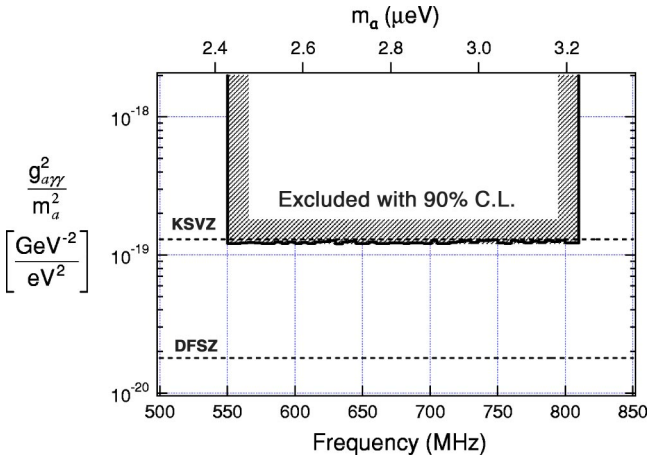

FIG. 16. (Color in online edition) The range of $g^2_{a\gamma\gamma}$ excluded at 90% C.L. by the six-bin search. KSVZ refers to one choice of Peccei-Quinn charges in a "hadronic" model (Kim, 1979; Shifman, Vainshtein, and Zakharov, 1980) and similarly for DFSZ in a more generic model (Zhitnitskii, 1980; Dine, Fischler, and Srednicki, 1981).

$$g_{a\gamma\gamma}(\text{excluded})^2 = (3.6\times 10^{-10}\ \text{GeV}^{-1})^2 \times\left(\frac{m_a}{1\ \text{eV}}\right)^2 \frac{P_{90}}{P_{\text{KSVZ}}}, \tag{20}$$

where P_{KSVZ} is the power expected in the KSVZ axion model (Kim, 1979; Shifman *et al.*, 1980), and P_{90} is the signal power excluded at 90% C.L.

Figure 16 shows the range of $g^2_{a\gamma\gamma}$ excluded at 90% C.L. by the six-bin search; note that the independent variable has been divided by m_a^2 to flatten the exclusion line. Also shown are the KSVZ and DFSZ (Zhitnitskii, 1980; Dine *et al.*, 1981) model predictions. This experiment has achieved an improvement in sensitivity of two orders of magnitude over previous experiments and is the first such search to probe realistic axion models.

This experiment has analyzed the data from an astrophysical perspective as well. Specifically, constraints have been placed on the local axionic halo density, having fixed the model axion-photon coupling (Asztalos *et al.*, 2002). Figure 17 shows the halo densities excluded for two well-developed models. For one implementation of the hadronic axion (designated KSVZ), it excludes the best maximum-likelihood estimate of 0.45 GeV/cm^3 (Gates, Gyuk, and Turner, 1995). For a GUT-inspired model (designated DFSZ), this constraint weakens to 3.0 GeV/cm^3. Note that the mass range covered by the U.S. search is currently 550–810 MHz (2.3–3.4 μeV).

F. Higher-frequency resonators

In addition to reducing the noise temperature of the experiment, advances should be made towards extending the search to higher mass and thus frequency. All experiments to date have been conducted between 2 and 20 μeV; a definitive search requires one to scan another factor of 50 higher in frequency.

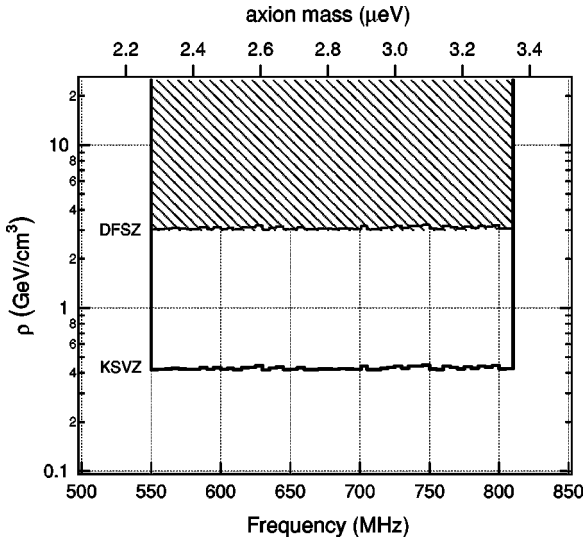

FIG. 17. Axionic halo density excluded 90% C.L. by the U.S. large-scale dark-matter axion search (Asztalos *et al.*, 2002), fixing the model axion-photon coupling.

The TM_{010} cavity mode is uniquely suited for an axion experiment; it has the highest "form factor" $C\sim 0.69$, i.e., the overlap integral between the external magnetic field and the electric field of the mode. (We assume a cylindrical geometry for the cavity, whose axis is collinear with the solenoidal magnetic field.) The value of C for any other mode is either much smaller or identically zero. The frequency of this mode is given by $f_{010} = 115\ \text{MHz}/R[m]$, or 460 MHz (1.9 μeV) for the single-cavity radius $R=0.25$ m used in the large-scale U.S. experiment. Radial translation of metal or dielectric rods can be used to tune the cavity by characteristically $\pm 50\%$ without undue degradation of C^2Q, the overall cavity figure of merit. Thus cavities of 100 mm diameter are required to probe the 10-μeV (2.4-GHz) axion mass region, 10 mm for 100 μeV, etc.

In order to fully utilize the volume V of the solenoidal magnet bore, multiple cavities can be packed together and power combined. This proposal was worked out by Hagmann (1990) for the case of two cavities and prototyped at room temperature. The salient feature is that the power from axion conversion adds linearly. So long as the cavities are tuned to exactly the same frequency, their outputs are summed in phase, and the axion frequency is sufficiently low so the axion de Broglie wavelength λ_d is larger than the cavity array; see Fig. 18. (As $\lambda_d = h/p_a \sim 10$–$100$ m is typically much greater than the size of the cavity array $D\sim 1$ m, the axion field drives the cavity array coherently, analogously to a multiple-slit experiment.) A four-cavity array was constructed and operated in the U.S. experiment (Figs. 19 and 20), achieving sensitivity to KSVZ model axions, at least over a very narrow notch in frequencies (Kinion, 2001). Reliability and increased complexity of operation were already significant factors for four cavities, and one should be wary of the strategy of deploying multiple independently tunable cavities for an axion experiment at higher frequencies, particularly when the number N would seem to scale as f^2. There are other difficulties. When the height of the cavity exceeds twice the diam-

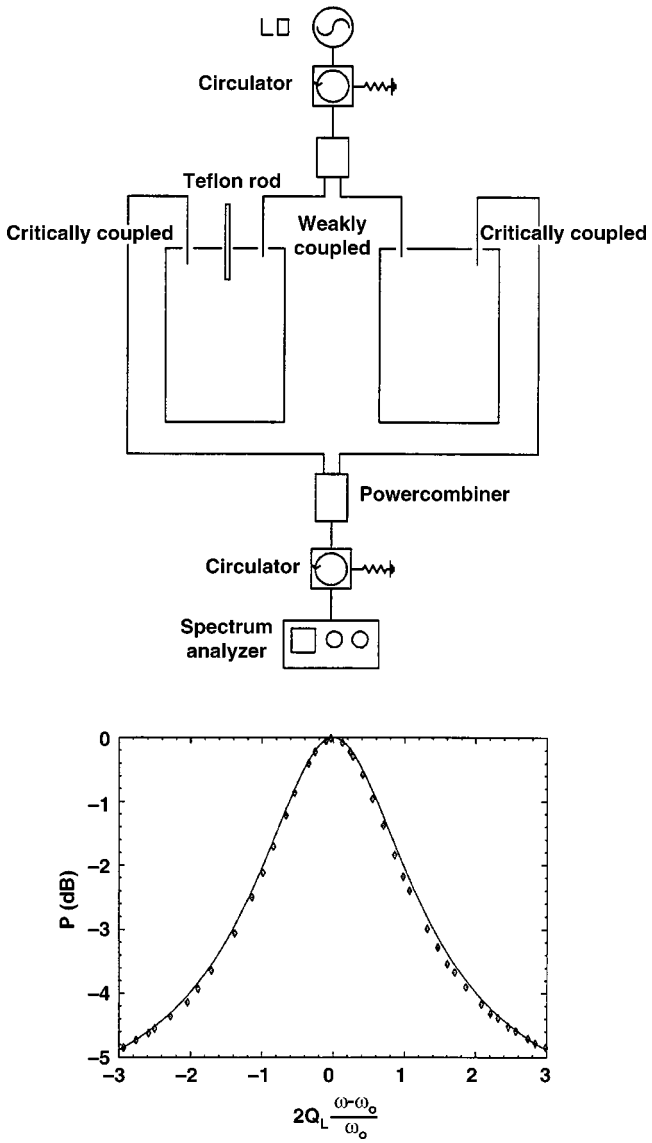

FIG. 18. Two-cavity power combining demonstration: upper panel, schematic of a two-cavity test; lower panel, measured and predicted power as a function of the frequency difference between the two cavities. From Hagmann, 1990.

eter, the TM_{010} mode is no longer the lowest mode, and as the aspect ratio of the cavity becomes larger, a whole thicket of TE modes (and TEM modes too, with metal tuning rods) intrudes on the search region, and the number of TM-TE mode crossings gets out of hand. Requiring that the cavities not exceed a certain reasonable aspect ratio (4:1 or so) then implies the scaling $N \propto f^3$. Combining more than four cavities does not seem practical, and a different way must be sought.

A potential line of investigation would be to employ resonators with a periodic array of metal posts. Figure 21 shows the calculated electric field for the TM_{010}-like mode, with a 19-post hexagonal array. The desired feature is achieved, namely, its frequency is characteristic of the lattice spacing and not the diameter of the resonator. By mounting alternate posts from the top and bottom ("stalactites" and "stalagmites") and moving them relative to one another, tuning of the array over some tens of percent is effected by a global relative translation. A prototype resonator with a 6×6 array of posts interdigitated with a 7×7 array of posts has borne out this strategy. To keep the TM_{010}-like mode relatively free from interloper TE or TEM modes, the height of the resonator must not greatly exceed the lattice spacing; however, this still results in a much more tractable f^1 number-of-cavities scaling rather than f^3. Variations of this idea utilizing a simpler global rotation rather than translation of posts are still under study, as are details of the antenna to couple power from the resonator to the amplifier.

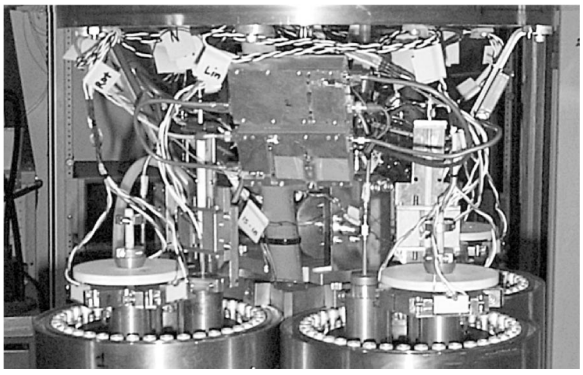

FIG. 19. Photograph of the four-cavity array used in the U.S. large-scale experiment. From Kinion, 2001.

V. TOWARD A DEFINITIVE EXPERIMENT: GENERALIZED AMPLIFIERS AND QUANTUM NOISE

At this point in the review, we begin to look at promising technologies and techniques that could support "third-generation" axion experiments—those that would cover the remaining parameter space in coupling and mass. As the axion-photon coupling $g_{a\gamma\gamma}$ is a narrow band, around a decade wide, as a function of mass, a definitive experiment is possible if the system noise temperature can be reduced sufficiently. Before presenting two promising avenues—SQUID amplifiers and the

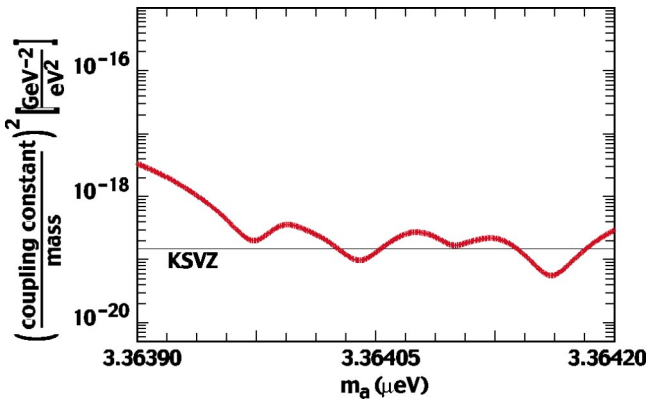

FIG. 20. (Color in online edition) Exclusion curve from the four-cavity array; a local halo density of 450 MeV/cm^3 was assumed. From Kinion, 2001.

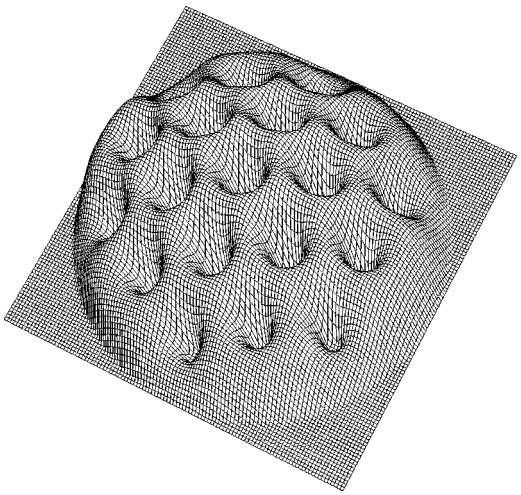

FIG. 21. Electric-field profile of the TM_{010} mode for a 19-post cylindrical cavity.

Rydberg-atom single-quantum detector—we offer a brief, general discussion of amplifiers and noise and the limitations of realizable devices.

It is widely appreciated that quantum mechanics forbids simultaneous measurement of certain pairs of ("conjugate") observables to arbitrarily high precision. Well-known examples of these pairs are position and momentum, and energy and time. Perhaps less well known is the existence of an uncertainty relation between the measurement precision of the number of quanta n in an electromagnetic wave and the phase of the radiation ϕ (Heitler, 1954),

$$\Delta n \cdot \Delta \phi \geq 1.$$

This number-phase uncertainty relation was mainly of academic interest until the development of ultralow-noise maser amplifiers in the 1960s. Until then, typical systems contained such huge numbers of quanta, with each quantum carrying such a tiny amount of momentum relative to the receiving apparatus that a classical description of the amplification process was entirely adequate. For instance, typical photon fluxes 100 km distant from even a modest-power FM radio transmitter are in the neighborhood of 10^{16} photons/m^2/sec. In this case, the underlying quantum nature of the radiation is swamped by the large flux of soft photons.

Quantum mechanics has two distinct processes—induced and spontaneous transitions—that describe electromagnetic transitions between quantum levels. In order to appreciate how these processes apply to amplification, let us consider the operating principle of the maser.

A maser contains atoms of some medium with at least two energy levels $E_1 < E_2$. The number of atoms in these levels are n_1 and n_2, with $n_1 + n_2$ the total number of available atoms. When we apply, from an external source, electromagnetic radiation at the transition frequency $(E_2 - E_1)/h$, the number of stimulated jumps is given by the stimulated transition probability, which is the same for upward and downward transitions. Since the populations n_1 and n_2 in the two levels are in general different, the power absorption by the maser material is nonzero and proportional to the population difference $n_1 - n_2$. If the energy-level populations are in thermal equilibrium, then $n_1 > n_2$ and the maser material absorbs the external radiation. However, if the energy-level populations are inverted so that $n_2 > n_1$, then there will be an excess of stimulated downward transitions with net amplification of the external source. This stimulated emission is the principle of maser amplification (Siegman, 1964).

Even in the absence of external electromagnetic radiation at the maser input, photons appear at the output. This is because, in addition to stimulated transitions, there are spontaneous transitions that occur in the absence of the external input even at zero temperature (Schiff, 1968). The rate of this spontaneous emission is easily calculable for this system and represents an irreducible minimum to the noise of this type of device. In detail, this rate of spontaneous transitions is just equal to the rate of stimulated emission that would be caused by a fictitious input signal with a strength of one quantum per mode (Siegman, 1961).

This latter observation allows a generalization to other types of amplifiers where it would be difficult to identify the energy-level structure responsible for the amplification and thereby compute the spontaneous transition rate. The generalization is that the quantum zero-point energy that populates the mode in the absence of any other electromagnetic input in the amplifier system is itself a source of photons for stimulated transitions, with the caveat that these zero-point photons only cause transitions downward. The 1 from the $n+1$ factor in the stimulated transition probability leads therefore to the concept, applicable to any amplifier, of a quantum noise level of one quantum per mode.

The uncertainty relation $\Delta n \cdot \Delta \phi \geq 1$ applies to the product. Nothing forbids measurement of one observable of the pair to high precision at the expense of the other, as long as the product uncertainty is respected. This is similar to the exercise of assembling a free-particle one-dimensional wave packet from momentum eigenstates. Obviously, momentum-space eigenstates have zero uncertainty in momentum and infinite position uncertainty. However, a wave packet assembled with an appropriate Gaussian weighting minimizes the uncertainty relation $\Delta x \cdot \Delta p \geq \hbar/2$. Further, with an appropriate normalization, this minimum occurs where the uncertainties in the product factors are equal to each other. In other words, given the state of the system, one can calculate the conjugate uncertainties, and the uncertainty relation is minimized for certain states in which both uncertainty terms are equal.

The states we speak of are those resulting from the interaction of the electromagnetic wave and the amplifier. There is a rich set of results concerning the nature of these states and the photon-detector interactions responsible for populating these states (Glauber, 1965; Kroll, 1965). One important result is that when a quantum object (the photon) interacts with a classical object

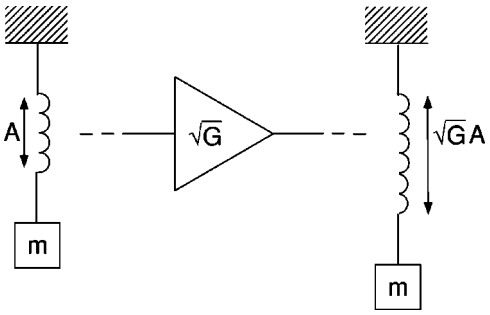

FIG. 22. The generalized amplifier system. The input system is a mode of a harmonic oscillator. The amplifier "looks" at the input and produces a harmonic oscillator at the output with amplitude gain $\sqrt{G}$.

(e.g., an antenna), the resulting states are special. These special states are given the name "coherent states," and they have the property that, in terms of their conjugate variable uncertainty relations, they are as "close to classical" as can be achieved by quantum-mechanical states. In particular, the uncertainty relation has equal contributions from the appropriately normalized product factors. These coherent states are generally unfamiliar due to certain unpleasant properties—for instance, they do not form a set of complete states. Nonetheless, this coherent-state formalism describes what happens inside a radio receiver or laser amplifier even in the limit of few or no photons at the input.

However, if the interaction of the input photons with the amplifier is nonclassical—for instance, photoelectric ejection off a cathode—the resulting states may not be simply describable as one of the pure coherent states. Such states are sometimes called "squeezed states," and though conjugate variable pairs obey the uncertainty relation, there is no guarantee of equal contributions from the product factors.

We can illustrate the above formalism with an example. Figure 22 shows one important type of amplifier system. The input is a mode of a harmonic oscillator (say, mechanical or electromagnetic). The oscillator is "viewed" by an amplifier having amplitude gain $\sqrt{G}$, so that the output of the amplifier is a harmonic oscillator in the same mode. For definiteness, we choose the oscillator equation of motion (in a mechanical realization) as $x(t)=x_c\cos\omega t+x_s\sin\omega t$ at the input and $x'(t)=\sqrt{G}x_c\cos\omega t+\sqrt{G}x_s\sin\omega t$ at the output. The constants x_c and x_s (and their associated uncertainties Δx_c and Δx_s) are called the quadrature amplitudes (uncertainties). If we suppose that the amplifier is classical in nature (containing a radio antenna, for instance), then the quadrature uncertainties are equal (as is the case for the classical coherent states) and the uncertainty relations at the amplifier input and output are $\Delta x\Delta p=m\omega(\Delta x)^2$ and $\Delta x'\Delta p'=Gm\omega(\Delta x)^2$, where $\Delta x_c=\Delta x_s=\Delta x$.

Suppose we perform a quantum-limited measurement at the amplifier output. The best we can do is $\Delta x'\Delta p'=\hbar/2$, so apparently $\hbar/2=Gm\omega(\Delta x)^2=G\Delta x\Delta p$. We therefore have the result $\Delta x\Delta p=(1/G)\hbar/2$. For any amplifier of this sort with greater than unity gain, there is an apparent violation of the uncertainty relation. Namely, one could perform a legitimate quantum-limited measurement at the amplifier output and infer a better than quantum-limited measurement of the oscillator mode at the amplifier input.

To prevent this violation of the uncertainty relation, there must be some extra noise δ_n that, referenced to the amplifier input, contributes as $\Delta x\Delta p=(1/G)\hbar/2+m\omega\delta_n^2$. We do not specifically assign this extra noise to the amplifier or the input oscillator. Now, a quantum-limited measurement, referenced to the amplifier input, obeys the uncertainty relation $\Delta x\Delta p=\hbar/2$ provided $m\omega\delta_n^2=(1-1/G)\hbar/2$, where δ_n is the noise referenced to the amplifier input. The quadrature amplitudes are therefore uncertain by δ_n. That is, the input oscillator equation of motion inferred by the measurement at the amplifier output could well be

$$x(t)=(x_c+\sqrt{2}\,\delta_n)\cos\omega t+(x_s+\sqrt{2}\,\delta_n)\sin\omega t.$$

Now suppose, in reality, the input oscillator (viewed classically) equation of motion obeyed $x_c=x_s=0$; then the inferred equation of motion might be

$$x(t)=\sqrt{2}\,\delta_n\cos\omega t+\sqrt{2}\,\delta_n\sin\omega t.$$

The apparent energy of this oscillator is $[(m\omega x_0)^2+p^2]/2m$, or $(1-1/G)\hbar\omega$. As discussed above, this result can be interpreted as due to the uncertainty relationship or to transitions induced by the zero-point energy, but the important result is that this amplifier appears to have excess noise of one photon in each mode. This is sometimes referred to as the "standard quantum limit" (Braginsky and Khalili, 1992). Expressed in noise temperature T_n this is

$$T_n=\hbar\omega/k_B,$$

where k_B is Boltzmann's constant. For amplification of a 1-GHz electromagnetic wave, this quantum noise temperature T_n is approximately 50 mK.

The standard quantum limit applies to a broad class of amplifiers. In particular, the HFET and SQUID amplifiers used in the U.S. Axion Search described in this review are bound by this limit. At present, the HFET amplifiers are not yet low enough in noise that this quantum limit is dominant, but the SQUID amplifiers may well be approaching this limit (see Sec. VI).

When the conditions leading to the standard quantum limit are relaxed, particularly the requirement that the amplifier behave near classically, then the contribution by the two factors in the number-phase uncertainty relation need no longer be equal. One extreme is the photon counter. Here, the uncertainty in the number of photons is small, but the uncertainty in the photon phase is large. Familiar realizations of this are the photomultiplier tube, photographic film, and the avalanche photodiode. A less familiar realization is the microwave photon counter based on Rydberg states of alkali atoms. This technique of single microwave photon counting was first demonstrated by Kleppner and Ducas (1976) and is the basis of the Kyoto axion search (see Sec. VII). This latter technique is attractive in that there is no funda-

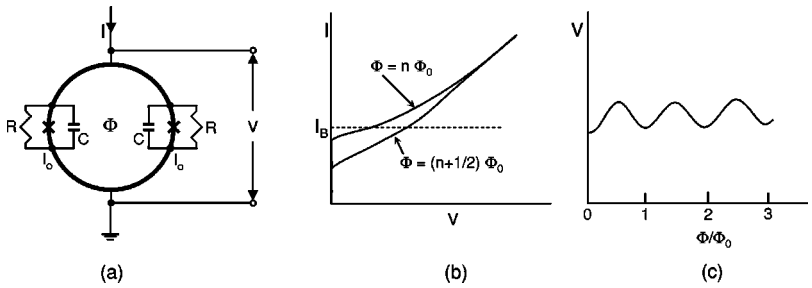

FIG. 23. Essence of the dc SQUID. (a) Representation in the resistively-shunted-junction (RSJ) circuit model showing the two Josephson junctions in a superconducting loop. (b) Current-voltage (I-V) characteristics for two different values of magnetic flux through the SQUID. (c) SQUID voltage V vs magnetic flux Φ/Φ_0 at constant bias current.

mental limit to the sensitivity of the Rydberg photon detector, but of course these amplifiers are not suitable for interferometric studies.

There are a considerable number of alternative amplifier technologies; some are obsolete and some are promising but not thoroughly explored, or both. These include diode mixers of all types (tunnel, Schottky, etc.), tunnel diode amplifiers, parametric amplifiers, masers, superconductor-insulator-superconductor (SIS) mixers, SQUID's, single-electron transistors, and HFET amplifiers of all types (GaAs, InP, etc.). The interested reader is referred to the literature (Okwit, 1984; Pospieszalski, 1993).

We now turn our attention to the specific technologies that we believe hold the most immediate promise for future microwave cavity experiments. Section VI is devoted to near-quantum-limited gigahertz SQUID amplifiers developed for the next-generation U.S. experiment. Section VII presents a theoretical description of Rydberg-atom single-quantum detection and its planned implementation in a large-scale experiment.

VI. THE MICROSTRIP SQUID AMPLIFIER

This section outlines the principles, operation, and performance of the microstrip SQUID amplifier. We begin with a summary of the principles of the dc SQUID and its practical realization and then briefly discuss the principle of microstrip input coupling. Subsequently we describe a realization of the microstrip SQUID amplifier and report measurements of the gain and frequency response. The last part of the section presents measured values of noise temperature at both liquid-^{4}He and millikelvin bath temperatures; we end with a brief summary.

A. The dc SQUID

1. Principles

The essence of the dc SQUID (Jaklevic *et al.*, 1964) is shown in Fig. 23. Two Josephson junctions (Josephson, 1962) are connected in parallel on a superconducting loop of inductance L. Each junction has parallel self-capacitance C and a resistance R, which is usually an external shunt. According to the resistively-shunted-junction model (McCumber, 1968; Stewart, 1968), the current-voltage (I-V) characteristics are nonhyster etic provided $\beta_c \equiv 2\pi I_0 R^2 C/\Phi_0 \leqslant 1$, where I_0 is the critical current of each junction and $\Phi_0 \equiv h/2e \approx 2.07 \times 10^{-15}$ Wb is the flux quantum. The I-V characteristics are shown in Fig. 23(b) for $\Phi = n\Phi_0$ and $(n+1/2)\Phi_0$, where Φ is the external flux applied to the loop and n is an integer. When the SQUID is biased with a constant current $I_B > 2I_0$, the voltage across the SQUID oscillates with period Φ_0 as Φ is steadily increased, as indicated in Fig. 23(c). The bias current is adjusted to give the maximum voltage change, and the SQUID is operated on the steepest part of the V-Φ curve where the flux-to-voltage transfer coefficient, $V_\Phi \equiv |(\partial V/\partial \Phi)_{I_B}|$, is a maximum. Thus the SQUID produces an output voltage in response to a small input flux $\delta\Phi (\ll \Phi_0)$ and is effectively a flux-to-voltage transducer.

To calculate the signal and noise properties of the SQUID one must solve numerically the equations relating the voltage across the SQUID to the bias current and the applied flux (Tesche and Clarke, 1977; Likharev, 1986; Ryhänen *et al.*, 1989; Koelle *et al.*, 1999). The noise arises from Nyquist current noise in the shunt resistors, which has a spectral density $4k_B T/R$. One finds that V_Φ peaks smoothly as a function of bias current and has a shallow maximum around an applied flux of $(2n+1)\Phi_0/4$. By using the computer to explore the behavior of the SQUID over a wide range of parameters one finds the conditions for optimal performance. Noise plays a key role in determining these conditions, and enters in two ways. First, the Josephson coupling energy of each junction, $I_0\Phi_0/2\pi$, must be substantially greater than the thermal energy, $k_B T$. This constraint is written in terms of a dimensionless noise parameter as

$$\Gamma \equiv 2\pi k_B T/I_0\Phi_0 = I_{\rm th}/I_0 \ll 1, \tag{21}$$

where $I_{\rm th} = 2\pi k_B T/\Phi_0 \approx 0.18\ \mu$A at 4.2 K. Second, the magnetic energy per flux quantum, $\Phi_0^2/2L$, must also be substantially greater than $k_B T$. We can express this requirement as (Koelle *et al.*, 1999)

$$\Gamma\beta_L \equiv 4\pi L k_B T/\Phi_0^2 = L/L_{\rm th} \ll 1, \tag{22}$$

where $\beta_L \equiv 2LI_0/\Phi_0$. The thermal inductance $L_{th} \equiv \Phi_0^2/4\pi k_B T$ is 5.9 nH at 4.2 K. The simulations show that optimum performance is achieved for $\beta_L \approx 1$ and that the noise level increases rapidly for $\Gamma\beta_L > 0.15$. From Eq. (22) we see that this constraint places an upper limit on L of about 900 pH at 4.2 K.

The computed values of the response and noise will, of course, depend on the chosen parameters, but for a typical SQUID at 4.2 K with $\beta_L = 1$ and $\Gamma = 0.05$ one finds the transfer function $V_\Phi \approx R/L$ under optimum bias conditions. The corresponding white voltage noise across the SQUID has a spectral density $S_V(f)$

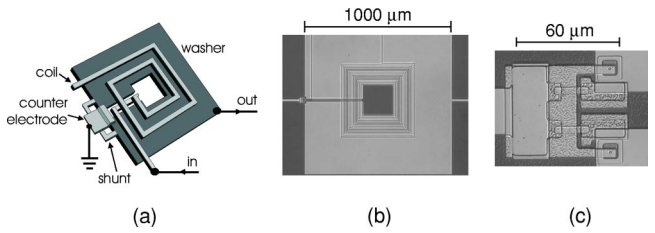

FIG. 24. (Color in online edition) The dc SQUID configured as a microwave amplifier: (a) Schematic drawing of square washer SQUID, with integrated spiral coil electrically insulated from it. (b) Photograph of square washer SQUID with 15-turn input coil. The two Josephson junctions are on the left side of the washer, as shown on an expanded scale in (c). Here, the two small dots are the junctions, consisting of an Al_2O_3 oxide layer sandwiched between the Nb washer below and Nb counter electrode above. The normal metal shunt resistors are visible as two horizontal strips above and below the middle of (c).

$S_V(f)S_V(f)\approx 16k_BTR$, approximately eight times the Nyquist noise in a resistance $R/2$. The spectral density of the equivalent flux noise is thus

$$S_\Phi(f)=S_V(f)/V_\Phi^2\approx 16k_BTL^2/R. \tag{23}$$

A useful figure of merit is the flux noise energy,

$$\varepsilon(f)=S_\Phi(f)/2L\approx 9k_BTL/R, \tag{24}$$

which takes into account the SQUID inductance.

For a representative SQUID at 4.2 K with $L=100$ pH, $I_0=10\ \mu$A, and $R=4\,\Omega$, one finds $V_\Phi\approx 80\ \mu\mathrm{V}\Phi_0^{-1}$ and $\epsilon(f)\approx 1.3\times 10^{-32}\ \mathrm{J\,Hz^{-1}}\approx 125\hbar$. The performances of dc SQUID's are generally in good agreement with predictions over a wide range of parameter space.

In addition to the voltage noise across the SQUID, there is also a current noise $J_N(t)$ around the SQUID loop (Tesche and Clarke, 1979), which has a spectral density

$$S_J(f)\approx 11k_BT/R. \tag{25}$$

Furthermore, the current noise is partially correlated with the voltage noise across the SQUID, with a cross-spectral density

$$S_{VJ}(f)\approx 12k_BT. \tag{26}$$

This correlation arises because the current noise generates a flux noise, which, in turn, contributes to the total voltage noise across the junction.

2. Practical dc SQUID's

The most commonly used SQUID's are made from photolithographically patterned thin films of Nb, following the design of Ketchen and Jaycox (1982), who deposited a superconducting spiral coil of n turns over the square washer that forms the body of the SQUID. A typical example is shown in Fig. 24. The coil is separated from the SQUID with an insulating layer and may be coupled to one of several different circuits, depending on the application. Design guidelines were given by Jaycox and Ketchen (1981), who showed that a square washer (with no slit), with inner and outer edges d and w, has an inductance $L(\mathrm{loop})=1.25\mu_0 d$ in the limit $w\gg d$. Here, $\mu_0=4\pi\times 10^{-7}$ H/m is the permeability of free space. They gave the following approximate expressions for the inductances of the SQUID, L, and the spiral coil, L_i, and for their mutual inductance M_i, in the limit of reasonably large n (say, greater than 20):

$$L=L(\mathrm{loop}), \tag{27}$$

$$L_i=n^2L, \tag{28}$$

and

$$M_i=nL. \tag{29}$$

Measured parameters are generally in good agreement with these predictions. Cantor (1996) has given a useful overview of SQUID design issues.

SQUID's are usually fabricated on 2–4-in. Si wafers and incorporate trilayer Nb/Al-Al_2O_3/Nb junctions (Gurvitch *et al.*, 1983). The SQUID washer and coil are patterned in Nb films, separated by an insulating layer of SiO_2. The shunt resistors are typically of Pd. For the device shown in Fig. 24, the estimated SQUID inductance is $L=0.32$ nH, and the measured shunt resistance $R=12\,\Omega$.

In virtually all applications at frequencies up to a few megahertz, the SQUID is used in a flux-locked loop as a null detector of magnetic flux. Thus, if one applies a flux $\delta\Phi$ to the SQUID, the feedback loop generates a canceling flux $-\delta\Phi$ in the SQUID and an output voltage proportional to $\delta\Phi$. Typical SQUID's have a noise of $(1-2)\times 10^{-6}\Phi_0\ \mathrm{Hz^{-1/2}}$ at frequencies down to about 1 Hz. Drung (1996) gives a detailed discussion of the issues concerning dynamic range, bandwidth, and slew rate.

At higher frequencies, the SQUID is operated open loop, with a static flux bias near $(2n+1)\Phi_0/4$. Hilbert and Clarke (1985) fabricated radio-frequency amplifiers with a tuned input circuit formed by connecting the SQUID input coil in series with a capacitor and a voltage source. Using standard methods for calculating noise temperature, it is straightforward to show that on resonance at frequency f the optimized value is given by

$$T_N(\omega)\approx\frac{\pi f}{k_BV_\Phi}(S_VS_J)^{1/2}\approx\frac{42fT}{V_\Phi}. \tag{30}$$

For an amplifier with $R\approx 8\,\Omega$, $L\approx 0.4$ nH, $L_i\approx 5.6$ nH, $M_i\approx 1$ nH, and $V_\Phi\approx 3\times 10^{10}\ \mathrm{sec^{-1}}$ at 4.2 K, Hilbert and Clarke found a power gain $G=18.6\pm 0.5$ dB and $T_N=1.7\pm 0.5$ K at 93 MHz. The predicted values were 17 dB and 1.1 K, respectively.

As the frequency was increased above about 200 MHz, the gain decreased rapidly because of the shunting effect of the parasitic capacitance between the coil and the SQUID washer. It is this problem that prevents one from operating a conventional dc SQUID in the gigahertz frequency range.

B. The microstrip SQUID amplifier

1. The microstrip

The microstrip SQUID amplifier makes a virtue of the capacitance between the coil and the washer by us-

ing it to form a resonant line. A microstrip consists of a superconducting strip of width w separated from an infinite superconducting sheet by an insulator with dielectric constant ε and thickness d. We assume that the thicknesses of the two superconductors are much greater than the superconducting penetration depth λ, and that $w \gg d$. The capacitance and inductance per unit length of the microstrip are given by (Ramo *et al.*, 1965) $C_0 = \varepsilon\varepsilon_0 w/d$ (F/m) and $L_0 = (\mu_0 d/w)(1+2\lambda/d)$ (H/m). Here, $\varepsilon_0 = 8.85\times10^{-12}$ F/m and $\mu_0 = 4\pi\times10^{-7}$ H/m are the permittivity and permeability of free space, and $c = 1/(\varepsilon_0\mu_0)^{1/2} = 3\times10^8$ m/sec is the velocity of light in vacuum. The factor $(1+2\lambda/d)$ accounts for the penetration of the magnetic field into the (identical) superconductors. The velocity of an electromagnetic wave on the microstrip is thus given by $\overline{c} = c/[\varepsilon(1+2\lambda/d)]^{1/2}$, and its characteristic impedance by

$$Z_0 = \left(\frac{L}{C}\right)^{1/2} = \frac{d}{w}\left[\frac{\mu_0(1+2\lambda/d)}{\varepsilon\varepsilon_0}\right]^{1/2}. \tag{31}$$

The microstrip can be configured as an electromagnetic resonator. For a microstrip of length ℓ with its two ends either open or terminated with resistances greater than Z_0, the fundamental frequency occurs when ℓ is equal to a half-wavelength (Ramo *et al.*, 1965),

$$f_0(L_0) = c/2\ell[\varepsilon(1+2\lambda/d)]^{1/2}. \tag{32}$$

In this mode, the resonator is analogous to a parallel tuned circuit, and for a resistance $R_i > Z_0$ connected to one end, the quality factor of the resonance is given by $Q = \pi R_i/2Z_0$.

2. Gain and frequency response

The microstrip SQUID has the conventional square-washer configuration (Fig. 24). However, in contrast to the conventional input scheme in which the signal is connected to the two ends of the coil, the signal is instead coupled between one end of the coil and the square washer; the end of the coil is left open. In this configuration, the coil forms the strip conductor of a microstrip and the washer provides the ground plane. In an early set of experiments (Mück *et al.*, 1998), the square washer had inner and outer dimensions of 0.2×0.2 mm^2 and 1×1 mm^2, and the input coil had $n=31$ turns, a width $w=5$ μm, and a length $\ell=71$ mm. Estimated parameters were $L\approx320$ pH, $L_i\approx300$ nH, and $M_i\approx10$ nH. The critical current and shunt resistance per junction were typically 5 μA and 10 Ω, and the maximum value of V_Φ was about $60\mu V\Phi_0^{-1}$. At 4.2 K, the white flux noise measured in a flux-locked loop at low frequencies was typically $2-3\mu\Phi_0$ Hz$^{-1/2}$. We note that virtually the entire length of the coil overlays the washer, which is at a uniform potential. The SQUID chip was mounted on a printed circuit board, and each pad was wire-bonded to a 50-Ω trace patterned on the board. The grounds of the input and output sub-miniature type-A (SMA) connectors were soldered to a ground plane on the reverse side of the board, and their center conductors were soldered to the traces coupled to the input of the microstrip and to the output from the SQUID, respectively. The assembly was rigidly mounted inside a box (made of lead foil) that eliminated fluctuations in the ambient magnetic field. Most measurements were made with the package immersed in liquid ^{4}He.

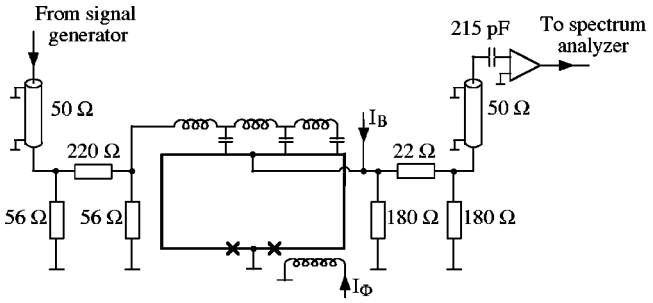

FIG. 25. Circuit used to determine the gain of a microstrip SQUID, which is shown with counter electrode grounded. I_B is the current bias, and I_Φ provides the flux bias. The input and output π networks have attenuations of 20 and 5 dB, respectively. The input microstrip is shown as a lumped-element line. From Mück *et al.*, 1998.

The circuit shown in Fig. 25 was used to measure the gain; the input coil over the square washer is shown as a distributed line. The current bias was supplied by batteries. The flux bias was provided by a directly coupled flux-locked loop that maintained the SQUID near its maximum gain (Mück and Clarke, 2001a). The loop rolled off at frequencies above a few kilohertz and had no effect on the high-frequency performance. A sweep oscillator was coupled to the microstrip via a room-temperature 100-dB attenuator and a cold 20-dB attenuator that prevented noise produced by the generator from saturating the SQUID. The cold attenuator also presented an impedance of 50 Ω to both the input coaxial line and the microstrip. A second cold, 4-dB attenuator coupled the output of the SQUID to a room-temperature postamplifier. The gain of the system excluding the SQUID was calibrated by disconnecting the SQUID and connecting the input and output attenuators. All measurements of the gain of the SQUID amplifier were referred to the baseline so obtained.

Since the washer SQUID is an asymmetric device—the two Josephson junctions are situated close together rather than on opposite sides of the SQUID loop—one can either ground the washer, on which the oxide barriers of the Josephson junctions are grown, or ground the upper Nb film (counter electrode) that completes and connects the two junctions. Since the washer acts as a ground plane for the input coil, at first sight it might seem plausible to ground the washer. However, it is also possible to ground the counter electrode and have the washer at output potential. In the latter case, one can have feedback from the output voltage generated on the washer to the input coil, via the capacitance between them. If the sign of V_Φ is such that the output voltage has the same sign as the input voltage, the feedback is positive; if the signs are opposite, the feedback is negative. We designate the corresponding flux-to-voltage transfer coefficients as V_Φ^+ and V_Φ^-, respectively.

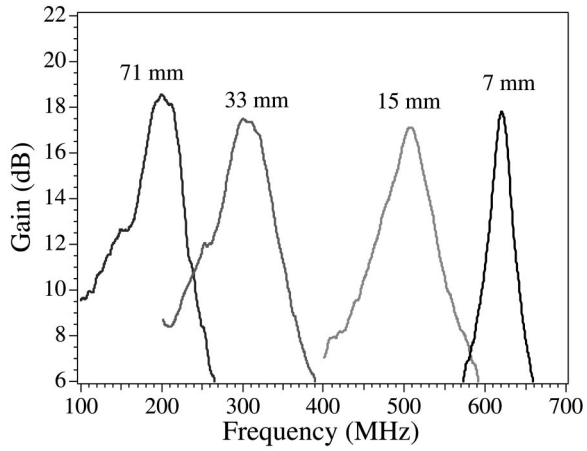

FIG. 26. Gain vs frequency for four coils on the same SQUID, with signal applied to the innermost turn. Data are for counter electrode grounded and V_Φ^+. Adapted from Mück *et al.*, 1998.

Figure 26 shows the gain of amplifier versus frequency for a device, initially with 31 turns, in which the number of turns was progressively reduced to 19, 11, and 6 using photolithography and reactive ion etching. As expected, the peak in the gain shifts to progressively higher frequencies as the length of the microstrip is reduced, from 200 MHz for the 71-mm coil to 620 MHz for the 7-mm coil. In addition, Q increases as the coil is shortened. However, the measured peak frequencies are not at all well predicted by the microstrip formulas given in the previous section. Taking the values $w=5\,\mu$m, $d=0.4\,\mu$m, $\varepsilon=9$, and $\lambda=0.15\,\mu$m, we find $C_0\approx 1$ nF m^{-1} and $L_0\approx 200$ nH m^{-1}. Thus $\overline{c}\approx 0.25c$, and for $\ell=31$ mm, Eq. (32) yields a resonant frequency of about 500 MHz, roughly $2\frac{1}{2}$ times the observed value. The discrepancy becomes even larger at shorter coil lengths.

A much better agreement between measured and predicted peak frequencies is obtained by taking n^2L/ℓ as the inductance per unit length, instead of L_0. This assumption leads to the predicted resonant frequency (Mück and Clarke, 2000)

$$f_0(n^2L)=1/2n(\ell L C_0)^{1/2}. \tag{33}$$

Table I compares the resonant frequencies for five SQUID's with those predicted by the microstrip model [Eq. (32)] and by Eq. (33). The resonant frequencies were measured using a reverse gain technique that eliminates the shift in the resonance by positive or negative feedback. We see that the latter values are much closer to the measured values than those of the microstrip model. We note, however, that the discrepancy between the measured values and those predicted by Eq. (33) increases as the coil is shortened. This trend may be explained by the fact that the parasitic inductance of the wiring to the chip becomes progressively more important as the length of the coil is shortened.

As the coil length is shortened further, the peak frequency continues to increase. A gain of about 21 dB has been realized at 1.6 GHz. In a SQUID with the hole replaced by a narrow slit and a 7-turn coil, the peak frequency was 3.8 GHz. However, the gain was reduced to 10 dB, largely because of the relatively small mutual inductance between the input coil and the SQUID.

TABLE I. Measured frequency f_0 of the fundamental resonance (half-wavelength) for five microstrip SQUID's with coils of n turns and length ℓ. Current and flux biases were adjusted to give the maximum transfer coefficient. The resonant frequency $f_0^{\rm calc}(L_0)$ is calculated from Eq. (32), assuming $L_0=175$ nH/m and $C_0=0.6$ nF/m; $f_0^{\rm calc}(n^2L)$ is the resonant frequency calculated using Eq. (33).

SQUID No.	n	ℓ (mm)	f_0 (MHz)	$f_0^{\rm calc}(L_0)$ (MHz)	$f_0^{\rm calc}(n^2L)$ (MHz)
1	40	97.6	105	500	91
2	15	23.5	370	2100	500
3	11	16	590	3000	820
4	6	7.9	1200	6200	2200
5	4	3.7	2100	13000	4700

Mück and Clarke (2000) studied the electromagnetic behavior of the microstrip SQUID amplifier using both an analog model and numerical calculations. The analog model confirmed the validity of Eq. (33) for the resonant frequency. The numerical simulations, using both lumped circuit and distributed element models, were used to study the effects of positive and negative feedback, corresponding to a grounded electrode with transfer functions V_Φ^+ and V_Φ^-. These simulations agree well with the observation that the peak in the gain occurs at a frequency above and below the resonance, respectively. The same model was used to investigate the input impedance of the microstrip, which is dominated by the complex impedance of the SQUID. For V_Φ^+, the input resistance became negative below the half-wavelength resonance in the frequency range where the gain was high. Correspondingly, for V_Φ^-, the input resistance was negative above the half-wavelength resonance, where the gain was also high. For low gains (above the resonance for V_Φ^- and below the resonance for V_Φ^+), the input resistance was positive and the return loss high. These simulations followed the trends in measured values of the input impedance remarkably well.

In a further series of experiments, Mück and Clarke (2001b) investigated harmonic distortion and intermodulation distortion. They showed that, biased for maximum gain, the microstrip SQUID amplifier generates third-harmonic signals with an amplitude in good agreement with a model based on a sinusoidal flux-to-voltage transfer function. The amplitude of the third harmonic is less than 1% of the fundamental for a flux amplitude of $0.1\Phi_0$. However, under the same bias conditions, departures from a sinusoidal transfer function produce a second-harmonic signal. This signal can be reduced or even eliminated by adjusting the flux bias empirically away from the point of maximum gain. Similarly, the third- and fifth-order intermodulation products can be non-negligible with the SQUID biased for maxi-

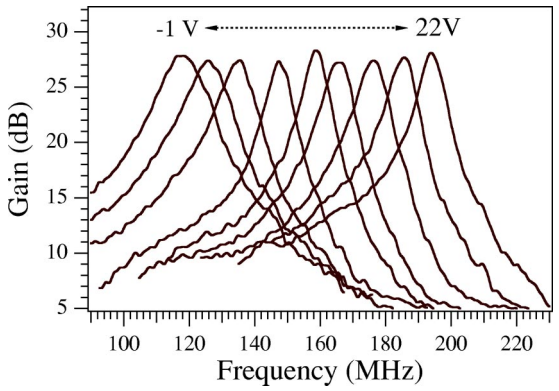

FIG. 27. Gain vs frequency for microstrip SQUID amplifier with 31 turns at 4.2 K for nine values of reverse bias voltage applied to the varactor diode. Adapted from Mück *et al.*, 1999.

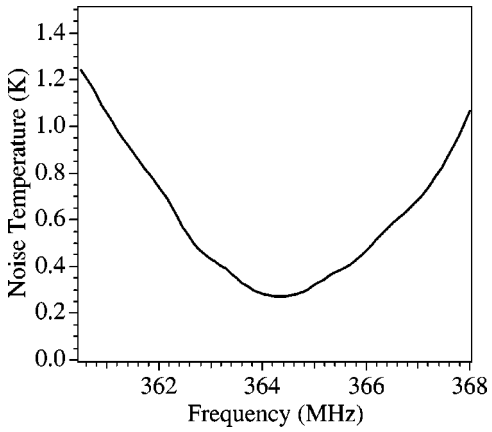

FIG. 28. Noise temperature for a microstrip SQUID amplifier with 29-turn spiral input coil. The device and its HFET postamplifier were cooled to 1.8 K. From André *et al.*, 1999.

mum gain, but one or the other can be reduced if the flux bias is adjusted appropriately.

We have seen that substantial levels of gain can be achieved with the microstrip SQUID amplifier. However, the peak frequency is clearly fixed by the length of the microstrip, whereas the axion detector demands tunability. Fortunately, one can tune the frequency quite simply by connecting a varactor diode across the otherwise open end of the input coil (Mück *et al.*, 1999). The capacitance of the diode can be varied by changing the value of the reverse bias voltage. Changing the capacitance modifies the phase shift of the electromagnetic wave when it is reflected, thereby increasing or decreasing the effective length of the microstrip and lowering or raising the peak frequency.

Experiments were carried out with a GaAs varactor diode, the capacitance of which could be varied from 1 to 10 pF by changing the bias voltage from -15 to 0 V. Two diodes in parallel were used to obtain a wider tuning range. The diodes, in series with a capacitor, were connected across the end of the input coil not connected to the signal source. The gain for optimized current and flux biases for a SQUID with 31 turns is shown in Fig. 27 for nine values of the capacitance of the two diodes. We see that the peak frequency is progressively lowered, from 195 to 117 MHz, as the capacitance is increased. The maximum gain is constant to within 1 dB over this range. In the absence of the varactor, the peak frequency is about 200 MHz. In fact, the presence of the varactors increases the gain, most likely by increasing the degree of positive feedback. The dependence of the peak frequency on the varactor capacitance is in reasonable agreement with a simple model (Mück *et al.*, 1999).

A potential concern is whether the varactor diode might introduce additional noise into the amplifier. Estimates of the contributions of the Nyquist noise and shot noise of the diode and of the noise on the bias voltage indicate that they should not be significant. The measured noise temperatures of a particular device with and without the varactor diodes were identical to within the uncertainties.

3. Noise

We turn now to the central issue, the noise temperature. An accurate way of measuring T_N is to increase the temperature T of the input load by means of a heater, so that the resistor provides a well-defined source of Nyquist noise power. The noise power at the output of the postamplifier is given by

$$P_N(f)=k_B(T+T_N)R_iGG_P+k_BT_PR_iG_P, \tag{34}$$

where G and G_P are the (power) gains of the SQUID amplifier and postamplifier, and T_P is the noise temperature of the postamplifier. By measuring the output noise power with a spectrum analyzer for several values of T, one can infer T_N+T_P/G. Measuring T_P separately using a similar method, one can deduce T_N. This discussion also makes it clear that one requires $T_P/G \ll T_N$ to ensure that the postamplifier noise does not contribute significantly to the system noise temperature.

In preliminary experiments, the postamplifier was at room temperature and had a noise temperature of about 80 K. Thus, with a typical SQUID power gain of 200 on resonance, the postamplifier contributed a noise temperature of about 0.4 K. Subsequent experiments made use of a single-stage postamplifier using a heterostructure field-effect transistor (HFET—a Fujitsu FHX13LG) operated in the ^{4}He bath. This postamplifier had a noise temperature of 10 ± 1.5 K. Figure 28 shows the system noise temperature versus frequency for a device with a peak frequency near 365 MHz, cooled to 1.8 K. The maximum gain of the microstrip SQUID was 24.5 ± 0.5 dB. The noise temperature increases rapidly as the frequency moves away from the peak; this effect is due largely to the resonant network used to couple the SQUID to the HFET. At the gain peak, the system noise temperature is 0.28 ± 0.06 K, to which the postamplifier contributes 0.09 ± 0.02 K. Thus the intrinsic noise temperature is 0.19 ± 0.06 K, an order of magnitude lower than the bath temperature. The noise temperature is also an order of magnitude lower than that of state-of-the-art, cooled semiconductor amplifiers (Bradley, 1999).

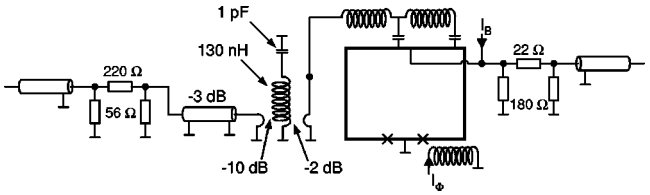

FIG. 29. Configuration of circuit used to detect Nyquist noise in a resonant circuit inductively coupled to the input of the microstrip amplifier. From André *et al.*, 1999.

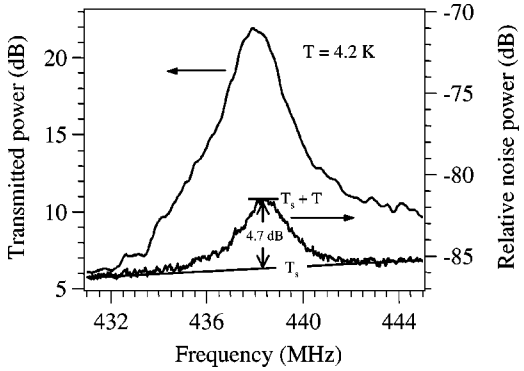

FIG. 30. Gain and noise of microstrip SQUID amplifier coupled to the resonant circuit of Fig. 29. The two curves show the transmitted power (referred to loop that couples signal into resonant circuit) at 4.2 K, and noise power with no input signal. Adapted from André *et al.*, 1999.

An alternative way to determine T_N is to couple the input of the microstrip to a tuned circuit, as shown in Fig. 29 (André *et al.*, 1999). The LC circuit consisted of a 1-pF capacitor and a four-turn copper coil, about 4 mm in diameter, inductively coupled to the microstrip by means of a loop of wire. In a separate experiment, the loop was connected to a 50-Ω cable, and the distance between the coil and the loop was adjusted to produce a 2-dB loss, thus reducing the Q by a factor of about 2. To determine the gain and Q, a second loop, with a coupling loss of 10 dB to the tuned circuit, was connected to a signal generator via a cold 20-dB attenuator and a stainless-steel cable with a loss of 3 dB.

The measured transmitted power at 4.2 K is shown in Fig. 30 (upper trace). The Q is about 270 and the maximum gain is 22 dB. The gain is referred to the input coupling loop of the resonant circuit and includes an added 12 dB to account for the coupling losses.

The noise generated by the resonant circuit, with the generator disconnected, is shown in the lower trace of Fig. 30. The measured peak is 4.7 dB above the (nearly white) noise background; to refer the peak to the input of the microstrip, 2 dB must be added to account for the coupling losses to obtain a peak height of 6.7 dB. This peak contains contributions from the Nyquist noise of the resonant circuit and from the system noise of the SQUID amplifier. Although it is not entirely straightforward to separate these contributions, using the following approximate argument one can show that this result is consistent with the measured noise temperature. On resonance, since the microstrip reduces the Q of the resonant circuit to approximately 1/2 of its unloaded value, the source impedance presented to the microstrip is roughly equal to the characteristic impedance of the microstrip. At frequencies well below resonance, the magnitude of the source impedance is approximately ωL_ℓ, where L_ℓ is the inductance of the coupling loop. Estimating $L_\ell \sim 10$ nH, we find $\omega L_\ell \sim 25\,\Omega$ at 400 MHz. Since $T_N \ll T$, to a first approximation one can ignore any variation in the noise power with source impedance. Thus the total noise on resonance can be characterized as a temperature $(T+T_N+T_P/G')$, while off resonance the corresponding value is (T_N+T_P/G'). Here, G' is the gain of the microstrip amplifier reduced by the 4-dB loss in the attenuator coupling it to the HFET. Using the peak height of 6.7 dB, we find T_N from the relation $10\log[(T+T_N+T_P/G')/(T_N+T_P/G')] \approx 6.7$ or $(T_N+T_P/G') = T_S \approx 1.1$ K. Given the approximations involved, this result is in reasonable agreement with the measured system noise temperature, 1.4 ± 0.18 K. It is clear that the predominant contribution to the noise peak in Fig. 30 is Nyquist noise in the resonant circuit.

It is evident from Eq. (30) that one expects T_N to scale with the bath temperature. Thus one might hope that even lower noise temperatures would be possible with the device cooled to millikelvin temperatures in a dilution refrigerator. However, the contribution of the HFET amplifier, about 0.1 K, would then become dominant. To circumvent this problem, a second microstrip SQUID amplifier was used as a postamplifier, as shown in Fig. 31 (Mück *et al.*, 1999). The resonant frequency of the second SQUID was tuned with a varactor diode to be near that of the first. To prevent the two SQUID's from interacting with each other, it was necessary to separate them with an attenuating network. Figure 32 shows the combined gain versus frequency for a particular pair of SQUID's at 4.2 K; the maximum gain is 33.5 ± 1 dB.

Figure 31 shows the system that was cooled in a dilution refrigerator (Mück *et al.*, 2001). All leads connected directly to the SQUID's were very heavily filtered over a wide frequency range using a combination of lumped circuit and copper powder filters, and a superconducting shield surrounding the SQUID's eliminated ambient magnetic-field fluctuations. The overall gain of the two SQUID's at 538 MHz was 30 ± 1 dB and 32 ± 1 dB at 4.2 K and 100 mK, respectively. A third stage of amplification was provided by an HFET (Fujitsu FHX13LG) with a resonant input circuit, cooled to 4.2 K and connected to the SQUID postamplifier via a cryogenic cable with a loss of 6 dB. At 550 MHz, the gain of the HFET was 22 ± 1 dB, and its noise temperature T_P about 6 K. At the lowest temperatures, the cable loss reduced the effective gain G' of the two SQUID's to 26 ± 1 dB so that the HFET contributed a noise temperature $T_P/G' \approx 15$ mK referred to the input of the first SQUID. Two different input circuits were used to measure the noise: the lower involved measuring the signal-to-noise ratio in the presence of an accurately known signal, and the upper involved measuring the noise from a resonant cir-

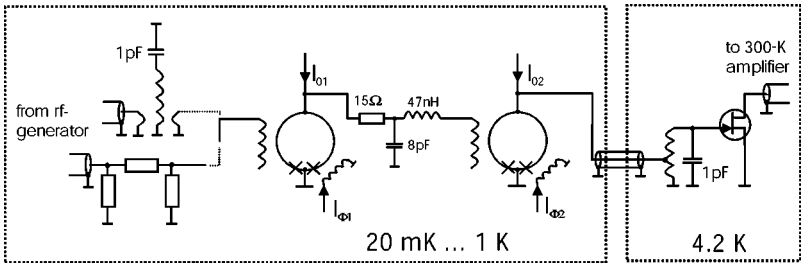

FIG. 31. Schematic of cascaded microstrip SQUID's and HFET. The input circuit on the left consists of either a resistive network (lower) or a resonant circuit (upper). From Mück, Kycia, and Clarke, 2001.

cuit. The two methods gave nearly identical results, and we describe only the second.

During the measurement, a small (about -140 dBm) signal was applied to the LC circuit, via the coupling loop, at a frequency about 2 MHz above its 519-MHz resonant frequency. This signal was used to optimize the bias currents and fluxes of the two SQUID's for maximum gain and optimum signal-to-noise ratio. The peak was monitored throughout the measurements to verify that the gain did not drift. The inset in Fig. 33 shows this peak, together with the noise peak from the resonant circuit. The value of T_N is extracted from the peak using the method described above, with the Nyquist noise power replaced by $(hf/2k_B)\coth(hf/2k_BT)$. Figure 33 shows the inferred values of T_N versus T. The error bars are determined solely by the uncertainty in the spectrum analyzer measurement. We see that T_N scales as T above about 150 mK, and flattens off at temperatures below about 70 mK to 47 ± 10 mK; by comparison, $T_Q \approx 25$ mK.

A potential source of the low-temperature saturation of T_N is hot electrons produced in the resistive shunts by bias current heating. Wellstood *et al.* (1994) obtained remarkably similar results for the noise spectral density measured at frequencies below about 50 kHz in SQUID's cooled to around 20 mK and found good agreement with a model in which the temperature of the electrons is determined by their coupling to the phonons. To investigate whether hot electrons were indeed responsible for the saturation in Fig. 33, Mück *et al.* (2001) remeasured the noise of the same SQUID at 140 kHz, where $T_Q < 10$ μK. For this experiment, the output of the first SQUID was coupled to the two ends of the input coil of a second SQUID, via a superconducting transformer with a current gain of about 3. The output of the second SQUID was coupled to a room-temperature amplifier with a noise temperature of about 3 K. The temperature dependence of the noise energy data at 140 kHz mimicked the noise temperature data plotted in Fig. 33 quite remarkably, leveling off to 1.2 ± 0.2 h at low temperatures. Since the data flatten out at the same temperature for both frequencies, the saturation in Fig. 33 cannot represent the quantum limit. Rather, since saturation occurs at about the same temperature as that in the experiments of Wellstood *et al.*, it is most likely due to the generation of hot electrons in the shunt resistors.

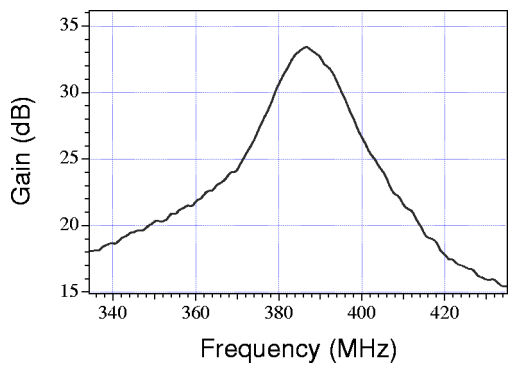

FIG. 32. Measured gain of two cascaded microstrip SQUID amplifiers. From Mück *et al.*, 1999.

C. Summary

We have described a new configuration of the dc SQUID in which the input signal is coupled between one end of the input coil and the square washer that forms the body of the SQUID. At the peak of the gain, the magnetic field couples strongly to the SQUID, enabling one to achieve a power gain of 20–25 dB over frequencies ranging from 0.2 to 1.6 GHz. The frequency at which the peak occurs can be tuned over a factor of nearly 2 by means of a pair of varactor diodes connected across the open end of the microstrip. The noise temperature T_N scales with the bath temperature T down to temperatures of about 100 mK, at which hot electrons

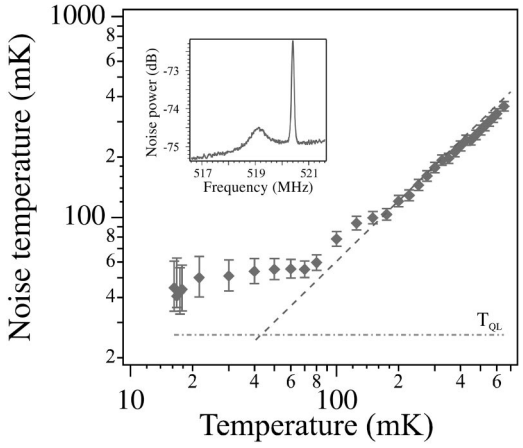

FIG. 33. Noise temperature of input microstrip SQUID at 519 MHz vs temperature measured with a resonant source: dashed line through the data, $T_N \propto T$; dot-dashed line, $T_Q = hf/k_B \approx 25$ mK. Inset is noise peak produced by LC-tuned circuit at 20 mK. The peak at 520.4 MHz is a calibration signal. From Mück, Kycia, and Clarke, 2001.

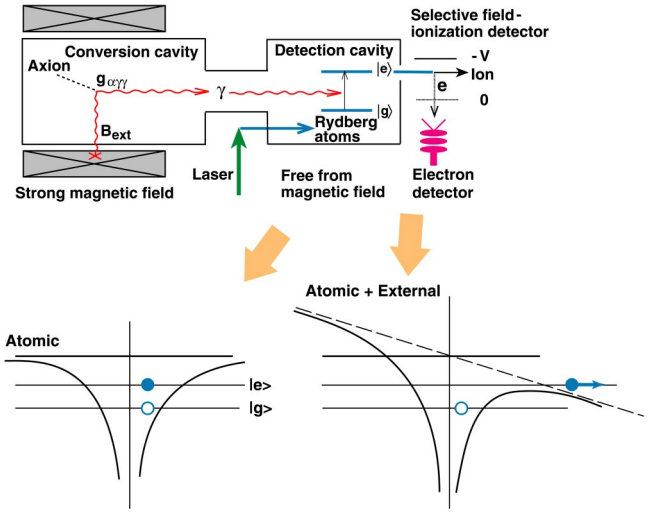

FIG. 34. (Color in online edition) Experimental principle of the Kyoto axion detector with the Rydberg-atom cavity detector. Adapted from Tada *et al.*, 2001.

cause T_N to flatten off. Nonetheless, at about 0.5 GHz, T_N saturates near 50 mK, within a factor of 2 of the quantum limit and a factor of 40 below the noise temperature of state-of-the-art-cooled semiconductor amplifiers. Since Wellstood *et al.* (1994) were able to reduce the temperature of the electrons in the shunts of their SQUID's by a factor of 2–3 at a bath temperature of 20 mK by adding thin-film cooling fins, a similar modification of the microstrip SQUID will likely reduce the noise temperature significantly. There is a very real possibility that the microstrip SQUID amplifier will attain the quantum limit at frequencies of 0.5 GHz and higher.

VII. THE RYDBERG-ATOM SINGLE-QUANTUM DETECTOR

A new detection method for searching for axions using a Rydberg-atom microwave-photon detector in a cavity was developed at the Laboratory of the Nuclear Science Division, Institute for Chemical Research, Kyoto University in Uji, Japan. First, we present the essential ingredients of the Rydberg-atom cavity technique and describe the prototype detector CARRACK1 (Cosmic Axion Research using Rydberg Atoms in a resonant Cavity in Kyoto) constructed in Japan. Next a detailed discussion of the detection efficiency based on quantum-theoretical calculations is presented. The results of these calculations were used by the Kyoto group to design CARRACK2, a large-scale axion search experiment.

A. Experimental principle

The experimental principle of the Rydberg-atom cavity detector (Matsuki and Yamamoto, 1991; Ogawa, Matsuki, and Yamamoto, 1996) is shown schematically in Fig. 34 (upper portion). As in the previously described experiments, axions are converted into photons in the conversion cavity, which is permeated by a strong magnetic field. The photons are transferred to the detection cavity via a coupling hole, where some are absorbed by a beam of Rydberg atoms. Rydberg atoms have large transition dipole moments and therefore have a high quantum efficiency for absorbing photons corresponding to an allowed transition. The atoms are prepared in a lower Rydberg state $|g\rangle$, and the transition frequency to some excited state $|e\rangle$ is adjusted to be equal to the cavity frequency via the Stark effect. After exiting the detection cavity, the excited Rydberg atoms are selectively ionized and detected with the field-ionization method (Gallagher, 1994). *Selective field ionization* is the key to the Rydberg-atom technique; the principle is shown in Fig. 34 (lower portion). Most of the atoms are still in the lower state $|g\rangle$. A few of them are in state $|e\rangle$ by virtue of having absorbed a microwave photon. The beam passes through a parallel-plate arrangement with a prescribed electric field such that the combined (linear + Coulomb) potential results in a barrier for the electrons that traps those in state $|g\rangle$ but leaves those in state $|e\rangle$ unbound (see the following section on selective field ionization for a more realistic description of the phenomenon). These unbound electrons are collected and sent to a channel electron multiplier, where they are counted.

The characteristics and detection efficiency of the Rydberg-atom detector are fundamentally different from those based on microwave amplifiers followed by a heterodyne receiver. The key point is that, since it is a phaseless detector (i.e., like a "phototube" for microwave frequencies), the ultimate noise temperature is not determined by the standard quantum limit. Rather, the ultimate sensitivity is limited by intrinsic noise coming from several sources, such as incomplete separation between the lower and upper states in the field-ionization detection, excitation of the upper state due to the collisions of atoms in the lower Rydberg state with residual gas along the beam path, dark-current noise from the channel electron multiplier, etc. The intrinsic noise due to these sources can be lowered to less than 10 mK in equivalent noise temperature, and thus the sensitivity is primarily limited by the thermal blackbody radiation in the cavity.

1. Rydberg atoms

Rydberg atoms are atomic systems that have been excited to near the ionization limit and in which an electron has been promoted to a level with large principle quantum number n. The Rydberg states currently studied experimentally have $10<n<150$. Classically, the outer electron orbits the core, which comprises the nucleus and the remaining electrons, at a distance n^2a_0, where a_0 is the Bohr radius. Approximating the core as a pointlike charge, the energy spectrum of the Rydberg atom is quasihydrogenic,

$$E_n=\frac{\mathcal{R}}{n^2}.$$

Here $\mathcal{R}$ is the Rydberg constant taking the reduced mass of the electron into account. The effects of the finite core size can be described for alkali atoms (such as Rb, which is used by the Kyoto group) using so-called quantum defect parameters (Seaton, 1958). The energy levels, which depend on the angular momentum ℓ through the number δ_ℓ, are given by

$$\mathrm{E}_{n,\ell}=\frac{\mathcal{R}}{(n-\delta_\ell)^2}=\frac{\mathcal{R}}{\tilde{n}^2}, \tag{35}$$

where $\tilde{n}$ is called the *effective principal quantum number*. The quantum defect parameter δ_l was historically introduced as an empirical parameter to represent the observed energy-level structure of nonhydrogenic atoms (Rydberg, 1890). It is recognized as the phase shift of the wave function of the nonhydrogenic atoms (pulled into the core) in units of π relative to the hydrogen atom (Gallagher, 1994). With this modification, the radiative properties of alkali Rydberg atoms can be estimated using the hydrogen model.

The radiative properties of Rydberg atoms are interesting for microwave photon detection for the following reasons: first, because of their size, the electric dipole matrix element between adjacent levels $\langle n+1|e\mathbf{r}|n\rangle \propto\tilde{n}^2$ is quite large. As a result, the coupling of these atoms to radiation fields is unusually strong. Second, transitions between Rydberg states ($\Delta E_n=E_{n+1}-E_n \approx 2\mathcal{R}/\tilde{n}^2$) fall in the microwave region, $\Delta E_{100}\approx 7$ GHz. Third, these states have long lifetimes, $\tau_n\propto\tilde{n}^3$ ($\ell \ll n$), $\tau_{100}\sim 1$ msec. This means that in spite of the strong coupling to microwaves, they can exist for long times in excited states.

The interaction of a Rydberg atom and a resonant cavity can be understood by considering a two-level atom coupled to a single cavity mode. The coupling between the atom and the cavity field is characterized by the coupling strength Ω, which depends on the dipole matrix element between the atomic levels, and the electric field of the cavity mode. The energy spectrum of the atom-cavity system is given by the eigenvalues of the Jaynes-Cummings Hamiltonian (Jaynes and Cummings, 1963); only the lowest states are important for this discussion. The ground state of the system is $\Psi_0=|g,0\rangle$, where g specifies that the Rydberg atom is in the lower state, and 0 is the number of photons in the cavity. When the cavity frequency is equal to the difference in energy between the atomic levels, the first excited state is twofold degenerate, $\Psi_1=|e,0\rangle$ or $\Psi_1=|g,1\rangle$; either the atom is excited or a photon is created in the cavity. The coupling Ω between the atom and the cavity field breaks the degeneracy, splitting the energy of the two states. The atom and the cavity field exchange energy with frequency Ω, which can now be identified as the Rabi frequency.

This simple picture ignores two important effects: dissipation and the collective behavior of N atoms in a cavity. The cavity has a finite Q and the Rydberg atoms have a finite lifetime, so dissipation processes must be taken into account. The second important effect is that an ensemble of identical atoms inside a cavity behaves as a collective system, not independently as might naively be expected. This is a result of the coupling of all of the atoms to the spatially coherent field inside the cavity (Haroche, 1982, 1990). The spectrum has been exactly calculated (Agarwal, 1984), and the results are simple to interpret for the ground and first excited state. For N atoms, the coupling Ω is replaced by $\Omega_N=\Omega\sqrt{N}$, which is the frequency of the Rabi oscillations for the exchange of energy between the cavity field and the collective atom system.

2. Selective field ionization

As mentioned before, the key to the Rydberg-atom technique is the ability to selectively ionize atoms in a particular Rydberg state. Both the cw and pulsed field-ionization methods can be used to detect Rydberg atoms that have been excited by photon absorption (Gallagher, 1994). The pulsed field method has achieved the greatest selectivity, so it will be the only one described here. Two low-angular-momentum states situated above and below a particular Stark manifold are chosen to be the detection states ($|g\rangle$ and $|e\rangle$). A Stark manifold represents a collection of energy levels that are degenerate in zero electric field, but split approximately linearly under an applied electric field. The results described here use the $111s$ and $111p$ states as the lower and upper detection states, respectively. As shown in Fig. 35, the Stark manifold corresponding to $n=108$ lies between these two states. Due to a characteristic feature of the pulsed field-ionization process in such highly excited Rydberg states (Kishimoto *et al.*, 2002), the bluest (highest) and reddest (lowest) states of the Stark manifold are ionized at quite different field strengths, as shown in Fig. 36(a) (Tada *et al.*, 2002). If atoms in the two detection states are transferred to different states of the Stark manifold, this difference in ionization fields can be exploited to distinguish them.

The first step is to transfer the two detection states to the reddest and bluest states of the Stark manifold. This is accomplished using an adiabatic transfer in the first avoided crossing of the detection state with the corresponding state of the Stark manifold. Figure 35(b) shows this process for the lower detection state; when the electric-field strength increases sufficiently slowly, atoms in the lower state follow the trajectory of the solid line and are adiabatically transferred to the reddest state of the Stark manifold. A similar process occurs at the avoided crossing of the upper detection state with the bluest state of the Stark manifold.

In the usual forward-driving technique, after the adiabatic transfer, the electric field is very rapidly increased and the ionization spectrum contains separate peaks corresponding to the different ionization energies of the reddest and bluest states.

It turns out that the selection efficiency is enhanced using the backward-driving technique (Tada *et al.*, 2002). In this case, after the adiabatic transfer, the electric field is rapidly switched off, and then increased rapidly to a large field in the opposite direction of the adiabatic field [see Fig. 35(c)]. The transfer through the avoided cross-

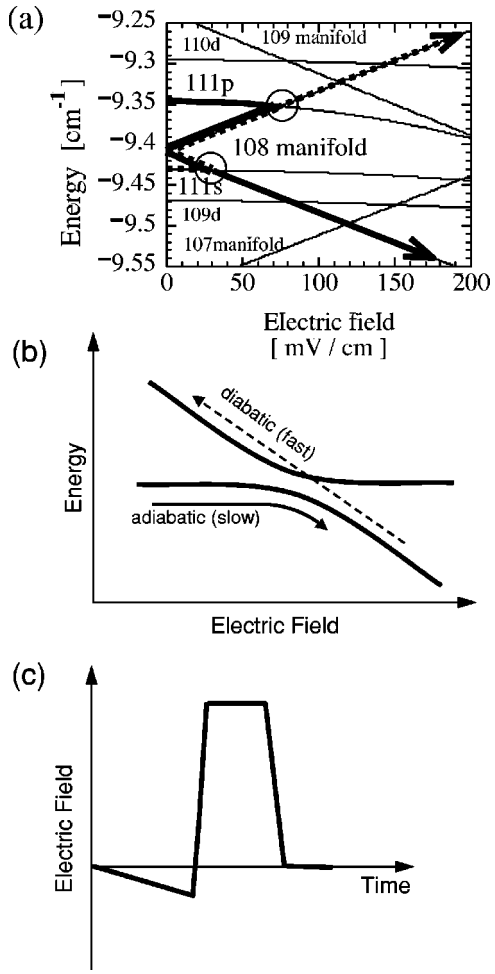

FIG. 35. The backward-driving pulsed selected field-ionization (SFI) scheme: (a) the low-field Stark energy diagrams near the $n=108$ manifold together with the ionization paths manipulated for the 111s and 111p states; (b) simplification of the first avoided crossing of the the 111s state and the Stark manifold shown in the lower circle of (a); (c) electric-field profile of the pulse used in the backward-driving scheme. Here the slow component is exaggerated for clarity. From Tada *et al.*, 2002.

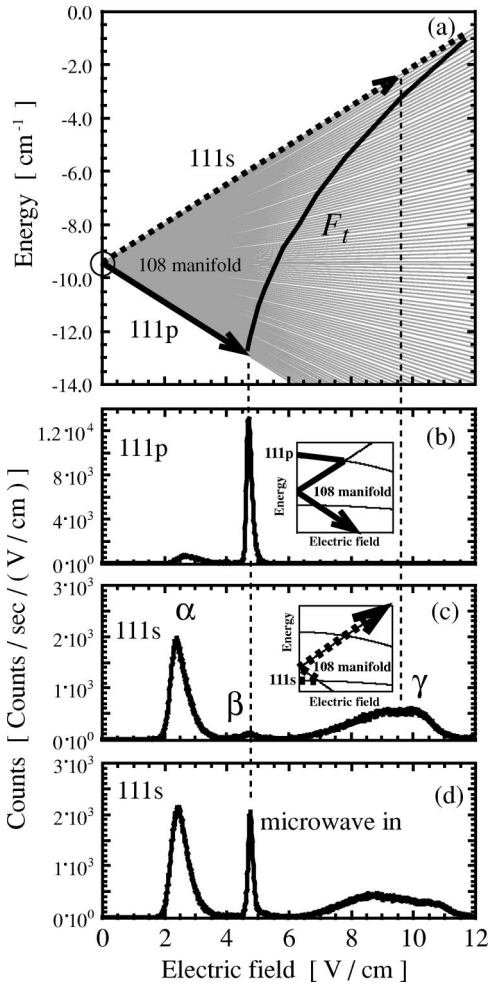

FIG. 36. Typical ionized electron spectra obsered with the pulsed SFI scheme: (a) the $n=108$ Stark manifold together with the ionization paths manipulated for the 111s and 111p states. The circle indicates the low-field region shown in Fig. 35(a). The expected threshold field strength from the tunneling ionization process is shown by the solid line F_t; (b)–(d) Field-ionization spectra of 111p and 111s states in the backward-driving scheme. Manipulated path trajectories at the low-field region in the ionization process are schematically shown in the insets of (b) and (c); (b) 111p state; (c) 111s state; (d) 111s state initially excited by a microwave source, the frequency of which is set to be equal to the transition frequency between the $111s_{1/2}$ and $111p_{3/2}$ states. From Tada *et al.*, 2002.

ing after the field is switched off is diabatic, meaning that the atoms remain in the Stark manifold. The dashed line of Fig. 35(b) shows the trajectory for the atoms in the lower detection state as the field is switched off. In this zero-field-crossing mode, the lower detection state is now transferred to the bluest state of the Stark manifold and hence ionizes at a higher electric field. With the zero-field-crossing mode, the ionization signals from the tunneling process are enhanced compared to the forward-driving method [sharp peak in Fig. 36(b)], thus more efficient selectivity can be achieved.

Figure 36(c) shows a typical ionized electron spectrum observed with this pulsed-selective field-ionization scheme (Tada *et al.*, 2002). Here the 111s state is first excited by two-step laser excitation from the ^{86}Rb $5s_{1/2}$ ground state via the intermediate $5p_{3/2}$ state. After passing through the detection cavity, the Rydberg atoms are ionized using the backward-driving technique. The initially prepared lower (111s) state and the upper (111p) state partially populated by photon absorption are transferred to the reddest and bluest states in the manifold. The peak β in Fig. 36(c) corresponds to the transition of the 111s state to the 111p state by photon absorption (frequency is 2.540 GHz).

Selectivity in the field ionization is further enhanced when a three-step electric-field pulse is applied, as in Fig. 37 (Tada *et al.*, 2002). As shown in Fig. 37(d), each ionization peak is well separated by the applied three-step pulse. This separation is achieved because the ionization due to the autoionizationlike process [peak α in Fig. 36(c)] has a rather long lifetime, which depends on the applied electric field. This peak is further separated from the second peak [β in Fig. 36(c)] by keeping the

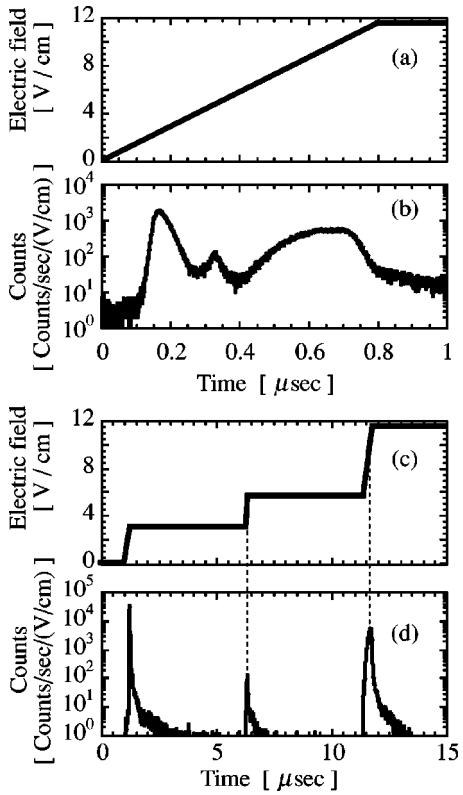

FIG. 37. Pulse profile and the corresponding field-ionization spectrum of the 111*s* state obtained with the advanced three-step field-ionization scheme together with those for the standard one-step scheme presented in Fig. 36. Note here that the slow component of the applied pulse in this backward-driving scheme is omitted in the profile drawing of both (a) and (c) for simplicity. (a) and (b) One-step pulse profile adopted in the previous standard backward-driving scheme as presented in Fig. 36 and corresponding timing spectrum on a logarithmic scale. (c) and (d) Advanced three-step pulse profile in the backward-driving scheme and corresponding timing spectrum observed. From Tada *et al.*, 2002.

electric field low for a relatively long time, as shown in Fig. 37(c). The peak separation is improved by more than two orders of magnitude; thus the effective noise temperature due to the incomplete separation for the lower and the upper states is less than 10 mK.

B. The CARRACK1 detector

Based on the principles described above, a prototype Rydberg-atom cavity detector was built and operated by the Kyoto group. Figure 38 shows a schematic of the CARRACK1 detector.

Axions are converted to photons in the conversion cavity, which is threaded by a strong magnetic field. These photons are coupled to the detection cavity through a coupling hole. The detection cavity must be separate from the conversion cavity, otherwise the Zeeman splitting of the Rydberg energy levels by the magnetic field would be too complex. This complexity is avoided by placing the detection cavity in a magnetic-field-free region.

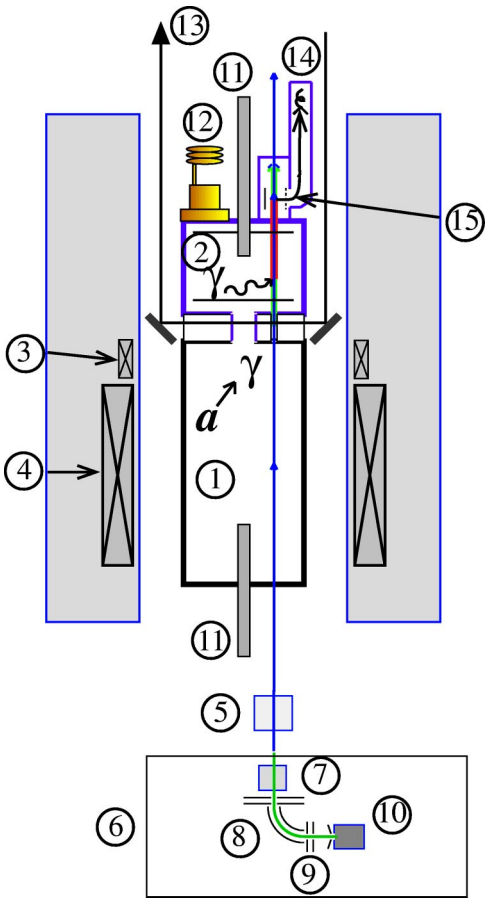

FIG. 38. (Color in online edition) Schematic diagram of the prototype experimental system to search for cosmic axions with Rydberg atoms in cooled resonant cavities: (1) conversion cavity; (2) detection cavity; (3) cancellation coil; (4) main superconducting magnet coil; (5) thermal atomic beam oven; (6) ion source and neutralization system; (7) neutralizer with resonant charge-exchange reaction; (8) bending and focusing electrodes; (9) accelerating electrodes; (10) ion source of surface ionization type; (11) tuning rod; (12) dilution refrigerator system; (13) laser beam; (14) field-ionization system; (15) ionization electrodes. From Tada *et al.*, 2001.

A beam of Rb atoms produced either by an oven or by an ion source-neutralizer system is injected into the cavity system. The ground-state beam passes through the conversion cavity with no effect. Just before entering the detection cavity, the atoms are excited to a Rydberg state $|g\rangle$ by two- or three-step laser excitation using narrow-bandwidth single-mode lasers. The laser beams are introduced into the top of the cryostat and after interacting with the atomic beam they exit through a glass window. While passing through the detection cavity, the Rydberg atoms may be excited to the state $|e\rangle$ by absorbing a photon. The spacing between the levels $|g\rangle$ and $|e\rangle$ is tuned by the Stark shift to match the resonant frequency of the cavity.

After exiting the cavity, the atoms in state $|e\rangle$ are selectively ionized at the field-ionization electrode, and the resulting electrons are guided through a series of focusing ring electrodes to the channel electron multiplier. In this way, the Rydberg atoms excited to the state

$|e\rangle$ are individually detected.

Blackbody photons in the cavity will also excite atoms to the $|e\rangle$ state, which in principle limits the sensitivity of this technique. To reduce the number of thermal photons, the cavity and detection system are cooled to roughly 15 mK with a dilution refrigerator.

1. Apparatus

The cavity system consists of two cylindrical TM_{010} single-mode cavities of the same inner diameter. The conversion cavity is made of oxygen-free high-conductivity copper, while the detection cavity is made of superconducting niobium to expel the external magnetic field with the Meissner effect.

Because of the coupling between the two cavities, there is a splitting of the TM_{010} mode. The strength of the coupling determines the frequency separation of the two eigenmodes. The design of the coupler is performed with computer codes taking the frequency separation into account. Depending on the electric-field distribution in the cavity and the rod-position dependence of the resonant frequency, one of the split modes is selected as the resonant mode of the cavity for the detection system.

2. Frequency tuning

Tuning of the resonant frequency is accomplished by inserting dielectric rods in both the conversion and the detection cavities along the cylindrical symmetry axis. This method was adopted because of the simplicity of driving the rods from outside the cryostat with stepping motors, although the cavity form factor is not optimal due to mode localization. The rod for the detection cavity is driven from the top of the cryostat, while the one for the conversion cavity is driven from the bottom. Aluminum-oxide rods with 7 to 10 mm diameter are used for both cavities; the diameter is chosen to achieve the desired tuning range.

A measurement of the frequency range covered by a typical tuning rod in the conversion cavity is shown in Fig. 39. The calculated dependence of the conversion form factor C [Eq. (49)] on the rod length is also shown. The electric-field distribution in the cavity is affected by the inserted rod position. Although the electric-field direction is not always perfectly parallel to the cylindrical axis, the whole field distribution is approximately that of the TM_{010} mode over the full tuning range. The loaded Q value observed is $Q_L=(3.5–4.5)\times10^4$.

Electrodes for introducing Stark shifts of the Rydberg states are inserted along the beam path in the detection cavity. The electrodes are used to finely tune the Rydberg-atom transition frequency to match to the cavity resonant frequency.

Since the cavities are cooled to near 10 mK, it is important to minimize the heat load from the high-temperature side. The tuning rod driving system is especially challenging in this regard, since there is a mechanical connection from the cavities and stepper motors to room temperature. The solution is to thermally anchor the driving system at several points. In addition, the rod for the conversion cavity is moved via Kevlar strings. The Kevlar string has very low heat conductivity, enough tensile strength to drive a rod of weight $\sim$100 g, and low extensibility (Tada *et al.*, 2001).

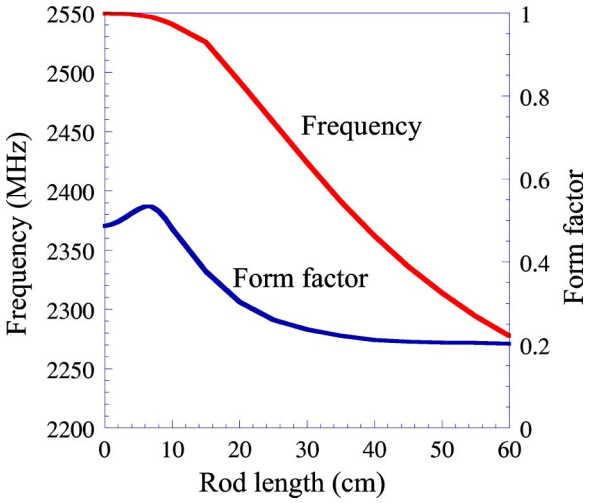

FIG. 39. (Color in online edition) The variations of the measured resonant frequency and the calculated conversion form factor with the position of the tuning rod in the conversion cavity.

3. Magnetic-field shielding in the detection cavity

A magnetic-field-free region for the detection cavity is created in two stages. First, the external magnetic field at the detection cavity is reduced to less than 0.09 T with a superconducting coil (cancellation coil). Second, the detection cavity and coupling parts are constructed from Nb metal, which upon becoming superconducting expels the interior magnetic field via the Meissner effect. In order to achieve a field-free region in the detection cavity, the effects of the demagnetization field induced by the superconducting Nb have to be carefully taken into account.

4. Selective field-ionization detector

The selective field-ionization detector consists of three parts: the field-ionization electrodes, transport electrodes for the ionized electrons, and an electron multiplier for detecting the electrons. A cross-sectional view of the system is schematically shown in Fig. 40.

The field-ionization electrodes are located in the Nb box on the bottom plate of the mixing chamber. The Rydberg atoms enter the electrodes after passing through the detection cavity. The ionized electrons are then transported by a number of focusing ring electrodes into the electron multiplier.

This configuration keeps the cavity and the field-ionization parts as cold as possible. The channel electron multiplier produces a resistive heat load as large as 10 mW and does not work properly at temperatures lower than 20 K. For these reasons, the channel electron multiplier is heated with a Nichrome coil surrounding it and

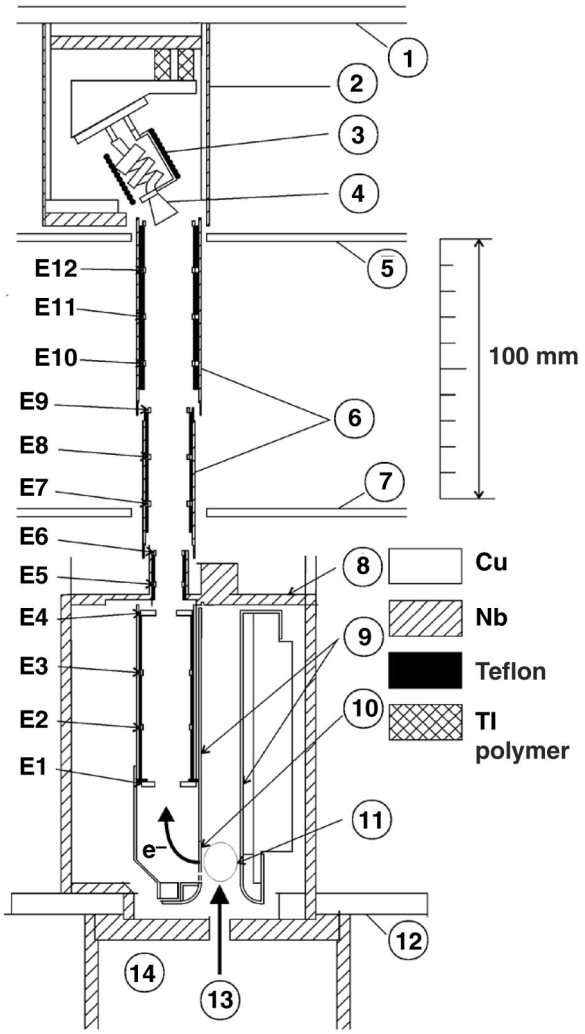

FIG. 40. Cross-sectional view of the selective field-ionization system: (1) plate for the 1-K pot; (2) housing for the channel electron multiplier (CEM); (3) a Nichrome coil for heating up the (CEM) to more than 20 K; (4) CEM; (5) plate for the still; (6) Nb tube; (7) plate for the heat exchanger, called the cold plate; (8) Nb housing box; (9) electrodes for the field ionization; (10) copper mesh to transport the electrons; (11) field-ionization region; (12) plate for the mixing chamber; (13) Rydberg atomic beam; (14) detection cavity made of Nb. $E1$–$E12$ represent the ring electrodes for the transportation of the ionized electrons.

is thermally isolated by supporting it with TI polymer, a low-thermal-conductivity dielectric material.

The system has been utilized to search for axions at 10 μeV mass region and the results on the constraint of the coupling constant $g_{a\gamma\gamma}$ are being evaluated (Yamamoto *et al.*, 2001).

C. Quantum-theoretical description of the detector system

The CARRACK1 detector demonstrated that selective field ionization of Rydberg atoms could be used to detect photons in a resonant cavity. Optimizing this process for axion detection requires a more complete understanding of axion-photon-atom interactions. This section contains a theoretical treatment of the Rydberg-atom single-quantum detector, which serves as the basis for the next-generation experiment being developed by the Kyoto group.

The Rydberg-atom cavity detector is treated as a dynamical system of interacting quantum oscillators with dissipation describing the axions, photons, and Rydberg atoms (Ogawa, Matsuki, and Yamamoto, 1996; Yamamoto and Matsuki, 1998, 1999; Kitagawa, Yamamoto, and Matsuki, 1999). The axion is treated as a quantum oscillator with a dissipation term coming from the finite broadening of its kinetic energy. This loss term in the Hamiltonian is introduced as an analogy to a loss but does not represent an actual loss. This quantum-dynamical system provides the basis for investigating various properties of the axion-photon-atom system. Here the essential features of this quantum system are discussed with an emphasis on the dependence of the detection efficiency on the various experimental parameters. Finally, requirements for an optimum-efficiency detector system are discussed, and the large-scale axion search apparatus CARRACK2 (Tada *et al.*, 1999) is described.

1. Properties of the axion-photon-atom system in resonant cavities

Quantum oscillators with dissipation for the axion-photon-atom interacting system in a resonant cavity are characterized by their energy ω_i, damping rate γ_i, and mutual interactions, where $i(=a,b,c)$ denotes axion, atom, and photon, respectively. The properties of these quantum oscillators are summarized as follows.

The initial average quantum state occupation numbers of axions, atoms in the upper state, and photons are estimated as

$$\overline{n_a}=\frac{\rho_a\lambda_d^3}{m_a}=5.7\times10^{25}\left(\frac{\rho_a}{0.3\ \mathrm{GeV\,cm^{-3}}}\right)\times\left(\frac{10^{-3}}{\beta_a}\right)^3\left(\frac{10^{-5}\ \mathrm{eV}}{m_a}\right)^4, \tag{36}$$

$$\overline{n_b}=0, \tag{37}$$

$$\overline{n_c}=(e^{\hbar\omega_c/k_BT_c}-1)^{-1}. \tag{38}$$

Here λ_d is the de Broglie wavelength of axions, and the energy density of cosmic axions ρ_a is a characteristic value $\rho_{\mathrm{halo}}=0.3\ \mathrm{GeV\,cm^{-3}}$. The Rydberg atoms are initially prepared exclusively in the lower state, resulting in Eq. (37).

The spread in the axion energies is

$$\gamma_a\sim\beta_a^2m_a/\hbar=10^{-11}\ \mathrm{eV}\hbar^{-1}\left(\frac{m_a}{10^{-5}\ \mathrm{eV}}\right)\left(\frac{\beta_a}{10^{-3}}\right)^2. \tag{39}$$

The decay rates of the atoms and photons are

$$\gamma_b=6.6\times10^{-13}\ \mathrm{eV}\hbar^{-1}\left(\frac{10^{-3}\ \mathrm{sec}}{\tau_b}\right), \tag{40}$$

$$\gamma_c \equiv \gamma = 5\times 10^{-10}\ \text{eV}\hbar^{-1}\left(\frac{\hbar\omega_c}{10^{-5}\ \text{eV}}\right)\left(\frac{2\times 10^4}{Q}\right). \quad (41)$$

Here, τ_b is the lifetime of the Rydberg state, typically $\tau_b \sim 10^{-3}$ sec for $n\sim 100$ in the vacuum (Gallagher, 1994).

2. Axion-photon interaction

The axion-photon interaction in a strong static magnetic field with flux density B_0 is described by the Lagrangian density (as described earlier)

$$\mathcal{L}_a = \hbar^{1/2}\epsilon_0 g_{a\gamma\gamma}\phi \boldsymbol{E}\cdot\boldsymbol{B}_0, \quad (42)$$

where $\hbar^{1/2}$ and ϵ_0 are explicitly factored out so that the Lagrangian density has the right dimension $\mathcal{L}_a \sim [\hbar\,\text{sec}^{-1}\,\text{m}^{-3}]\sim[\text{eV}\,\text{m}^{-3}]$ with the axion-photon-photon coupling constant $g_{a\gamma\gamma}\sim[\text{eV}^{-1}]$.

The electric-field operator in the cavity volume V is given by

$$\boldsymbol{E}(\mathbf{x},t) = (\hbar\omega_c/2\epsilon_0)^{1/2}[\boldsymbol{\alpha}(\mathbf{x})c(t) + \boldsymbol{\alpha}^*(\mathbf{x})c^\dagger(t)] \quad (43)$$

for a mode with a resonant frequency ω_c. The creation and annihilation operators satisfy the usual commutation relation, $[c,c^\dagger]=1$. The whole cavity may be viewed as a combination of two coupled subcavities, the *conversion cavity* with volume V_1 and the *detection cavity* with volume V_2, which are coupled together with $V = V_1 + V_2$. The electric field of the mode can then be divided as

$$\boldsymbol{\alpha}(\mathbf{x}) = \boldsymbol{\alpha}_1(\mathbf{x}) + \boldsymbol{\alpha}_2(\mathbf{x}), \quad (44)$$

where $\boldsymbol{\alpha}_1(\mathbf{x}) = \mathbf{0}$ for $\mathbf{x}\in V_2$ and $\boldsymbol{\alpha}_2(\mathbf{x}) = \mathbf{0}$ for $\mathbf{x}\in V_1$, respectively. The normalization condition of $\boldsymbol{\alpha}(\mathbf{x})$ is

$$\int_{V_1} |\boldsymbol{\alpha}_1(\mathbf{x})|^2 d^3x + \int_{V_2} |\boldsymbol{\alpha}_2(\mathbf{x})|^2 d^3x = 1. \quad (45)$$

The coupling between the two cavities splits the mode into two modes with energies ω_c and ω_c'. The coupling strength is adjusted to give a sufficient separation between the two modes ($|\omega_c - \omega_c'| \gg \gamma$). In this case, only one of the modes is close to the axion frequency ω_a.

The Lagrangian density for the axion-photon-photon coupling implies the effective interaction Hamiltonian between the coherent axion mode a and the resonant radiation mode c,

$$H_{ac} = \hbar\kappa(a^\dagger c + a c^\dagger). \quad (46)$$

The coupling constant κ is given for $\omega_c \simeq m_a/\hbar$,

$$\begin{aligned}\kappa &= \hbar^{1/2} g_{a\gamma\gamma}\epsilon_0^{1/2} B_{\text{eff}}\left[\left(\frac{\beta_a m_a}{2\pi\hbar}\right)^3 \frac{V_1}{2}\right]^{1/2} \\ &= 4\times 10^{-26}\ \text{eV}\hbar^{-1}\left(\frac{g_{a\gamma\gamma}}{1.4\times 10^{-15}\ \text{GeV}^{-1}}\right)\left(\frac{B_{\text{eff}}}{4\ \text{T}}\right) \\ &\quad\times\left(\frac{\beta_a m_a}{10^{-3}\times 10^{-5}\ \text{eV}}\right)^{3/2}\left(\frac{V_1}{5000\ \text{cm}^3}\right)^{1/2}, \end{aligned} \quad (47)$$

where

$$B_{\text{eff}} = \zeta_1 C B_0, \quad (48)$$

and B_0 is the maximum density of the external magnetic flux. The axion-photon-photon coupling constant $g_{a\gamma\gamma}$ is normalized to the value expected in the DFSZ axion model with $m_a = 10^{-5}$ eV.

The form factor C for the magnetic field is given by

$$C = \zeta_1^{-1} V_1^{-1/2}\left|\int_{\mathcal{V}_1} d^3x\, \boldsymbol{\alpha}_1(\mathbf{x})\cdot[\boldsymbol{B}_0(\mathbf{x})/B_0]\right| \quad (49)$$

with

$$\zeta_1 = \left[\int_{\mathcal{V}_1} d^3x |\boldsymbol{\alpha}_1(\mathbf{x})|^2\right]^{1/2}. \quad (50)$$

3. Atom-photon interaction

In the experimental system, the Rydberg atoms are injected as a uniform beam; this implies that a certain number N of Rydberg atoms are constantly present in the cavity. Such an ensemble of identical atoms behaves as a collective system in their interaction with the resonant radiation mode. Suppose for simplicity that the N atoms are at the antinodal position of the electric field in the detection cavity. Then the effective coupling between the resonant photons and the N atoms is given by

$$H_{bc} = \hbar\Omega_N(b^\dagger c + b c^\dagger), \quad (51)$$

where b is the collective atomic mode operator satisfying the commutation relation $[b,b^\dagger]=1$. The value of the collective coupling constant Ω_N is

$$\Omega_N = 1\times 10^{-10}\ \text{eV}\hbar^{-1}\left(\frac{\Omega}{5\times 10^3\ \text{sec}^{-1}}\right)\left(\frac{N}{10^3}\right)^{1/2} \quad (52)$$

for typical values of Ω and N. In practice, Ω_N will have position and time dependence due to the local variation of the electric field in the cavity mode.

4. Evolution in the Liouville picture

The reduced density matrix of the damped oscillators q_i (a, b, and c) obeys the Liouville equation (see, for example, Louisell, 1990),

$$\frac{d\rho}{dt} = \frac{1}{i\hbar}[H,\rho] + \Lambda\rho. \quad (53)$$

The Liouvillian relaxations are represented by the operator $\Lambda\rho$, which is given by

$$\begin{aligned}\Lambda\rho &= \sum_i \frac{\gamma_i}{2}[2q_i\rho q_i^\dagger - q_i^\dagger q_i\rho - \rho q_i^\dagger q_i] \\ &\quad + \sum_i \gamma_i\overline{n_i}[q_i^\dagger\rho q_i + q_i\rho q_i^\dagger - q_i^\dagger q_i\rho - \rho q_i q_i^\dagger], \end{aligned} \quad (54)$$

where γ_i and $\overline{n_i}$ are the damping rates and equilibrium occupation numbers, respectively. The total Hamiltonian is given by

$$H = \sum_i \hbar\omega_i q_i^\dagger q_i + \sum_{i\neq j}\hbar\Omega_{ij}(t) q_i^\dagger q_j, \quad (55)$$

where $\Omega_{ij}(t) = \Omega_{ji}^*(t)$ represent the interaction terms,

which may be time dependent, as is the case for the interaction between the photons and the atoms moving in the cavity.

The Liouville equation implies, in the coherent-state basis, a Fokker-Planck equation for the distribution function P:

$$\frac{\partial P}{\partial t}=i\mathcal{H}_{ij}(t)\frac{\partial}{\partial\alpha_i}(\alpha_j P)-i\mathcal{H}_{ij}^{*}(t)\frac{\partial}{\partial\alpha_i^{*}}(\alpha_j^{*}P)+\mathcal{D}_{ij}\frac{\partial^2 P}{\partial\alpha_i\partial\alpha_j^{*}}. \tag{56}$$

The effective Hamiltonian $\mathcal{H}(t)$ and diffusion term $\mathcal{D}$ are given by

$$\mathcal{H}_{ij}(t)=\left(\omega_i-\frac{i}{2}\gamma_i\right)\delta_{ij}+\Omega_{ij}(t)(1-\delta_{ij}), \tag{57}$$

$$\mathcal{D}_{ij}=\gamma_i\overline{n}_i\delta_{ij}. \tag{58}$$

Explicitly, for the axion-photon-atom system,

$$\mathcal{H}(t)=\begin{pmatrix}\omega_b-\frac{i}{2}\gamma_b & \Omega(t) & 0\\ \Omega(t) & \omega_c-\frac{i}{2}\gamma_c & \kappa\\ 0 & \kappa & \omega_a-\frac{i}{2}\gamma_a\end{pmatrix} \tag{59}$$

with $\omega_a=m_a/\hbar$, and

$$\mathcal{D}=\begin{pmatrix}\gamma_b\overline{n}_b & 0 & 0\\ 0 & \gamma_c\overline{n}_c & 0\\ 0 & 0 & \gamma_a\overline{n}_a\end{pmatrix}. \tag{60}$$

The collective atom-photon coupling is time dependent,

$$\Omega(t)=\Omega_N f(vt), \tag{61}$$

because the atoms move with velocity v. The function f is the electric-field profile of the detection cavity mode along the atomic beam.

In the simple case with constant atom-photon coupling $\Omega(t)=\Omega_N$, an analytic solution is obtained for the particle numbers

$$n_i(t)=\langle q_i^{\dagger}q_i\rangle=r_{ic}(t)\overline{n}_c+r_{ia}(t)\overline{n}_a, \tag{62}$$

where

$$r_{ij}(t)=\sum_{m,n}g_{ij}^{m}{}^{*}g_{ij}^{n}\left[\left(1-\frac{\gamma_j}{\Lambda_{mn}}\right)e^{-\Lambda_{mn}t}+\frac{\gamma_j}{\Lambda_{mn}}\right] \tag{63}$$

with

$$g_{ij}^{k}=\lim_{s\to-i\lambda_k}(s+i\lambda_k)(s\mathbf{1}+i\mathcal{H})_{ij}^{-1}, \tag{64}$$

$$\Lambda_{mn}=-i(\lambda_m^{*}-\lambda_n). \tag{65}$$

Here λ_i $(i=a,b,c)$ are the eigenvalues of the effective Hamiltonian $\mathcal{H}(t)$.

Since the Rydberg atomic beam is injected into, and then extracted from, the resonant cavity, the evolution of the above interacting system is cut off by the transit time given by

$$t_{\mathrm{tr}}=L/v. \tag{66}$$

L is the distance through the cavity. (It is assumed here for simplicity that the atoms have uniform velocity.) Typically $t_{\mathrm{tr}}\simeq 400\tau_\gamma$ with $L=0.2$ m, $v=350\ \mathrm{m\,sec^{-1}}$, $m_a=10^{-5}$ eV, and $Q=2\times10^4$. Hence the transit time can be chosen to be long enough, i.e.,

$$t_{\mathrm{tr}}>\text{several}\ \ \gamma_a^{-1} \tag{67}$$

with $\gamma_a\sim\beta_a^2 m_a$, so that the different particle numbers will practically reach their asymptotic values:

$$r_{ij}(t_{\mathrm{tr}})\approx r_{ij}(\infty)=\sum_{m,n}g_{ij}^{m}{}^{*}g_{ij}^{n}\frac{\gamma_j}{\Lambda_{mn}}. \tag{68}$$

Then the number of axion-converted photons is given approximately by

$$n_c[a\to c]\approx r_{ca}(\infty)\overline{n}_a. \tag{69}$$

and the number of excited atoms due to the axion-converted photons is given by

$$n_b[a\to c\to b]\approx r_{ba}(\infty)\overline{n}_a. \tag{70}$$

5. Optimum-sensitivity setup

Calculations based on the above analytical solution (Ogawa, Matsuki, and Yamamoto, 1996) give essentially the same results as more detailed numerical calculations performed to see the effect of the various experimental parameters on the detection efficiency (Yamamoto and Matsuki, 1998, 1999; Kitagawa, Yamamoto, and Matsuki, 1999). The latter take account of the time dependence of the atom-photon interaction due to atomic motion in the cavity. The spatial distribution of the electric field of the cavity mode along the atomic beam direction was also taken into account. Figure 41 shows an example of the signal and noise rates versus the atomic beam intensity I_{Ryd}. Here the remarkable point is that the noise rate saturates at a certain value of the beam intensity as a result of the thermal equilibrium between the photons and the atomic system (Raimond *et al.*, 1982). The saturated number of excited atoms is proportional to the number of photons in the cavity $\overline{n}_c$; the frequency dependence of $\overline{n}_c$ is shown in Fig. 42.

The signal rate from axion conversion, on the other hand, reaches a maximum for some number of Rydberg atoms injected. The existence of this maximum is easy to understand qualitatively. The power from axion-to-photon conversion [Eq. (14)] is proportional to the Q of the cavity. Rydberg atoms exiting the cavity in the excited state extract power from the cavity, thereby decreasing Q as well as the signal power. The optimum value of N is large enough so that the atomic system reaches thermal equilibrium with the photons from axion conversion, but not so large as to overload the cavity. This is analogous to achieving critical coupling in the detectors using HFET amplifiers to couple power from the cavity.

The experimental parameters that can be chosen to achieve maximum detection efficiency are

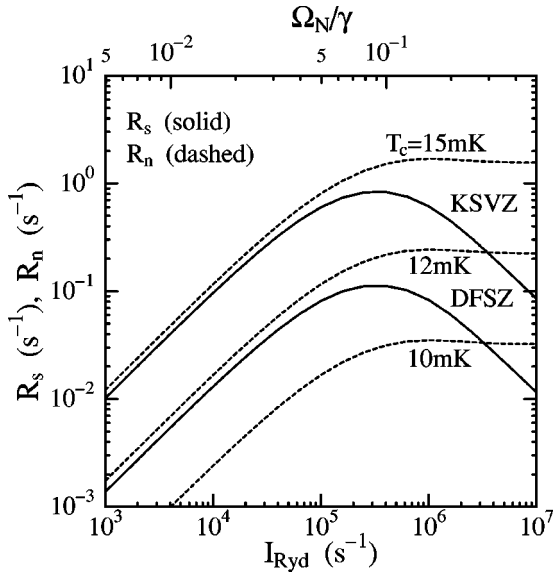

FIG. 41. The signal and noise rates vs the atomic beam intensity. The relevant parameters are $m_a=10^{-5}$ eV ($\Delta\omega_a=0$), $\beta_a=10^{-3}$, $\gamma_a=\beta_a^2 m_a$, $Q=2\times10^4$, $L=0.2$ m, $v=350$ m sec^{-1}, $\Omega=5\times10^3$ sec^{-1}, and $T_c=10$, 12, 15 mK. From Kitagawa, Yamamoto, and Matsuki, 1999.

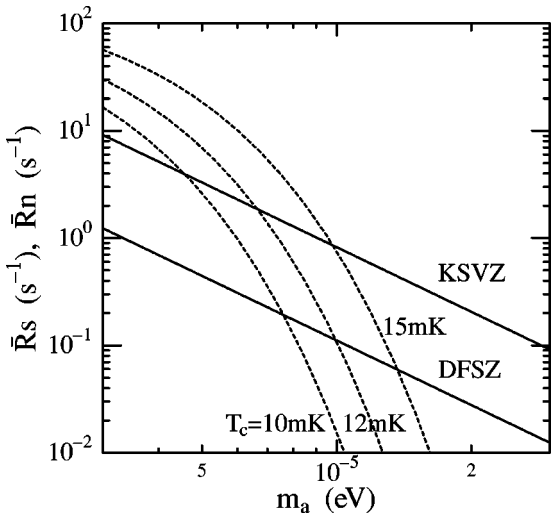

FIG. 43. The estimates of the optimal counting rates of signals $\overline{R_s}$ (solid lines) and of noise $\overline{R_n}$ (dashed lines) are shown depending on the axion mass m_a for the KSVZ and DFSZ models at the cavity temperatures $T_c=10$, 12, 15 mK. The relevant parameters are $\overline{\gamma_a}=\gamma_a+\gamma_{\rm tr}$, $\gamma_a=\beta_a^2 m_a$, $\beta_a=10^{-3}$, $Q=2\times10^4$, $L=0.2$ m, $\Omega=5\times10^3$ sec^{-1}, $v=350$ m sec^{-1}($m_a/10^{-5}$ eV), and $V_1=5000$ cm^3($m_a/10^{-5}$ eV)$^{-2}$. From Kitagawa, Yamamoto, and Matsuki, 2000.

detunings: $\Delta\omega_a\equiv\omega_a-\omega_c$, $\Delta\omega_b\equiv\omega_b-\omega_c$,

couplings: κ, Ω_N,

dampings: γ_a, γ_b, $\gamma_c\equiv\gamma$,

uncertainty: $\gamma_{\rm tr}=t_{\rm tr}^{-1}$.

The optimum values of the adjustable parameters are estimated to be

$$\overline{\Omega}_N\sim0.1\gamma\left(\frac{\beta_a}{10^{-3}}\right)\left(\frac{Q}{2\times10^4}\right)^{1/2}, \tag{71}$$

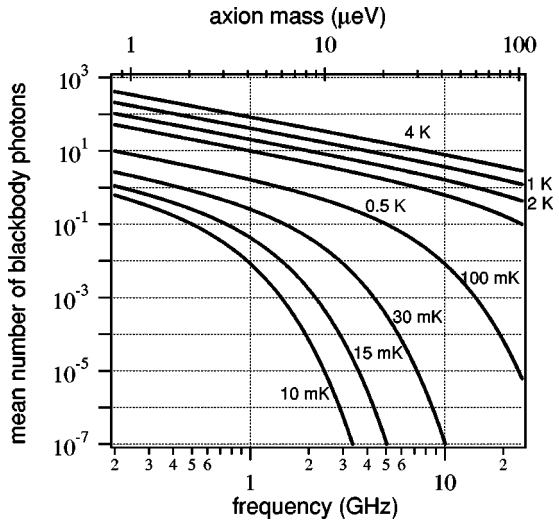

FIG. 42. (Color in online edition) Frequency dependence of the average number of thermal photons present in a single cavity mode as a function of temperature. From Tada *et al.*, 1999.

$$\overline{N}\sim10^2\ \text{atoms}\left(\frac{\beta_a}{10^{-3}}\right)^2\left(\frac{m_a}{10^{-5}\ \text{eV}}\right)^2\times\left(\frac{Q}{2\times10^4}\right)^{-1}\left(\frac{\Omega}{5\times10^3\ \text{sec}^{-1}}\right)^{-2}, \tag{72}$$

$$\overline{I}_{\rm Ryd}\sim(10^5-10^6)\ \text{sec}^{-1}\left(\frac{\beta_a}{10^{-3}}\right)^4\left(\frac{m_a}{10^{-5}\ \text{eV}}\right)^3\times\left(\frac{Q}{2\times10^4}\right)^{-1}\left(\frac{\Omega}{5\times10^3\ \text{sec}^{-1}}\right)^{-2}. \tag{73}$$

The scanning frequency step is taken to be

$$\Delta\omega_c\sim\overline{\gamma_a}\sim2.4\ \text{kHz}\left(\frac{\beta_a}{10^{-3}}\right)^2\left(\frac{m_a}{10^{-5}\ \text{eV}}\right). \tag{74}$$

It is noted here that the single atom-photon coupling constant Ω can be predicted rather precisely from atomic structure calculations, and the calculated value can be compared with experimental data obtained by measuring the dependence of the thermal-photon noise rate on the number of injected Rydberg atoms $I_{\rm Ryd}$ (Yamamoto *et al.*, 2001).

The count rates expected from axion conversion photons and from blackbody photons, respectively, are given by

$$\overline{R}_s\sim4(v/L)(\gamma/\overline{\gamma}_a)(\kappa/\gamma)^2\overline{n}_a, \tag{75}$$

$$\overline{R}_n\sim(v/L)\overline{n}_c[m_a/T_c], \tag{76}$$

for the optimum setup, where the thermal photon number $\overline{n}_c$ is evaluated at $\omega_c\simeq m_a$. The mass dependence of the optimum counting rates is shown in Fig. 43.

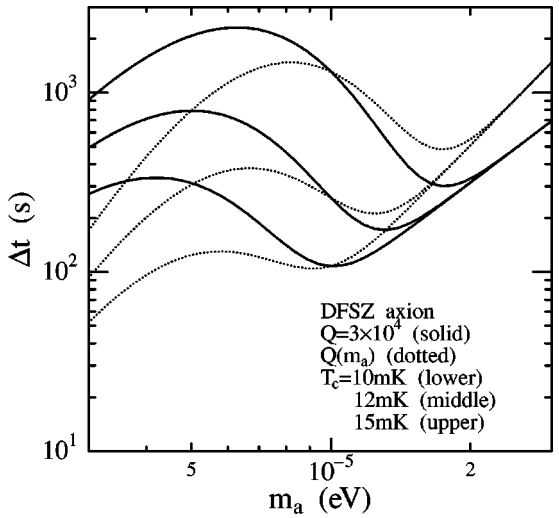

FIG. 44. The one-step measurement time for 3σ is shown depending on the axion mass. These calculations are made for the DFSZ axion (Zhitnitskii, 1980; Dine *et al.*, 1981) with the optimum setup of the relevant experimental parameters as given in the text. Solid lines, Q factors are fixed; dotted lines, frequency (f) dependence of Q factors is assumed to be proportional to $f^{-2/3}$. From Kitagawa, Yamamoto, and Matsuki, 1999.

With the counting rates $R_s \approx \overline{R}_s$ and $R_n \approx \overline{R}_n$ the measurement time required to search for an axion signal at the confidence level of $m\sigma$ is given by

$$\Delta t = \frac{m^2(1+R_n/R_s)}{R_s} \sim \begin{cases} m^2(R_n/R_s)R_s^{-1} & (R_s \ll R_n) \\ m^2 R_s^{-1} & (R_s \gg R_n). \end{cases} \tag{77}$$

The total scanning time over a 10% frequency range is then

$$t_{\rm tot} = \frac{0.1\omega_c}{\Delta\omega_c}\Delta t \sim 10^5 \left(\frac{\beta_a}{10^{-3}}\right)^{-2} \Delta t, \tag{78}$$

with $\Delta\omega_c$ given by Eq. (74).

The axion-mass dependence of the one-step measurement time Δt at a 3σ confidence level with the optimized experimental conditions is shown in Fig. 44 for DFSZ-model axions.

D. The CARRACK2 detector

Following the above theoretical analysis of the optimal experimental parameters, a large-scale axion search apparatus, CARRACK2, was designed and constructed (Tada *et al.*, 1999) to search for axions over a wide range of mass. The diameter of the main magnet is 54 cm and the available inner diameter of 50 cm allows one to install cavities that correspond to $\sim 2\ \mu$eV axion mass. The coil is 90 cm long and the maximum flux density is 7 T.

The basic design, shown in Fig. 45, is similar to that of the prototype system CARRACK1, with several modifications to improve the system performance. The detection cavity is now located at the bottom of the cavity

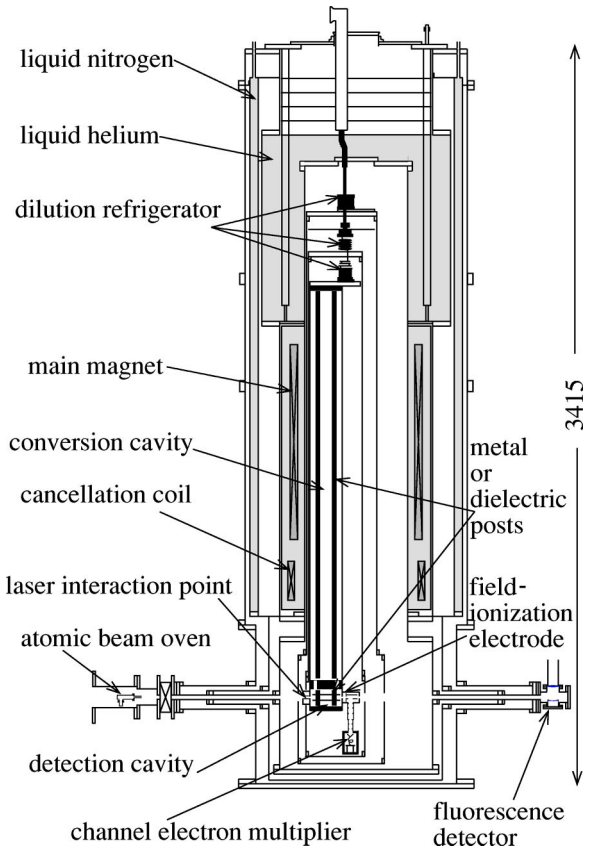

FIG. 45. Schematic drawing of a large-scale Rydberg-atom cavity-detector CARRACK2 to search for axions over a wide range of mass. From Tada *et al.*, 1999.

system, and the laser and atomic beams are injected into the cryostat transversally to the axis of the cylindrical cavity. This provides easier access to the inside and simplifies the alignment of the two beam systems. The metal and dielectric post system (Hagmann, Sikivie, Sullivan, Tanner, and Cho, 1990) was adopted for the tuning of the cavity resonant frequency. The driving system is more complicated than that for the rod system adopted in CARRACK1, but the cavity form factor and thus the detection efficiency are improved. Kevlar strings attached to external stepper motors are still used to drive the posts.

The search region to be covered with this system is from ~ 2 to $\sim 30\ \mu$eV. As shown in Fig. 43, the background noise from blackbody radiation in the cavity decreases with increasing frequency; therefore the signal-to-noise ratio increases with increasing axion mass. This means that the required temperature of the cavity system can be slightly higher than 10 mK as one goes to more than $\sim 15\ \mu$eV. However, the absolute counting rate decreases because the cavity volume decreases, so that the time necessary to achieve sensitivity to DFSZ axions increases, as can be seen in Fig. 44.

An important parameter for optimizing the sensitivity is the atomic velocity v. If v is small and thus $\overline{\gamma_a} \sim \gamma_a > \gamma_{\rm tr}$, the signal-to-noise ratio $\overline{R}_s/\overline{R}_n$ is almost independent of v, since $\overline{R}_s$ and $\overline{R}_n$ both decrease with v. How-

ever, if v is large, so that $\overline{\gamma_a} \sim \gamma_{\rm tr} > \gamma_a$, the signal rate $\overline{R_s}$ becomes rather insensitive to v, while the noise rate $\overline{R_n}$ increases with v. Hence the optimal sensitivity is expected to be attained when the atomic velocity v is

$$v \sim \overline{v} = L\gamma_a , \tag{79}$$

so that $\gamma_{\rm tr} \sim \overline{\gamma_a}$, and the original atomic damping rate is small enough so that $\gamma_b < \gamma_a$.

It is essential to optimize the atomic beam intensity and velocity in an axion search with the Rydberg-atom cavity detector. In practice, however, the actual spectrum of galactic axions is not known. If the energy spread of the axion signal is of the order $\gamma_a \sim \beta_a^2 m_a$ with $\beta_a \sim 10^{-3}$, then the optimum atomic velocity would be

$$v \sim (10^2 - 10^3)\ \ {\rm m\,sec}^{-1} \left(\frac{L}{0.1\ \ {\rm m}} \right) \left(\frac{\beta_a}{10^{-3}} \right)^2 \left(\frac{m_a}{10^{-5}\ \ {\rm eV}} \right). \tag{80}$$

However, it is possible that the galactic axion spectrum has narrow peaks. In this case, $\gamma_a \ll \beta_a^2 m_a$, and should galactic axions be discovered in the wideband search, the energy resolution could be improved by decreasing the atomic beam velocity and intensity so that $v/L = \gamma_{\rm tr} \ll \beta_a^2 m_a$ and $I_{\rm Ryd} \sim \overline{I}_{\rm Ryd} \propto v^2$ with $\overline{\Omega}_N \sim (\gamma_{\rm tr}\gamma)^{1/2} \propto v^{1/2}$ for $\gamma_a \lesssim \overline{\gamma_a} \sim \gamma_{\rm tr} \ll \beta_a^2 m_a$. The scanning step should also be reduced since $\Delta\omega_c \propto v$ [Eq. (74)]. The best choice of v may be given by Eq. (79), although we do not know γ_a for the narrow peaks beforehand. It might be much smaller than the original atomic width γ_b, in which case the ultimate resolution is limited by the lifetime of the Rydberg states in the cavity and the measurement integration time per cavity tune. This improvement of resolution would at any rate enable the identification of narrow peaks.

Several factors limit this method's reach in axion mass. For axion masses less than 2 μeV, the principal quantum numbers required would be $n \geq 180$. The polarizability of the Rydberg states increases as n^7 so that extreme care has to be taken to reduce the effect of Stark splitting in high-n states due to stray electric fields at the laser excitation and field-ionization regions. Strong Stark mixing in the higher-n states makes it impossible to separate the excited p states from the initially prepared s states with the field-ionization method (Tada *et al.*, 1999).

For higher masses, the limiting factor is the reduction of the cavity diameter and thus cavity volume. In this case, the use of multiple cavities or a higher-mode cavity would be useful to increase the effective volume. Note that only the conversion stage would require multiple cavities; a single cavity would still suffice for the detection stage.

VIII. SUMMARY AND OUTLOOK

For a cold-dark-matter candidate, the axion possesses the rare virtue of a fairly tightly bounded parameter space. The axion-photon couplings g_γ corresponding to the several different models proposed all cluster within an order of magnitude. The upper end of the mass range runs into a robust limit from SN1987a; the lower end, limited by cosmic overclosure, is more tenuous but is unlikely under any scenario to be less than a μeV.

Although the expected conversion power is extraordinarily weak, the technology will soon be in hand to perform a definitive search. By definitive, we mean one that will either find the axion with high probability, if it exists, or if not, exclude it. While the technological development so far has been very promising, we are not there yet. The new microstrip technique for coupling the signal into a SQUID has extended the application of SQUID's as high-gain amplifiers into the 1-GHz region, but we know that a new scheme (and possibly a new SQUID layout) will be required for 10 GHz and above. The near-quantum-limited noise performance of the current SQUID's is adequate to start the next-generation searches, although there are ideas and plans under consideration for searches that would reach the quantum limit. Higher-frequency operation poses no new conceptual problem for the Rydberg-atom single-quantum technique; the hurdle there is making this dauntingly complex experiment operate automatically and reliably. Regarding cavities for the 10–100-GHz region, both further conceptualization and practical development are needed.

We believe a successful strategy for a serious search involves a coordinated two-prong program: (1) Continued operation of the present experiments, to cover as much of the previously unexplored (m_A, g_γ) space as possible. Putting prejudices aside, the axion could be lurking anywhere in the open parameter space. (One should be open for a pleasant surprise, for example, a low-mass axion with a relatively strong coupling.) (2) Concurrent vigorous research and development on amplifiers and cavities, to be incorporated into the experiments on an ongoing basis. Ideally, operations should go on continuously, interrupted only by necessary upgrade-related activity. In this way, a serious program could deliver a definitive result in about a decade.

Finally, taking the optimistic point of view, we reiterate that when the axion is discovered, it will not be the end of the journey, but only the beginning. The other unique virtue of this experiment is that it measures the total energy of the axion, mass plus kinetic, and there may be fine structure to the signal. The peaks in frequency due to the flows of dark matter in the halo will contain a wealth of information about the formation of the Milky Way galaxy and will mark the beginning of a new subfield of astronomy. Axionic dark matter would also represent a unique macroscopic quantum system for study. A fourth-generation experiment might combine the output of two cavities and measure the output power as a function of their separation to map out the correlation function for the axionic Bose fluid, which should be on the order of 10–100 m for the virialized component.

ACKNOWLEDGMENTS

This work was performed under the auspices of the U.S. Department of Energy, Contracts Nos. W-7405-ENG-048, DE-AC03-76SF00098, and DE-FG02-97ER41029, and the National Science Foundation under Grant No. PHY-9501959 and Contract No. PHY-9600014.

REFERENCES

Abbott, L., and P. Sikivie, 1983, Phys. Lett. **120B**, 133.
Adler, S., 1969, Phys. Rev. **177**, 2426.
Agarwal, G. S., 1984, Phys. Rev. Lett. **53**, 1732.
Alexeyev, E. N., *et al.*, 1987, Pis'ma Zh. Eksp. Teor. Fiz. **45**, 461 [JETP Lett. **45**, 589 (1987)].
André, M-O., M. Mück, J. Clarke, J. Gail, and C. Heiden, 1999, Appl. Phys. Lett. **75**, 698.
Asztalos, S., *et al.*, 2001, Phys. Rev. D **64**, 092003.
Asztalos, S., *et al.*, 2002, Astrophys. J. Lett. **571**, L27.
Babu, K. S., and R. N. Mohapatra, 1990, Phys. Rev. D **41**, 1286.
Bardeen, W. A., and S.-H. H. Tye, 1978, Phys. Lett. **74B**, 229.
Barr, S. M., 1984, Phys. Rev. D **30**, 1805.
Barr, S. M., D. Chang, and G. Senjanovic, 1991, Phys. Rev. Lett. **67**, 2765.
Battye, R. A., and E. P. S. Shellard, 1994a, Nucl. Phys. B **423**, 260.
Battye, R. A., and E. P. S. Shellard, 1994b, Phys. Rev. Lett. **73**, 2954.
Battye, R., and Shellard, 1996, Phys. Rev. Lett. **76**, 2203(E).
Beg, M. A. B., and H. S. Tsao, 1978, Phys. Rev. Lett. **41**, 278.
Belavin, A. A., A. M. Polyakov, A. S. Shvarts, and Yu. S. Tyupkin, 1975, Phys. Lett. **59B**, 85.
Bell, J. S., and R. Jackiw, 1969, Nuovo Cimento A **60**, 47.
Bradley, R. F., 1999, Nucl. Phys. B (Proc. Suppl.) **72**, 137.
Braginsky, V. B., and F. Y. Khalili, 1992, in *Quantum Measurement*, edited by K. Thorne (Cambridge University, Cambridge, England/New York).
Bratton, C., *et al.*, 1988, Phys. Rev. D **37**, 3361.
Callan, C. G., R. F. Dashen, and D. J. Gross, 1976, Phys. Lett. **63B**, 334.
Cantor, R., 1996, in *SQUID Sensors: Fundamentals and Applications*, edited by H. Weinstock (Kluwer Academic, Dordrecht), p. 179.
Chang, S., C. Hagmann, and P. Sikivie, 1999, Phys. Rev. D **59**, 023505.
Cheng, H.-Y., 1988, Phys. Rep. **158**, 1.
Choi, K., 1992, Nucl. Phys. B **383**, 58.
Davis, R., 1985, Phys. Rev. D **32**, 3172.
Davis, R., 1986, Phys. Lett. **180B**, 225.
Daw, E., and R. F. Bradley, 1997, J. Appl. Phys. **82**, 1925.
Dearborn, D., D. Schramm, and G. Steigman, 1986, Phys. Rev. Lett. **56**, 26.
de Bernardis, P., *et al.*, 2000, Nature (London) **404**, 955.
DeGrand, T., T. W. Kephart, and T. J. Weiler, 1986, Phys. Rev. D **33**, 910.
DePanfilis, S., A. C. Melissinos, B. E. Moskowitz, J. T. Rogers, Y. K. Semertzidis, W. U. Wuensch, H. J. Halama, A. G. Prodell, W. B. Fowler, and F. A. Nezrick, 1987, Phys. Rev. Lett. **59**, 839.
Dicke, R. H., 1946, Rev. Sci. Instrum. **17**, 268.
Dicus, D., E. Kolb, V. Teplitz, and R. Wagoner, 1978, Phys. Rev. D **18**, 1829.
Dicus, D., E. Kolb, V. Teplitz, and R. Wagoner, 1980, Phys. Rev. D **22**, 839.
Dine, M., and W. Fischler, 1983, Phys. Lett. **120B**, 137.
Dine, M., W. Fischler, and M. Srednicki, 1981, Phys. Lett. **104B**, 199.
Donnelly, T. W., S. J. Freedman, R. S. Lytel, R. D. Peccei, and M. Schwartz, 1978, Phys. Rev. D **18**, 1607.
Drung, D., 1996, in *SQUID Sensors: Fundamentals and Applications*, edited by H. Weinstock (Kluwer Academic, Dordrecht), p. 63.
Eichler, R., *et al.*, 1986, Phys. Lett. B **175**, 101.
Ellis, J., and M. K. Gaillard, 1979, Nucl. Phys. B **150**, 141.
Ellis, J., and K. Olive, 1987, Phys. Lett. B **193**, 525.
Frampton, P. H., and T. W. Kephart, 1991, Phys. Rev. Lett. **66**, 1666.
Frampton, P. H., and D. Ng, 1991, Phys. Rev. D **43**, 3034.
Gallagher, T. F., 1994, *Rydberg Atoms* (Cambridge University Press, Cambridge).
Gasser, J., and H. Leutwyler, 1985, Nucl. Phys. B **250**, 465.
Gates, E. J., G. Gyuk, and M. S. Turner, 1995, Astrophys. J. Lett. **449**, L123.
Georgi, H., 1978, Hadronic J. **1**, 155.
Georgi, H., and I. McArthur, 1981, Preprint No. HUTP-81/A011.
Glauber, R. J., 1965, in *Quantum Optics and Electronics*, edited by C. DeWitt, A. Blandin, and C. Cohen-Tannoudji (Gordon and Breach, New York).
Gross, D. J., R. D. Pisarski, and L. G. Yaffe, 1981, Rev. Mod. Phys. **53**, 43.
Gurvitch, M., M. A. Washington, and H. A. Huggins, 1983, Appl. Phys. Lett. **42**, 472.
Hagmann, C. A., 1990, Ph.D. thesis (University of Florida).
Hagmann, C., S. Chang, and P. Sikivie, 2001, Phys. Rev. D **63**, 125018.
Hagmann, C., and P. Sikivie, 1991, Nucl. Phys. B **363**, 247.
Hagmann, C., P. Sikivie, N. S. Sullivan, and D. B. Tanner, 1990, Phys. Rev. D **42**, 1297.
Hagmann, C., P. Sikivie, N. S. Sullivan, D. B. Tanner, and S.-I. Cho, 1990, Rev. Sci. Instrum. **61**, 1076.
Hanany, S., *et al.*, 2000, Astrophys. J. Lett. **545**, L5.
Harari, D., and P. Sikivie, 1987, Phys. Lett. B **195**, 361.
Haroche, S., 1982, in *Rydberg Atoms and Radiation in a Resonant Cavity*, Les Houches 38, edited by G. Grynberg and R. Stora (Elsevier Science, Amsterdam), p. 192.
Haroche, S., 1990, *Cavity Quantum Electrodynamics*, Les Houches 1990 LIII, edited by J. Dalibard, J. M. Raimond, and J. Zinn-Justin (Elsevier Science, Amsterdam), p. 767.
Harris, P. G., *et al.*, 1999, Phys. Rev. Lett. **82**, 904.
Heitler, W., 1954, *The Quantum Theory of Radiation*, 3rd ed. (Oxford University Press, Oxford).
Hilbert, C., and J. Clarke, 1985, J. Low Temp. Phys. **61**, 263.
Hindmarsh, M., 1992, Phys. Rev. D **45**, 1130.
Hirata, K., *et al.*, 1988, Phys. Rev. D **38**, 448.
Hogan, C. J., and M. J. Rees, 1988, Phys. Lett. B **205**, 228.
Ipser, J., and P. Sikivie, 1983, Phys. Rev. Lett. **50**, 925.
Jackiw, R., and C. Rebbi, 1976, Phys. Rev. Lett. **37**, 172.
Jaklevic, R. C., J. Lambe, A. H. Silver, and J. E. Mercereau, 1964, Phys. Rev. Lett. **12**, 159.
Janka, H.-T., W. Keil, G. Raffelt, and D. Seckel, 1996, Phys. Rev. Lett. **76**, 2621.
Jaycox, J. M., and M. B. Ketchen, 1981, IEEE Trans. Magn. **MAG-17**, 400.
Jaynes, E. T., and F. W. Cummings, 1963, Proc. IEEE **51**, 89.
Josephson, B. D., 1962, Phys. Lett. **1**, 251.

Kaplan, D. B., 1985, Nucl. Phys. B **260**, 215.
Kaplan, D. B., and A. V. Manohar, 1986, Phys. Rev. Lett. **56**, 2004.
Keil, W., H.-T. Janka, D. N. Schramm, G. Sigl, M. S. Turner, and J. Ellis, 1997, Phys. Rev. D **56**, 2419.
Ketchen, M. B., and J. M. Jaycox, 1982, Appl. Phys. Lett. **40**, 736.
Kim, J., 1979, Phys. Rev. Lett. **43**, 103.
Kim, J. E., 1987, Phys. Rep. **150**, 1.
Kinion, S. D., 2001, Ph.D. thesis (University of California, Davis).
Kishimoto, Y., M. Tada, K. Kominato, M. Shibata, S. Yamada, T. Haseyama, I. Ogawa, H. Funahashi, K. Yamamoto, and S. Matsuki, 2002, Phys. Lett. A **303**, 279.
Kitagawa, A., K. Yamamoto, and S. Matsuki, 1999, e-print hep-ph/9908445.
Kleppner, D., and T. W. Ducas, 1976, Bull. Am. Phys. Soc. **21**, 600.
Kobayashi, M., and K. Maskawa, 1973, Prog. Theor. Phys. **49**, 652.
Koelle, D., R. Kleiner, F. Ludwig, E. Dantsker, and J. Clarke, 1999, Rev. Mod. Phys. **71**, 631.
Kolb, E., and I. I. Tkachev, 1993, Phys. Rev. Lett. **71**, 3051.
Kolb, E., and I. I. Tkachev, 1994, Phys. Rev. D **49**, 5040.
Kolb, E., and I. I. Tkachev, 1996, Astrophys. J. Lett. **460**, L25.
Krauss, L., J. Moody, F. Wilczek, and D. Morris, 1985, Phys. Rev. Lett. **55**, 1797.
Kroll, N. M., 1965, in *Quantum Optics and Electronics*, edited by C. DeWitt, A. Blandin, and C. Cohen-Tannoudji (Gordon and Breach, New York).
Kuchimanchi, R., 1996, Phys. Rev. Lett. **76**, 3486.
Kurokawa, K., 1965, Bell Syst. Tech. J. **44**, 1675.
Lange, J., 1969, IEEE Trans. Microwave Theory Tech. **17**, 1150.
Lazarides, G., R. Schaefer, D. Seckel, and Q. Shafi, 1990, Nucl. Phys. B **346**, 193.
Likharev, K. K., 1986, *Dynamics of Josephson Junctions and Circuits* (Gordon and Breach, New York)
Linde, A., 1991, Phys. Lett. B **259**, 38.
Linde, A. D., 1984, JETP Lett. **40**, 1333.
Linde, A. D., 1985, Phys. Lett. **158B**, 375.
Linde, A. D., and D. H. Lyth, 1990, Phys. Lett. B **246**, 353.
Louisell, W. H., 1990, *Quantum Statistical Properties of Radiation* (Wiley, New York).
Lynden-Bell, D., 1967, Mon. Not. R. Astron. Soc. **136**, 101.
Lyth, D. H., 1990, Phys. Lett. B **236**, 408.
Lyth, D. H., 1992a, Phys. Lett. B **275**, 279.
Lyth, D. H., 1992b, Phys. Rev. D **45**, 3394.
Lyth, D. H., and E. D. Stewart, 1992a, Phys. Lett. B **283**, 189.
Lyth, D. H., and E. D. Stewart, 1992b, Phys. Rev. D **46**, 532.
Matsuki, S., and K. Yamamoto, 1991, Phys. Lett. B **263**, 523.
McCumber, D. E., 1968, J. Appl. Phys. **39**, 3113.
Mohapatra, R. N., and A. Rasin, 1996, Phys. Rev. Lett. **76**, 3490.
Mohapatra, R. N., and G. Senjanovic, 1978, Phys. Lett. **79B**, 283.
Moskowitz, B. E., and J. Rogers, 1988, Nucl. Instrum. Methods Phys. Res. A **264**, 445.
Mück, M., M-O. André, J. Clarke, J. Gail, and C. Heiden, 1998, Appl. Phys. Lett. **72**, 2885.
Mück, M., M.-O. André, J. Clarke, J. Gail, and C. Heiden, 1999, Appl. Phys. Lett. **75**, 3545.
Mück, M., and J. Clarke, 2000, J. Appl. Phys. **88**, 6910.
Mück, M., and J. Clarke, 2001a, Appl. Phys. Lett. **78**, 3666.
Mück, M., and J. Clarke, 2001b, Rev. Sci. Instrum. **72**, 3691.
Mück, M., J. B. Kycia, and J. Clarke, 2001, Appl. Phys. Lett. **78**, 967.
Nagasawa, M., and M. Kawasaki, 1994, Phys. Rev. D **50**, 4821.
Nelson, A. E., 1984, Phys. Lett. **136B**, 387.
Ogawa, I., S. Matsuki, and K. Yamamoto, 1996, Phys. Rev. D **53**, R1740.
Okwit, S., 1984, IEEE Trans. Microwave Theory Tech. **MTT-32**, 1068.
Particle Data Group, 1998, Eur. Phys. J. C **3**, 1.
Peccei, R. D., 1989, in *CP Violation*, edited by C. Jarlskog (World Scientific, Singapore), p. 503.
Peccei, R. D., and H. Quinn, 1977, Phys. Rev. Lett. **38**, 1440.
Peng, H., *et al.*, 2000, Nucl. Instrum. Methods Phys. Res. A **444**, 569.
Perlmutter, S., *et al.*, 1999, Astrophys. J. **517**, 565.
Pospieszalski, M. W., 1993, in *Proceedings of the 23rd European Microwave Conference* (Reed Exhibition, Tunbridge Wells, UK), p. 73.
Preskill, J., M. Wise, and F. Wilczek, 1983, Phys. Lett. **120B**, 127.
Raffelt, G., and D. Dearborn, 1987, Phys. Rev. D **36**, 2211.
Raffelt, G., and D. Seckel, 1988, Phys. Rev. Lett. **60**, 1793.
Raffelt, G. G., 1990, Phys. Rep. **198**, 1.
Raimond, J. M., P. Goy, M. Gross, C. Fabre, and S. Haroche, 1982, Phys. Rev. Lett. **49**, 117.
Ramo, S., J. R. Whinnery, and T. van Duzer, 1965, *Fields and Waves in Communication Electronics* (Wiley, New York).
Reiss, A. G., *et al.*, 1998, Astron. J. **116**, 1009.
Rydberg, J. R., 1890, Philos. Mag. **29**, 331.
Ryhänen, T., H. Seppä, R. Ilmoniemi, and J. Knuutila, 1989, J. Low Temp. Phys. **76**, 287.
Schiff, L., 1968, *Quantum Mechanics*, 3rd ed. (McGraw-Hill, New York).
Schramm, D. N., and M. S. Turner, 1998, Rev. Mod. Phys. **70**, 303.
Schultz, S., D. R. Smith, and N. Kroll, 1993, in *Proceedings of the Particle Accelerator Conference 4* (IEEE, Washington, D.C.), p. 2559.
Seaton, M. J., 1958, Mon. Not. R. Astron. Soc. **118**, 501.
Seckel, D., and M. S. Turner, 1985, Phys. Rev. D **32**, 3178.
Shifman, M. A., A. I. Vainshtein, and V. I. Zakharov, 1980, Nucl. Phys. B **166**, 493.
Siebert, W. M., 1986, *Circuits Signals, and Systems* (McGraw-Hill, New York).
Siegman, A. E., 1961, Proc. IRE **49**, 633.
Siegman, A. E., 1964, *Microwave Solid-State Masers* (McGraw-Hill, New York).
Sikivie, P., 1982, Phys. Rev. Lett. **48**, 1156.
Sikivie, P., 1983a, Phys. Rev. Lett. **51**, 1415.
Sikivie, P., 1983b, in *Where Are the Elementary Particles, Proceedings of the 14th Summer School on Particle Physics*, Gif-sur-Yvette, 1982, edited by P. Fayet *et al.* (Institut National de Physique Nuclear et Physique des Particules, Paris), p. 1.
Sikivie, P., 1985, Phys. Rev. D **32**, 2988.
Sikivie, P., 1987, in *Cosmology and Particle Physics*, edited by E. Alvarez (World Scientific, Singapore), p. 143.
Sikivie, P., 1998, Phys. Lett. B **432**, 139.
Sikivie, P., 1999, in *Proceedings of the Second International Workshop on the Identification of Dark Matter*, edited by N. Spooner and V. Kudryavtsev (World Scientific, Singapore), p. 474.

Sikivie, P., and J. R. Ipser, 1992, Phys. Lett. B **291**, 288.
Sikivie, P., I. I. Tkachev, and Y. Wang, 1995, Phys. Rev. Lett. **75**, 2911.
Sikivie, P., I. I. Tkachev, and Y. Wang, 1997, Phys. Rev. D **56**, 1863.
Sikivie, P., and S. Wick, 2002, Phys. Rev. D **66**, 023504.
Srednicki, M., 1985, Nucl. Phys. B **260**, 689.
Steinhardt, P. J., and M. S. Turner, 1983, Phys. Lett. **129B**, 51.
Stewart, W. C., 1968, Appl. Phys. Lett. **12**, 277.
Suzuki, M., 1986, Phys. Lett. B **175**, 364.
't Hooft, G., 1976a, Phys. Rev. D **14**, 3432.
't Hooft, G., 1976b, Phys. Rev. Lett. **37**, 8.
Tada, M., Y. Kishimoto, K. Kominato, M. Shibata, S. Yamada, T. Haseyama, I. Ogawa, H. Funahashi, K. Yamamoto, and S. Matsuki, 2002, Phys. Lett. A **303**, 285.
Tada, M., Y. Kishimoto, M. Shibata, K. Kominato, I. Ogawa, H. Funahashi, K. Yamamoto, and S. Matsuki, 2001, e-print physics/0101028.
Tada, M., *et al.*, 1999, Nucl. Phys. B **72**, 164.
Tesche, C. D., and J. Clarke, 1977, J. Low Temp. Phys. **27**, 301.
Tesche, C. D., and J. Clarke, 1979, J. Low Temp. Phys. **37**, 397.
Turner, M. S., 1985, Phys. Rev. D **32**, 843.
Turner, M. S., 1988, Phys. Rev. Lett. **60**, 1797.
Turner, M. S., 1990, Phys. Rep. **197**, 67.
Turner, M. S., and F. Wilczek, 1991, Phys. Rev. Lett. **66**, 5.
Unruh, W. G., and R. M. Wald, 1985, Phys. Rev. D **32**, 831.
Vafa, C., and E. Witten, 1984, Phys. Rev. Lett. **53**, 535.
Vilenkin, A., and A. E. Everett, 1982, Phys. Rev. Lett. **48**, 1867.
Weinberg, S., 1975, Phys. Rev. D **11**, 3583.
Weinberg, S., 1978, Phys. Rev. Lett. **40**, 223.
Wellstood, F. C., C. Urbina, and J. Clarke, 1994, Phys. Rev. B **49**, 5942.
Wilczek, F., 1978, Phys. Rev. Lett. **40**, 279.
Wuensch, W., S. DePanfilis-Wuensch, Y. K. Semertzidis, J. T. Rogers, A. C. Melissinos, H. J. Halama, B. E. Moskowitz, A. G. Prodell, W. B. Fowler, and F. A. Nezrick, 1989, Phys. Rev. D **40**, 3153.
Yamaguchi, M., M. Kawasaki, and J. Yokoyama, 1999, Phys. Rev. Lett. **82**, 4578.
Yamamoto, K., and S. Matsuki, 1998, in *Proceedings of the Second International Workshop on the Identification of Dark Matter in the Universe*, Buxton UK, edited by N. J. Spooner and V. Kudryatsev (World Scientific, Singapore), p. 474.
Yamamoto, K., and S. Matsuki, 1999, Nucl. Phys. B (Proc. Suppl.) **72**, 132.
Yamamoto, K., *et al.*, 2001, e-print hep-ph/0101200.
Zhitnitsky, A. R., 1980, Sov. J. Nucl. Phys. **31**, 260.